Moore, G.F., Taira, A., and Klaus, A., et al., 2001
Proceedings of the Ocean Drilling Program, Initial Reports Volume 190

7. SITE 1176[1]

Shipboard Scientific Party[2]

SITE SUMMARY

The objective of Site 1176 was to determine the nature of accreted sediments of the large thrust-slice zone as well as to understand deformation and potential fluid flow related to a major out-of-sequence thrust (OOST). The OOST itself, however, was not penetrated.

We recognized three lithostratigraphic units at Site 1176. Unit I (upper slope–basin facies) extends from the seafloor to 195.79 meters below seafloor (mbsf). Its lithologies include nannofossil-rich mud, volcanic ash, and sand to silt turbidites. The principal processes of sedimentation for Unit I were hemipelagic settling and turbidity currents, with occasional volcanic ash falls and remobilization by slumping. Unit II (middle slope–basin facies) extends from 195.97 to 223.54 mbsf. In addition to typical hemipelagic mud, Unit II contains sandy mudstone and rare beds of volcanic ash. Deposition of this facies occurred from muddy debris flows, routine settling of suspended sediment, and occasional ash falls. Unit III was cored to a depth of 440.36 mbsf and contains abundant interbeds of sand to silt turbidites, carbonate-poor hemipelagic mudstone, pebbly mudstone, gravel, and rare volcanic ash. The primary depositional environment for this unit was probably a trench-fan system fed by a transverse submarine canyon, and depletion of carbonate supports the idea of deposition below the carbonate compensation depth. The petrographic compositions of sands and gravels, rich in sedimentary lithic fragments and quartz, show that their provenance is southwest Japan as typically represented by the Shimanto Belt. The junction between the lowermost slope sediment and the top of the accretionary prism probably coincides with the boundary between Units II and III.

Site 1176 can be divided into two structural domains: slope basin and accretionary prism. Deformation of the slope-basin sediments (0–224 mbsf) is characterized by inclined bedding intervals in which

[1]Examples of how to reference the whole or part of this volume.
[2]Shipboard Scientific Party addresses.

Ms 190IR-107

slump folds together with contorted and chaotically mixed bedding are locally developed. These features are interpreted to record the effects of active tilting and uplifting of the slope basin. Small faults are thought to result from extensional response to this tilting and uplift of the basin and/or burial compactional strains. In contrast, deformation structures are almost absent in the accreted sediments (below 224 mbsf), although core recovery was very poor. However, the apparently consistent near-horizontal bedding may reflect the flat part of a hanging-wall anticline formed in association with an underlying thrust.

Biostratigraphic age control was provided by calcareous nannofossils. Nannofossil assemblages are Pliocene (Zone NN16) to Pleistocene in age (Subzone NN21b) according to nine recognized biostratigraphic events. Although nannofossils are common and generally moderately preserved in the upper Pleistocene, nannofossils from sediments older than 1 Ma are rare and poorly preserved. Age models based on biostratigraphy indicate sedimentation rates of ~0.07–0.26 m/k.y.

Inclination data of Hole 1176A after alternating-field (AF) demagnetization at 30 mT provided useful information for interpretation of geomagnetic polarity changes from the late Pliocene to the Pleistocene. The Brunhes/Matuyama boundary (0.78 Ma) is interpreted to occur at 199.55 mbsf. Seven short reversal events were observed in the Brunhes Chron and may represent geomagnetic excursions in this chron.

The most intense microbially mediated reactions occur in the top <100 mbsf of the section. Microbial sulfate reduction is complete at ~20 mbsf. In the top half of this zone, the sulfate reduction rate decreases linearly with depth, whereas in the lower half, maximum sulfate reduction occurs at the base of the zone. The alkalinity produced is involved in carbonate reactions, and the ammonium produced is involved in clay ion exchange reactions.

The alkalinity maximum and Ca and Mg minima coincide with the depth of the base of the sulfate reduction zone; thus, this depth interval is also characterized by intense carbonate diagenesis. The Ca and Mg concentration profiles indicate that in the sulfate reduction zone, both authigenic dolomite precipitation and replacement of a precursor biogenic calcite occur. Deeper, however, through the upper and middle slope–basin section, replacement of a precursor calcite is the only dolomitization reaction.

Volcanic ash or other silicate diagenetic reactions are minimal because of the low geothermal gradient of 56°C/km. Diatom dissolution may control the pore fluid silica concentration. At the base of the section, pore fluids have a composition close to seawater, as indicated by the return to seawater concentrations of all abiogenic components, except for K. The Cl concentration profile is consistent with diffusion between a low-Cl zone at greater depth and the seafloor. Because of poor recovery, the location of the low-Cl zone is poorly defined but is constrained to be between 240 and 320 mbsf. The low-Cl fluid is enriched in Ca and depleted in Na, K, and Mg. A chemically similar fluid was identified at Site 1174.

Diffusion of low-chlorinity interglacial seawater into the sediment section is not observed at this site. As at Site 1175, this may be the result of repeated slope-failure events and sediment reworking. At greater depths, the residual signal from the glacial ocean seawater may have been overprinted by diffusion.

The total carbon content for the sediments examined between 200 and 401.6 mbsf at Site 1176 ranged from 0.05 to 2.25 wt%. The highest carbon value (2.25 wt% at 340 m) was dominated by a terrestrial com-

ponent likely derived from fan debris flow to the trench sediments. The sulfur content showed a similar trend to total organic carbon (TOC) with the highest values of sulfur (1.05 and 2.07 wt%) coincident with the highest TOC values (0.86 and 2.25 wt%). The inorganic carbon (~0.05–2.6 wt%) and high carbonate content (up to ~35 wt%) are similar to values observed at Site 1175. Methane concentrations in sediments below the sulfate reduction zone (~9.5 m) are consistent with a bacterial origin. Methane dominates the composition of the hydrocarbons measured throughout Hole 1176A.

Bacterial abundance was enumerated in 18 samples obtained at Site 1176. Abundance at the surface was 6.67×10^8 cells/cm^3. The deepest sample is 363.49 mbsf with 1.71×10^6 cells/cm^3, representing 0.25% of the surface population. Bacterial populations decline rapidly from the surface, consistent with the decrease in sulfate concentrations to near zero at 14.6 mbsf. The decline in bacterial abundance with depth follows the predicted depth/population size relationship very closely. In addition to the onboard assays, 11 whole-round cores were taken for shipboard enrichment cultures, cell viability, and shore-based microbiological analysis to measure potential bacterial activities, culture microorganisms, characterize nucleic acids, and investigate fatty acid biomarkers.

Porosities decrease gradually with depth in the upper slope–basin facies (Unit I), from values of ~65%–73% at the mudline to 55%–60% at 200 mbsf. Within the upper slope–basin facies, there is considerable scatter in porosity, with values ranging from 51% to 73%. This scatter may be related to the inferred deposition of this unit by slope failure processes. No clear changes in index properties occur at the boundary between the upper and middle slope–basin facies (Units I and II). Within the middle slope–basin facies (Unit II), porosity continues to decrease gradually with depth, following the same trend as observed for the upper slope–basin facies. Changes in index properties correlate with the boundary between the middle slope–basin and accretionary prism facies (Units II and III) at 225 mbsf. Porosity decreases from 53%–57% to 48%–54% across this boundary. Velocity and formation factor also increase at the top of Unit III. Within Unit III, porosities decrease with depth, reaching ~40%–47% by ~310 mbsf. From this depth to 405 mbsf, porosities remain constant, with values ranging from ~40% to 47%.

Five successful in situ temperature measurements indicate a thermal gradient of 0.056°C/m.

Results from the gas permeameter at Site 1176 are slightly different from those from other sites in that the range is even greater and there is no general decrease with depth. Throughout the hole, the hemipelagic clays show low values with greater scatter than elsewhere, and in the upper half of the section (above 200 mbsf), sands, gravels, and especially ashes gave much higher values. In the lower half of the hole, sands and gravels give high measurements, even at the bottom of the hole.

This site provided information regarding the nature of accreted sediments that compose the large thrust-slice zone including the slope-basin transition. Coarse clastic sediments of Outer Zone origin, perhaps transported through a transverse canyon, are the dominant lithology of the accreted sediments. The accreted section of this zone is, thus, very different from the axially transported, volcaniclastic-rich trench sediments at Sites 1173, 1174, and 808. The age of the prism is probably younger than 2 Ma, and slope-basin development initiated <1 Ma, suggesting extraordinarily rapid growth of the prism.

OPERATIONS

Transit from Site 1175 to Proposed Site ENT-06A (Site 1176)

Once the seafloor positioning beacon was recovered, the 1.6-nmi transit to proposed Site ENT-06A (Site 1176) was made in dynamic positioning mode in 3 hr. During the transit, the instrumented load pins, which had been returned to the ship on the boat transfer earlier in the leg, were reinstalled in the block. A seafloor positioning beacon was deployed at 0915 hr on 26 June, establishing Site 1176.

Hole 1176A

The precision depth recorder (PDR) indicated a seafloor depth of 3016.8 meters below sea level (mbsl) (3028.4 meters below rig floor [mbrf]). Based on the correlation between the previous PDR measurements and the drilling depth as determined via drill-pipe measurement, the bit was lowered to 3018.4 mbsl (3030 mbrf). Hole 1176A was spudded at 1305 hr on 26 June. In Core 1H, 7.41 m of sediment was recovered, indicating a seafloor depth determined by drill-pipe measurement of 3020.5 mbsl (3032.1 mbrf) (Tables T1, T2). The hole was cored with the advanced hydraulic piston corer (APC) from the seafloor to 170.6 mbsf (3202.7 mbrf), where the overpull had increased to 60,000 lb while we retrieved Core 19H. A considerable amount of sand was encountered in the hole, and a 6.1-m section of sand (from 115.3 to 121.4 mbsf; 3147.4 to 3153.5 mbrf) was drilled ahead without coring. Nineteen APC cores that penetrated 164.5 m of section and recovered 151.43 m of sediment (92%) were taken.

The extended core barrel (XCB) coring system was then used to core from 170.6 to 449.6 mbsf (3202.7 to 3481.7 mbrf). Twenty-nine XCB cores were taken, coring 279.0 m and recovering 74.82 m (27%). Sand was encountered virtually throughout the entire borehole. The scientists decided to terminate the hole because the extensive sands prevented achievement of the primary objectives of the hole.

The bit was pulled out of the hole and cleared the seafloor at 0745 hr on 29 June. The seafloor positioning beacon was released at 0845 hr and sighted on the surface at 0925 hr. At this time, however, the current was ~2.8 kt and there were also 15-kt winds, so the beacon was swept away from the ship before it could be recovered. The pipe trip continued and the bit cleared the rotary table at 1345 hr, ending Hole 1176A and operations at Site 1176. Once the bit was back aboard, the ship began the transit to proposed Site WNT-01B (Site 1177) in dynamic positioning mode.

LITHOSTRATIGRAPHY

We recognized three lithostratigraphic units at Site 1176 (Fig. F1). In a general sense, all three units are equivalent to what was cored at Site 1175 (Table T3).

T1. Coring summary, p. 55.

T2. Coring summary by section, p. 56.

F1. Stratigraphic column, Site 1176, p. 23.

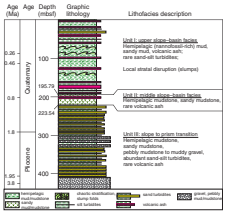

T3. Summary of stratigraphic relations, p. 61.

Unit I (Upper Slope-Basin Facies)

Unit I is Quaternary in age, extends from the seafloor to a subbottom depth of 195.79 mbsf, and is equivalent to Unit I and part of Unit II at Site 1175 (Table T3). This unit consists predominantly of nannofossil-rich hemipelagic mud (silty clay to clayey silt) interlayered with volcanic ash, thin beds of sand, silty sand, clayey sand, silt, and rare sandy mud. In contrast to Unit I at Site 1175, chaotic bedding with recognizable fold hinges (e.g., Fig. F2) is present in only one core (interval 190-1176A-7H-2, 115 cm, to 7H-4, 120 cm). Steeply dipping strata are present in a number of other cores (190-1176A-9H, 16H, and 19H), and these deformed intervals may have been caused by slumping.

The mud in Unit I is greenish gray in color and homogeneous, faintly laminated, or mottled (see "Lithostratigraphy," in the "Site 1175" chapter for a more detailed description). Diatoms become scarce in the lower part of the unit, but nannofossils are abundant throughout (see "Site 1176 Smear Slides," p. 49). Volcanic ash beds are common (Fig. F3). The thickest ash recovered (1.67 m) is located at the base of Core 190-1176A-18H (159.4 mbsf). The ash layers are similar to those at Site 1175 (Fig. F4). Sand, clayey sand, and silt are present mainly as thin beds, laminae, and a few thick beds (Fig. F5).

Processes responsible for the sedimentation of Unit I include hemipelagic settling, occasional turbidity currents, and submarine mudflows, together with air falls of volcanic ash. Chaotic deposits are less prevalent than at Site 1175; this is probably because Site 1176 is located on a nearly flat-lying part of the slope basin with modest relief nearby.

Unit II (Middle Slope–Basin Facies)

At Site 1175, Unit II was defined primarily by the presence of sandy mudstone throughout. This unusual lithology also occurs in Unit II at Site 1176, but in only two cores (intervals 190-1176A-22X-4, 139 cm, to 22X-7, 48 cm, and 25X-3, 67 cm, to 25X-4, 34 cm). The other lithologies of Unit II are a more typical hemipelagic mudstone (silty claystone to clayey siltstone) and rare beds of volcanic ash. Unit II is also considerably thinner at Site 1176 (27.75 m) than at Site 1175 with the top and base at 195.79 and 223.54 mbsf, respectively (Table T3). Sedimentation occurred by hemipelagic settling, muddy debris flow, and volcanic ash falls.

Unit III (Slope to Prism Transition Facies)

The most characteristic feature of Unit III is the common occurrence of thin- to medium-bedded silty or sandy turbidites. The top of Unit III is located where thin sand beds become abundant at 223.54 mbsf (Section 190-1176A-25X-4, 34 cm). Other lithologies include pebbly mudstone and gravel, sandy mudstone, and silty claystone. This unit is equivalent to Unit III at Site 1175 but contains more gravel and woody material. The deepest core within this unit is from 440.36 mbsf (Section 190-1176A-48X-CC, 36 cm).

Sand to silty sand is thin to thick bedded and moderately indurated. Typical internal sedimentary structures include plane-parallel laminae and/or cross-laminae (Fig. F6). Cross-stratification is particularly common in Cores 190-1176A-37X to 44X. Most such beds also display sharp to scoured bases, normal size grading, and gradational tops. All of these characteristics are consistent with transport by turbidity currents.

F2. Chaotic and inclined interbeds of volcanic ash and silty clay in Unit I, p. 24.

F3. Distribution and thickness of volcanic ash layers, p. 25.

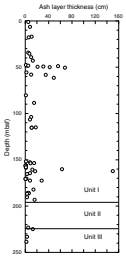

F4. Volcanic ash from Unit I, p. 26.

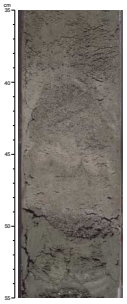

F5. Cycle of silty sand turbidites and gray-green silty clay from Unit I, p. 27.

The gravel to pebbly mudstone of Unit III is present in Cores 190-1176A-34X to 36X and 43X to 48X. These poorly indurated deposits are poorly sorted throughout and contain clay- to pebble-sized particles (Fig. F7). The matrix is composed of silty clay, similar in composition to the finer-grained interbeds. Larger clasts are rounded to subangular and up to 5 cm across. Clast lithologies include abundant quartz, chert, sedimentary and metasedimentary lithic fragments, feldspar, and woody material. In addition, poorly lithified fragments of green siltstone probably originated as locally derived rip-up clasts.

The sandy mudstone of Unit III is typically greenish gray, gray, or green and homogeneous to faintly laminated or mottled by bioturbation. Nannofossils are less abundant than in the silty clays of Unit I (see description in "Lithostratigraphy" p. 4, in the "Site 1175" chapter for more details). Unit III also contains rare laminae and thin beds of gray to brown ash (Fig. F3). These strata are composed predominantly of fresh volcanic glass. In addition, a single bed of carbonate-cemented claystone is present in interval 190-1176A-43X-2, 55–70 cm. This layer is probably a product of diagenetic alteration of nannofossil-rich claystone.

The depositional mechanisms and depositional setting for Site 1176 are basically the same as those described for Unit III at Site 1175. Based solely on lithologic characteristics, we are not able to draw a definitive distinction between lowermost trench-slope deposits and the uppermost part of the accretionary prism. Several interpretations need to be considered. One possibility is that the thin sand beds within the upper part of Unit III settled onto a sedimentary carapace above the uplifting prism as thicker turbidity currents moved across the trench floor and lapped onto the landward wall. Interpretations of seismic reflection data, on the other hand, suggest that the unconformity between slope facies and accretionary prism occurs at a depth of ~230 mbsf at Site 1176. This depth coincides reasonably well with the upper boundary of Unit III (223.54 mbsf). The preponderance of coarse-grained gravity-flow deposits within Unit III also favors a depositional site with subdued seafloor gradients to promote rapid deceleration and trigger deposition. The flat floor of the trench satisfies this expectation better than a steeply inclined lower slope. Another way to accommodate the high influx of coarse-grained detritus would be to initiate frontal accretion close to the mouth of a submarine canyon, then to sustain the flow path of the canyon through the newly formed slope basin as uplift of the accretionary prism continued. This uplift pattern would prevent the development of a clear facies change from trench to trench-slope environments.

X-Ray Diffraction Mineralogy

The results of X-ray diffraction (XRD) analysis of bulk-sediment samples from Site 1176 are shown in Figure F8 and Table T4. Within Unit I, the average relative percentages of total clay minerals, quartz, plagioclase, and calcite are 38%, 27%, 11%, and 23%, respectively (Table T5). The content of total clay minerals does not change appreciably downsection. Quartz and plagioclase abundances within Unit III increase to average values of 41% and 17%, respectively. We attribute these changes in composition to a greater proportion of siliciclastic influx and coarser grain size within Unit III. Conversely, with one exception of carbonate-cemented claystone, the calcite content drops sharply below the upper boundary of Unit III (Fig. F8). Depletion of calcite is

F6. Cross-laminae in silty sand from Unit III, p. 28.

F7. Quartz pebbles and lithic clasts in muddy matrix from Unit III, p. 29.

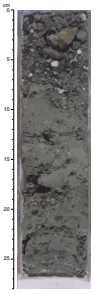

F8. Abundance of total clay minerals, quartz, plagioclase, and calcite, p. 30.

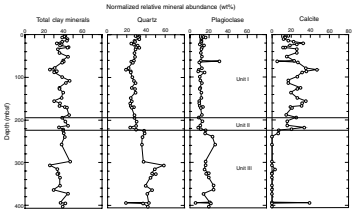

T4. Peak intensities and peak areas from XRD analysis of sediments, p. 62.

T5. Relative mineral abundance based on XRD analysis of sediments, p. 64.

probably a function of deposition below the calcite compensation depth and dilution of the biogenic pelagic component of suspended sediment influx by terrigeneous silt and clay. Deposition of Unit III in deeper water (relative to Units I and II) is also consistent with the interpretation of the Unit II/III boundary as an unconformity between accreted trench-wedge deposits and slope sediments.

XRD analysis was completed on four volcanic ash samples from Site 1176 (Table T6). Three of the analyses produced unusual results. One sample (190-1176A-13H-3, 12–13 cm) contains an unidentified mineral with a high-intensity peak that corresponds to a d-value of 3.648 Å. A second sample (190-1176A-17H-3, 52–53 cm) is a crystal tuff with abundant plagioclase, quartz, and pyroxene; a relatively low intensity background on the diffractogram indicates that the content of volcanic glass is minor. The third unusual sample (190-1176A-18H-2, 68–69 cm) contains a large amount of well-crystallized mica in addition to crystals of quartz and plagioclase and abundant glass.

T6. XRD analysis of volcanic ash, p. 65.

STRUCTURAL GEOLOGY

Site 1176 was drilled to retrieve both slope-basin and accreted sediments. The deformational features of the slope-basin sediments are very similar to those at Site 1175, whereas deformational structures are commonly lacking in the accreted sediments, although core recovery was very poor. As shown in Table T7 and Figures F9 and F10, attitudes of bedding are quite different between lithostratigraphic Units I and II (upper and middle slope–basin facies) and III (accretionary prism).

T7. Structural data, p. 66.

F9. Bedding dips relative to the core liner plotted vs. depth, p. 31.

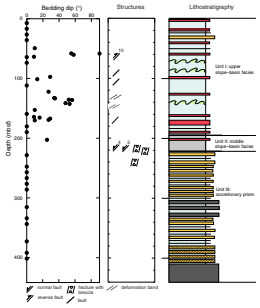

In Units I and II (0–224 mbsf), horizontal and inclined bedding intervals alternate (Fig. F9). In the intervals of inclined bedding, the orientation of bedding exhibits a high degree of scatter (Fig. F10). Some of these inclined bedding intervals include slump folds (Fig. F2) and contorted and chaotically mixed bedding, indicating deformational features similar to the equivalent sedimentary facies at Site 1175. In addition, high-angle small faults are sporadically developed in Units I and II (Fig. F9). They are characterized by dark seams <6 mm across (Fig. F11). These small faults show both normal and reverse senses of movement and displacements up to 1 cm (Fig. F9), but displaced markers are commonly absent. Deformation bands displaying faultlike features are observed at 130, 146, and 149 mbsf (Table T7; Fig. F9). They consist of planar dark zones no more than 3 mm across, but no displaced markers are observed across them. A remarkable aspect of these features is that they are developed in quite soft, muddy sediments.

F10. Stereographic projections of bedding in Units I and II, p. 32.

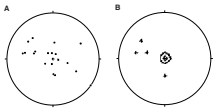

We again interpret that the inclined bedding intervals bounded by horizontal bedding intervals above and below resulted from slumping due to tectonic tilting and uplift of the slope basin associated with displacement along the seismically imaged thrust. Our interpretation of the small faults is the same as at Site 1175; they record burial compactional strains and/or extensional response related to tilting and uplifting of the slope basin.

F11. Examples of small faults, p. 33.

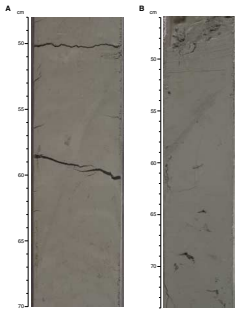

Zones of locally intense fracturing and faulting, ~30 cm in thickness, are present across the facies boundary between Units II and III (Fig. F9). Unlike those at Site 1174, these zones are not inclined, organized fracture zones but instead consist of irregular fractures with various orientations, predominantly vertical or high angle. Below this facies boundary, core recovery was extremely poor and XCB biscuiting precluded observation of deformation structures. Where observed, bedding dips were

consistently horizontal (Fig. F9). As Unit III probably includes accretionary prism sediments (see "Lithostratigraphy," p. 4), such flat-lying bedding was unexpected. One possible explanation for this horizontal orientation is that these accreted sediments at Site 1176 may correspond to the flat part of a hanging-wall anticline formed in association with the underlying thrust. The main thrust fault beneath Site 1176 appears to show flat-ramp-flat geometry in the three-dimensional (3-D) seismic reflection data (see "Seismic Stratigraphy," p. 21), and the few observed fractures with weakly developed slickensides could reflect the only modest deformation typical of a flat. Unfortunately this remains speculative, as the extremely poor recovery and high degree of XCB biscuiting prevent any unequivocal interpretation of deformation in the accreted sediments.

Uncalibrated Gas-Permeameter Measurements

Results from the gas permeameter at Site 1176, again subject to the provisos outlined in "Structural Geology," p. 6, in the "Explanatory Notes" chapter, are slightly different from those at other sites in that the range is even greater and there is no general decrease with depth (Fig. F12). The hemipelagic clays show greater scatter than at previous sites, between 10^{-15} and 10^{-17} m^2, and the apparently high-permeability materials are more varied in nature. A black gravel at 34.13 mbsf is so permeable it was impossible to measure. Sandy layers high in the section also gave large values, but the greatest apparent gas permeabilities above 200 mbsf were yielded by bands of volcanic ash, typically between 10^{-11} and 10^{-13} m^2.

In the lower half of the hole, from 200 mbsf to its base, the silty clays continue to range irregularly between 10^{-15} and 10^{-17} m^2, but here the high values are given by sands and gravels. Many of the sand laminae are not represented in the data because they had been somewhat washed away during core preparation, giving a recessed surface to the split core face that was impractical to measure. However, sufficient determinations were possible to show that values in excess of 10^{-13} m^2 were common even at these depths. In fact the deepest material recovered here, polymict gravels at 440 mbsf, gave results among the highest at the site.

F12. Uncalibrated gas-permeability results, p. 34.

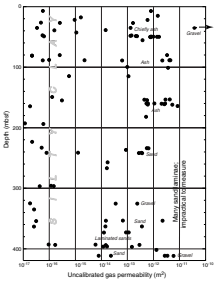

BIOSTRATIGRAPHY

Sediments recovered from Site 1176 provide a sedimentary record from the Quaternary (Subzone NN21b) to the Pliocene. Calcareous nannofossils were used for developing the biostratigraphic framework according to the zonation schemes of Gartner (1977) and Martini (1971) with zonal modifications proposed by Young (1998) (Table T8). The interval (core and section) and depth (mbsf) constraints of calcareous nannofossil events recognized at Site 1176 are listed in Table T9. For the range of calcareous nannofossils at Site 1176, see Table T10.

T8. Recognized nannofossil events, p. 68.

T9. Interval and depth constraints of calcareous nannofossil events, p. 69.

T10. Calcareous nannofossil range chart, p. 70.

Calcareous Nannofossils

Hole 1176A was cored to 440.35 mbsf recovering Quaternary (Subzone NN21b) to Pliocene nannofossil assemblages (Zone NN15?). Slump deposits within the Quaternary and common reworking of nan-

nofossils in the Pliocene sediments may lead to misplaced first and last occurrences.

Pleistocene

Sediments recovered from 7.4 to 286.37 mbsf (Samples 190-1176A-1H-CC to 32X-CC) yield Pleistocene nannofossil assemblages. Below an interval from Samples 190-1176A-1H-CC to 25X-CC yielding abundant and well-preserved nannofossils, there is a sharp decrease in abundance alongside a decline to poorer preservation. Small placoliths such as *Emiliania huxleyi* and *Gephyrocapsa* spp. dominate the assemblage. The composition of Pleistocene assemblages older than 0.26 Ma is characterized by the dominance of gephyrocapsids. Reworked Neogene taxa such as discoasterids, *Reticulofenestra pseudoumbilicus,* and *Sphenolithus* spp. were encountered sporadically throughout the Pleistocene samples. Based on counts of 300 specimens per sample, the onset of the *E. huxleyi* acme Subzone NN21b (0.085 Ma) could be determined between Samples 190-1176A-1H-CC and 2H-CC. A further event used to subdivide Subzone NN21a was the last occurrence of *Helicosphaera inversa* (0.14 Ma) between Samples 190-1176A-6H-CC and 7H-CC. The base of Subzone NN21a, marked by the first occurrence of *E. huxleyi* (0.26 Ma), was observed between Samples 190-1176A-9H-CC and 10H-3, 89–90 cm. Sample 190-1176A-10H-3, 89–90 cm, is placed in Zone NN20 because of the absence of *E. huxleyi* and *Pseudoemiliania lacunosa*. The following event recognized was the last occurrence of *P. lacunosa* that marks the top of Zone NN19 between Samples 190-1176A-10H-3, 89–90 cm, and 10H-CC. Because *P. lacunosa* is excellently preserved, reworking is not considered here. Samples 190-1176A-11H-4, 78–79 cm, to 12H-4, 75–76 cm, which are barren of *P. lacunosa,* were assigned to Zone NN20 again. The presence of *P. lacunosa* (0.46 Ma) in Sample 190-1176A-12H-4, 75–76 cm, assigns the level to Zone NN19. This unusual sequence of biostratigraphic events could be explained by local stratal disruption that characterizes the lithostratigraphic unit from 0 to 195.79 mbsf. The last occurrence of *Reticulofenestra asanoi* (0.8 Ma) (between Samples 190-1176A-22X-CC and 23X-2, 53–54 cm) and its first occurrence (1.06 Ma) (between Samples 190-1176A-26X-CC to 27X-2, 75–76 cm) provide further datums to subdivide Zone NN19. The first occurrence of *Gephyrocapsa oceanica* (1.77 Ma), which approximates the Pleistocene/Pliocene boundary, was observed between Samples 190-1176A-32X-CC and 33X-CC. Identification of different *Gephyrocapsa* acme zones may lead to a more precise biostratigraphy for the Quaternary.

Pliocene

Sediments cored from 296.90 mbsf to the bottom of the hole at 440.36 mbsf (Samples 190-1176A-42X-CC to 48X-CC) contain nannofossils of Pliocene age that are mostly poorly preserved and scarce. The late Pliocene assemblages are dominated by reticulofenestrids and *Pseudoemiliania* spp. Reworking of older Neogene taxa is common, making a biostratigraphic assignment for the lower part of the sequence difficult. The last occurrence of *Discoaster brouweri* defining the top of Zone NN18 (2.0 Ma) was observed between Samples 190-1176A-44X-CC and 45X-CC with fairly abundant and well-preserved *D. brouweri* specimens. The presence of *Discoaster pentaradiatus* and large *R. pseudoumbilicus* (>7 µm), of which the last occurrence defines the top of Zone NN15 (3.8 Ma), was observed between Samples 190-1176A-46X-CC and 47X-CC.

This could represent reworking of early Pliocene fossils in younger nonfossiliferous sediments because nannofossils are rare throughout the Pliocene but obviously reworked specimens are common. Further analysis of additional samples may resolve those problems.

PALEOMAGNETISM

Introduction

Tensor tool orientations were successfully used to correct the magnetic declinations from 16.95 to 170.60 mbsf (Cores 190-1176A-3H through 19H). After measuring the natural remanent magnetization, all sections of the archive half of the core were partially demagnetized using AF magnetization at 30 mT at 5-cm intervals to remove magnetic overprints. Inclination data obtained after AF demagnetization provide useful information for interpreting late Pliocene to Pleistocene geomagnetic polarity reversals. Magnetic polarity reversals at Hole 1176A were correlated with the Hole 1175A polarity pattern using inclination measurements after AF demagnetization at 30 mT. However, identification of geomagnetic polarity intervals based on inclination changes in the lower part of Hole 1176A was difficult because of poor core recovery.

Paleomagnetic Results

The declinations of cores from 16.95 to 170.60 mbsf (Cores 190-1176A-3H through 19H) were corrected using Tensor tool orientation measurements. These declination changes reflect the secular variation of the geomagnetic field, although some of these may possibly be short geomagnetic excursions (Fig. **F13**). Two anomalous declination directions of 180° at 121.45–139.85 mbsf (top of Core 190-1176A-14H through bottom of Core 15H) and 140.45–159.65 mbsf (top of Core 190-1176A-16H through bottom of Core 17H) are also observed. These declination anomalies may be caused by core rotation, but it is unknown why the corrected declinations show opposite directions from geomagnetic north. Scattered declinations below 170.60 mbsf indicate that several pieces of core rotated individually during XCB coring.

Positive inclinations were observed from 0 to 199.55 mbsf (Fig. **F13**) after AF demagnetization at 30 mT. Seven short intervals of reversed polarity inclinations were observed in this positive inclination zone. These negative inclinations probably reflect geomagnetic excursions commonly observed in this normal chron. These events appear to correspond to the anomalous declination directions (Table **T11**) and are very similar to reversed polarity inclination events at Site 1175 (see **"Paleomagnetic Results,"** p. 12, in "Paleomagnetism" in the "Site 1175" chapter).

Magnetic intensity shows slightly low values with some high-intensity peaks from 0 to 241.40 mbsf (Section 190-1176A-27X-3, 50 cm) (Fig. **F13**). These high-intensity peaks closely correspond to high-susceptibility peaks measured with the multisensor track (MST) (see **"Physical Properties,"** p. 17) and likely reflect the existence of ash layers. Higher intensity was observed from 241.40 to ~300 mbsf (Section 190-1176A-27X-3, 55 cm).

F13. Paleomagnetic declination, inclination, and intensity, p. 35.

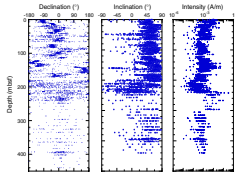

T11. Depths and ages of magnetic chrons and subchrons, p. 72.

Magnetostratigraphy

Site 1176 magnetostratigraphy is based on polarity changes determined by measuring the inclination of the archive half of the core after AF demagnetization at 30 mT. A magnetic polarity change from normal to reversed at 199.55 mbsf (Section 190-1176A-23X-1, 5 cm) is interpreted as the Brunhes/Matuyama Chron boundary dated at 0.78 Ma (Cande and Kent, 1995) (Fig. **F14**). Seven short reversed polarity events are also observed in the Brunhes Chron at 46.70 mbsf (Section 190-1176A-6H-1, 130 cm), 61.20 mbsf (Section 7H-5, 30 cm), 64.50 mbsf (Section 8H-1, 10 cm), 140.50 mbsf (Section 16H-1, 5 cm), 159.45 mbsf (Section 18H-1, 5 cm), 163.95 mbsf (Section 19H-2, 5 cm), and 181.75 mbsf (Section 21X-2, 5 cm). These short intervals are thought to represent geomagnetic excursions in the Brunhes Chron and may be correlated with the eight major excursions of Champion and Lanphere (1988), which include Laschamp (~0.04 Ma), Blake (~0.13 Ma), Jamaica (~0.19 Ma), Lavantine (~0.29 Ma), Biwa III (~0.38 Ma), Emperor (~0.47 Ma), Big Lost (~0.56 Ma), and Delta (~0.62 Ma). A clear short excursion known as Chron C1n-1 (Cande and Kent, 1995) was also identified in the Brunhes Chron at Site 1176. However, identification of such excursions is sometimes difficult because they are usually very short events. In an effort to identify the excursions, comparisons were made with the paleomagnetic results of Site 1175. The inclination anomaly at 161.47 mbsf (Section 190-1176A-18H-2, 70 cm) may correspond to excursion C1n-1.

The top of the Matuyama Chron (0.780–2.581 Ma) is interpreted to occur at 199.55 mbsf. In this reversed chron, poor core recovery makes identification of short normal polarity geomagnetic events difficult. The nearly continuous normal polarity interval from 214.80 (Section 190-1176A-24X-4, 120 cm) to 219.35 mbsf (Section 25X-1, 65 cm) may be the Jaramillo Event (0.99–1.07 Ma).

F14. Magnetostratigraphy, p. 36.

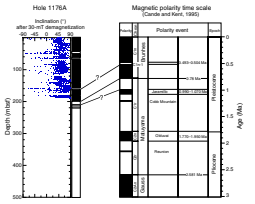

Sedimentation Rate

Based on the depth and age of the Brunhes/Matuyama boundary, the sedimentation rate of lithostratigraphic Units I and II is estimated at 25.58 cm/k.y. (Fig. **F15**) and correlates well with biostratigraphic results (see **"Biostratigraphy,"** p. 8).

F15. Age-depth plot, p. 37.

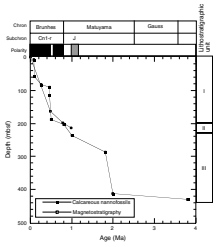

INORGANIC GEOCHEMISTRY

Forty-five pore fluid samples were squeezed from selected 10- to 60-cm-long whole-round samples for chemical and isotopic analyses. Sample depths ranged from 1.4 to 394.8 mbsf. One 5-cm-long core-catcher sample was also selected from the bottom of the hole at 440 mbsf. Because only 0.5 mL of pore fluid was recovered from this sample, it was sealed for shore-based analyses and is not included in Table **T12** or Figure **F16.** Samples were collected from every section in Cores 190-1176A-1H and 2H, from three sections in Core 3H, and from two sections in Cores 4H and 5H. One sample per section was collected per core from the remainder of the site where core quality and recovery were adequate for a pore fluid sample. Because of poor core recovery in Cores 190-1176A-28X through 35X, 37X, and 38X, pore fluid chemical data are not available for 239–325 and 326–354 mbsf.

T12. Pore fluid composition, p. 73.

F16. Pore fluid compositions as a function of depth, p. 38.

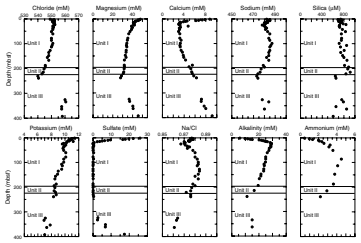

Elemental concentrations are reported in Table T12 and plotted in Figure F16. As at the former sites, eight major and minor dissolved anions and cations that sensitively reflect inorganic or microbially mediated water-rock reactions were determined for each sample. The anions are Cl, Ca, Mg, Na, K, and Si, and the cations are alkalinity and sulfate. Salinity and pH were also determined. Every third sample was analyzed for ammonium. Between 300 and 400 mbsf, only three samples were analyzed for alkalinity because of the small volume of pore fluid obtained in this depth interval.

The outstanding characteristics of the pore fluids concentration-depth profiles at Site 1176 are the sharp discontinuities, particularly in the Cl gradient, that occur between ~230 and 320 mbsf, the return of most abiogenic components (except for K) to near-seawater concentrations below this discontinuity, and the intense microbially mediated reactions that occur at rather shallow depth, in the top 100 m of the section, and dominate the inorganic diagenetic reactions at this depth interval. Carbonate and sulfide formation and ion exchange reactions are the important diagenetic reactions at this site.

Geochemistry Controlled by Inorganic Reactions

Chloride

Cl concentrations were determined with a relative analytical uncertainty of 0.1% based on duplicate or triplicate titrations of all samples. Cl concentrations are constant in the top 50–60 mbsf and then monotonically decrease with depth (Fig F16). The profile between ~60 and 240 mbsf is a diffusional profile driven by a deeper nonrecovered low-Cl fluid source. Lower than background core temperatures of 11°–12°C (instead of 14°–16°C) measured on the catwalk suggest that a small percent of the freshening observed in the pore fluids of Core 190-1176A-25X and particularly Core 26X may be caused by the dissociation of disseminated gas hydrate. Evidence of diffusion of low-chlorinity interglacial seawater into the sediment section was not observed at this site. One explanation for this is that repeated slumping has reworked these upper sediments, mixing zones with slightly different Cl concentrations (see "Inorganic Geochemistry," p. 15, in the "Site 1175" chapter and "Lithostratigraphy," p. 4).

Below ~320 mbsf, the pore fluids have slightly higher than seawater Cl concentrations. The transition from lower than seawater Cl to close to seawater Cl concentrations occurs between ~230 and 320 mbsf. The upper boundary of this zone, in which core recovery was marginal, corresponds to the boundary between lithostratigraphic Units II and III (see "Lithostratigraphy," p. 4). This residual pore fluid composition reflects only slight modification by diagenesis. Presently the temperature at this depth interval is low (~20°C) (see "Physical Properties," p. 17); thus, reactions are slow.

Sodium

The Na concentration-depth profile, although similar overall to that of Cl, shows two distinct and interesting features: a small minimum at ~23 mbsf, which is the depth of the alkalinity maximum, and a broad maximum centered at ~100 mbsf that corresponds to the ammonium maximum. The minimum suggests intimate involvement in authigenic carbonate formation, whereas the maximum is caused by expulsion

into the pore fluid from clay ion exchange sites by ammonium. Consequently, in Units I and II the Na/Cl ratios, 0.885 and 0.878, are slightly but significantly higher than the seawater ratio of 0.859.

Potassium

K concentrations generally decrease with depth from slightly higher than seawater values to 67% of seawater concentrations at the base of the section. A small minimum is observed at the depth of the alkalinity maximum. The broad maximum that corresponds to the depth of the ammonium maximum has been observed at each of the former sites drilled in the vicinity (i.e., Sites 1173–1175); it reflects expulsion into the pore fluids from clay ion exchange sites. The minimum associated with the alkalinity maximum was not observed at the other sites. This minimum is observed at this site because of the high carbonate content, ranging from ~8 to 27 wt%, in Units I and II (see **"Organic Geochemistry,"** p. 15). Unlike Cl or Na, at the base of the section K does not return to seawater concentrations but continues to be consumed by a diagenetic reaction or by mixing with a deep-seated K-depleted fluid.

Silica

Dissolved Si concentrations reach high values of ~750 µM close to the sediment-water interface and increase monotonically with depth to a maximum of 914 µM at ~215 mbsf, close to the boundary between lithostratigraphic Units I and II. Below this, the gradient reverses and the concentrations decrease with depth. The maximum concentration value is close to the solubility of opal-A at the prevailing temperature of ~12°C at ~200 mbsf. As at all other sites, diatom dissolution controls Si concentrations. Diatoms are present throughout the section but are greatly diminished in abundance and preservation at the depth interval that corresponds to the Unit II/III boundary (see **"Biostratigraphy,"** p. 8). Indeed, at ~230 mbsf Si concentrations drop to ~650 µM.

Calcium and Magnesium

Similar to those at adjacent Site 1175, Ca and Mg concentration-depth profiles indicate intense carbonate diagenesis in lithostratigraphic Units I and II. The Ca profile is a mirror image of the alkalinity profile, whereas the Mg profile is distinct. The Mg distribution mimics that of Ca above the Ca minimum; below the Ca minimum they exhibit inverse gradients—Ca concentrations increase and Mg concentrations decrease with depth. Both Ca and Mg concentrations are lower or equal to seawater concentrations throughout the section. The lack of elevated Ca concentrations indicates that Ca and Mg are principally involved in carbonate rather than silicate reactions. This is presumably due to the prevailing low temperatures at this site

Ca concentrations drop sharply by ~7 mM, to a minimum of 3 mM (28% of seawater value) in the top 20 m of the section, with a gradient of 0.38 mM/m. The Ca and Mg minima coincide with the alkalinity maximum, indicating authigenic dolomite precipitation. However, the drop in Mg concentrations in the upper 20 m of the section is ~13 mM (from a seawater value of ~54 mM to ~41 mM), a gradient of 0.65 mM/m, indicating that Mg uptake is almost double Ca uptake. This suggests that in the top section, Mg is simultaneously consumed by both authi-

genic dolomite formation and dolomitization of the precursor biogenic calcite. Below the Ca minimum to the base of Unit II, the inverse profiles of Ca and Mg indicate that dolomitization of calcite is the dominant reaction in most of the section.

At the base of the section, like Cl and Na, Ca and Mg return to almost seawater concentrations. The only reactions that can increase Mg concentrations in pore fluids are ion exchange and dedolomitization. However, net Mg ion exchange is limited to the upper 100 mbsf because insufficient ammonium is present below 100 mbsf and the Ca concentrations necessary for dedolomitization are much too low. Hence, the observed Mg increase at the base of Unit III unequivocally indicates that these pore fluids are only slightly modified seawater.

Geochemistry Controlled by Microbially Mediated Reactions

Sulfate

Sulfate concentrations rapidly decrease with depth and reach zero at ~20 mbsf, where alkalinity has its maximum value. At Site 1175, zero sulfate occurred at a shallower depth (~15 mbsf). Preliminary analysis of the shallow high-resolution data reveals that sulfate reduction rates decrease with depth in the top 10 m of the sulfate gradient zone, whereas in the lower half of the zone, the sulfate reduction rate is at maximum at the very base of the zone. From 20 mbsf to the top of Unit III, the pore fluids contain no sulfate. At the base of the section, sulfate concentrations increase rapidly, and at the deepest sample recovered the concentration is ~17 mM, almost 60% of the seawater value. The lower-than-seawater sulfate concentrations in a section with pore fluid compositions near that of seawater suggest that bacterial sulfate reduction has lowered the concentrations to present levels. This lowering may have occurred either before this subsection was buried, or sulfate reduction is ongoing at a very low rate. In this depth interval, alkalinity has a constant value of 15 mM, suggesting either a steady state between production as a result of sulfate reduction and reaction or no production.

Alkalinity

Alkalinity increases rapidly with depth to a maximum value of ~29 mM at ~20 mbsf, the depth at which sulfate concentrations reach zero value and Ca is at a minimum. At greater depths, alkalinity decreases monotonically to ~11 mM at the top of Unit III, suggesting a sink at greater depths. The gap in the profile at the crucial depth between ~240 and 320 mbsf does not allow full interpretation of the decreasing trend. The constant concentration of ~15 mM at the base of the section is discussed in "Sulfate," p. 14.

Ammonium

Ammonium produced by bacterially mediated decomposition of organic matter increases in concentration with depth, having a broad maximum of ~5 mM between ~20 and 200 mbsf. The maximum concentration and depth span are almost identical to those observed at the adjacent Site 1175. At such a high concentration, it preferentially occupies clay ion exchange sites, thus expelling Mg, K, and Na into the pore fluid, as discussed above. The decrease with depth implies an ammo-

nium sink at greater depth; however, the specific reaction(s) involved is as yet unknown.

Summary

At this site, the pore fluid chemistry is less modified from seawater than at the deeper-water, warmer Sites 1173 and 1174 and is modified to a similar extent as at the adjacent slope-basin Site 1175. The two most important reaction types that control the pore fluid chemistry are (1) carbonate diagenesis, mostly dolomitization, and (2) microbially mediated reactions with products intimately involved in the carbonate diagenesis. Other important reactions are opal-A (diatom) dissolution and clay ion exchange reactions with ammonium. At the base of the section, pore fluids maintain a composition close to seawater, as indicated by the return to seawater concentrations of all abiogenic components except for K. There is no evidence for important silicate reactions except diatom dissolution, as expected for the low geothermal gradient at this site.

The Cl concentration profile indicates diffusion between a low-Cl fluid zone at depth and the seafloor. Unfortunately, this interesting diffusion profile has a large data gap at a crucial depth interval because of low and no core recovery between ~240 and ~320 mbsf. Assuming that the Cl gradient is indeed driven by a low-Cl fluid possibly associated with the OOST fault, the Mg, Ca, Na, and K values suggest that this fluid has elevated Ca concentrations and is depleted in Na, K, and Mg. This chemical composition is similar to that of geochemically distinct fluid identified in structural and stratigraphic horizons at Site 1174.

Evidence of diffusion of low-chlorinity interglacial seawater into the uppermost sediment section is not observed at this site. This may be due to either rapid deposition of the upper 50–60 m of section or reworking of sediments by slumping.

ORGANIC GEOCHEMISTRY

Monitoring of volatile hydrocarbons was conducted for safety considerations, and organic, petrological, and geochemical studies were carried out to assess the types of organic matter and the molecular compositions of the hydrocarbons found in the accreted trench-slope sediments.

Forty-four sediment samples and two vacutainer samples were collected at Site 1176 (~10-m intervals) from 4.5 to 401.6 mbsf (Table **T13**). All sediments were analyzed for methane concentrations and light hydrocarbon compositions during headspace analyses (Fig. **F17A**). In addition, molecular gas compositions, TOC, inorganic carbon (carbonate), and sulfur analyses were performed (Fig. **F18;** Table **T14**) (see **"Organic Geochemistry,"** p. 14, in the "Explanatory Notes" chapter for analytical procedures).

TOC contents for the sediment samples examined ranged from 0.05 to 2.25 wt% (Fig. **F18**). The highest TOC value was found in a sample collected at 340 mbsf (2.25 wt%) that was characterized by a high content of terrestrial material observed in the form of plant detritus (fan debris flow) in the sediment. The average TOC content for sediments examined between 4.5 and 393 mbsf was ~0.50 wt%. Nitrogen contents for the same sample interval were extremely low (average = 0.03 wt%) with one spike at 200 mbsf (~0.12 wt%). Sulfur contents had a similar

T13. Headspace analyses, p. 74.

F17. Composition, concentrations, and distributions of headspace gases measured in sediments, p. 39.

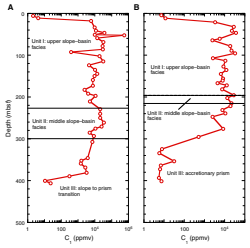

F18. TOC, S, and methane concentrations, p. 40.

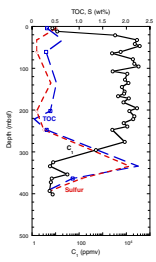

T14. Carbon, nitrogen, sulfur, and hydrogen analyses, p. 75.

trend to TOC values, ranging between 0 and 2.07 wt%, with the highest S values (1.05 and 2.07 wt%) coinciding with the highest TOC values (0.86 and 2.25 wt%).

Inorganic carbon values (0.05–2.8 wt%) are similar in range to those at Site 1175 and correspond to bulk carbonate values of 0.42–23.32 wt%, with some values up to 36.78 wt%; however, the average inorganic carbon values were higher in the upper 65 mbsf at Site 1176, ranging between 0.69 and 2.09 wt%. The only exception was in a sample collected from near the bottom of the hole that corresponded to the highest values for inorganic carbon and carbonate (4.4 and 36.65 wt%, respectively). In general, carbonate contents were highest in the upper ~200 mbsf and then decreased sharply over the remaining depth to just over 0.5 wt%, a trend also observed in Hole 1175A (Fig. **F17A, F17B**).

Hydrocarbon Gases

Headspace gas concentrations of methane were very low in the first 11.9 mbsf within the sulfate reduction zone (7.3–11.7 ppm) (Fig. **F17A, F17B**), also similar to Site 1175. An increase in concentration above this section, from 3377 to 36,920 ppm, was observed over the next 135 m of the hole. Methane concentrations remained moderately high (~8000–20,000 ppm) down to ~285 mbsf before dropping steadily over the remainder of the hole, with values dipping to 5.6–30.1 ppm at ~401.6 mbsf. The very low concentrations of methane in the lowest 30 m of the hole may be partially due to low core recovery and the lithologies encountered (mostly poorly consolidated sand and cobble-sized gravel) in the last few cores. As at Site 1175, the hydrocarbons encountered at Site 1176 are dominated by biogenic methane, with only trace levels of ethane (0.3–1.5 ppm) detected in a few samples.

Conclusions

Organic geochemistry analyses performed on samples from Site 1176 lead to the following conclusions:

1. TOC contents for sediments examined between ~200 and 401.6 mbsf at Site 1176 ranged from 0.05 to 2.25 wt%. The highest TOC value (2.25 wt% at 340 mbsf) was dominated by a terrestrial component likely derived from fan debris flow to the trench sediments.
2. Sulfur contents showed a similar trend to TOC contents, with the highest values of S (1.05 and 2.07 wt%) coincident with the highest TOC values (0.86 and 2.25 wt%).
3. Inorganic carbon concentrations (~0.05–2.6 wt%) and high carbonate contents (up to ~35 wt%) are similar to values observed at Site 1175.
4. Methane concentrations in sediments below the sulfate reduction zone (~9.5 mbsf) are consistent with a bacterial origin. Methane dominates the composition of the hydrocarbons measured throughout Hole 1176A.

MICROBIOLOGY

Eighteen samples for microbiological analysis were obtained from Hole 1176A for direct microscopic enumeration aboard ship. Eleven

whole-round cores were taken for shipboard enrichment cultures, cell viability, and shore-based microbiological analysis to measure potential bacterial activities, culture microorganisms, characterize nucleic acids, and investigate fatty acid biomarkers.

Total Bacterial Enumeration

Bacteria are present in all 18 samples (Table T15; Fig. F19). The surface sample (190-1176A-1H-1, 0–1 cm) contains 6.67×10^8 cells/cm^3, which follows a general trend observed at other Ocean Drilling Program (ODP) sites where near-surface bacterial populations decrease as overlying water depths increase (Table T16).

The deepest sample is at 363.49 mbsf (Sample 190-1176A-40X-1, 49–50 cm) with 1.71×10^6 cells/cm^3, representing 0.25% of the surface population. Bacterial populations decline rapidly from the surface, consistent with the decrease in sulfate concentrations to near zero at 14.6 mbsf (see "Inorganic Geochemistry," p. 11). Below 14.6 mbsf, bacterial populations increase with increases in methane concentrations (see "Organic Geochemistry," p. 15).

The depth distribution of total bacterial numbers in sediments from Site 1176 conforms to the general model for bacterial populations in deep-sea sediments (Parkes et al., 1994) from the surface to 363 mbsf (Fig. F19). Although deviations from the expected profile are greater than those observed at Site 1175 (see "Microbiology," p. 19, in the "Site 1175" chapter), they are nonetheless small, consistently remaining within the given 95% prediction limits, and there is no apparent correlation with any geochemical component of the sediment. The single datum with the greatest deviation is at 51 mbsf (Sample 190-1176A-6H-4, 114–115 cm), and interestingly, this deviation is coincident with the lowest organic carbon concentration measured at this site (0.05 wt%) (see "Organic Geochemistry," p. 15).

T15. Total bacterial populations in sediments, p. 76.

F19. Depth distribution of total bacterial populations in sediment samples, p. 41.

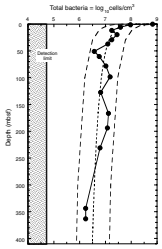

T16. Comparison of near-surface sediment bacterial populations, p. 77.

PHYSICAL PROPERTIES

Introduction

At Site 1176, laboratory measurements were made to provide a downhole profile of physical properties within a slope basin overlying accreted sediments. With the exception of extremely short (<50 cm) sections, all cores were initially passed through the MST before being split. Gamma-ray attenuation (GRA) and magnetic susceptibility measurements were taken at 4-cm intervals with 2-s acquisition times for all cores. Natural gamma ray (NGR) was counted every 20 cm for 20-s intervals.

Moisture and density samples were selected from undisturbed core at regularly spaced intervals of one per section. Measurements of dry volume and wet and dry mass were uploaded to the Janus database and were used to calculate water content, bulk density, grain density, porosity, void ratio, and dry bulk density. *P*-wave velocities were measured on split cores or discrete samples at a frequency of two to three per core. Measurements were taken in three directions when core conditions permitted.

Undrained shear strength measurements were made near the *P*-wave core measurement locations from between the mudline and 170 mbsf, at which point XCB coring began and the cores became too stiff for in-

sertion of the vane shear device. Conductivity measurements were taken at least once per core. Raw data and calculated physical properties are available from the Janus database for all MST, moisture and density, thermal conductivity, velocity, and shear strength measurements (see the "Related Leg Data" contents list). Because electrical conductivity data are not currently available from the database, they are included in Tables T17 and T18.

T17. Formation factor obtained by the needle-probe method, p. 78.

T18. Electrical conductivity and formation factor obtained for sample cubes, p. 79.

Density and Porosity

Sediment bulk density was determined by both the GRA method on unsplit cores and the mass/volume method ("index properties") on discrete samples (see "Physical Properties," p. 19, in the "Explanatory Notes" chapter). The GRA density data and the bulk densities determined by the mass/volume method are generally in good agreement for APC cores (Fig. F20A, F20B). Below ~170 mbsf, the small diameter of XCB cores results in GRA bulk densities that are 0.1–0.2 g/cm³ lower than those determined from discrete samples. Both moisture and density measured on discrete samples and GRA density measurements show similar downhole trends. The GRA density measurements are more closely spaced than moisture and density samples and show detailed bulk density variations within lithostratigraphic Unit I (upper slope–basin facies) that probably reflect lithologic variations. Both methods show shifts to higher bulk densities at ~60 mbsf (from ~1.55 above to ~1.65 g/cm³ below) and ~220 mbsf (from ~1.75 above to ~1.85 g/cm³ below).

Grain densities determined from dry mass and volume measurements are slightly lower in Unit I (average of 2.66 g/cm³) than in Unit III (accretionary prism) (average of 2.71 g/cm³), whereas values are scattered within Unit II (middle slope-basin) (Fig. F20C). In Units I and II, porosities decrease gradually with depth, from ~65%–70% at the mudline to 55%–60% at 220 mbsf. Porosities decrease by 3%–5% at the upper boundary of Unit III then decrease gradually with depth to ~300 mbsf. Below 300 mbsf, porosities remain relatively constant at between 40% and 45%.

F20. Bulk density, grain density, and porosity, p. 42.

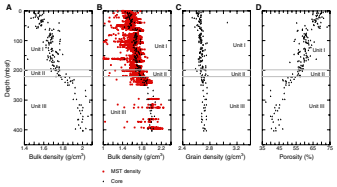

Shear Strength

Undrained shear strength measurements were made using a miniature automated vane shear (AVS) and were conducted exclusively in fine-grained silty clays. Below 170 mbsf (Core 190-1176A-19H), samples were sufficiently indurated that insertion of the AVS caused fracturing of the sediments. Shear strengths increase gradually downhole from ~10 kPa at the seafloor to values approaching ~80 kPa at 170 mbsf (Fig. F21). Scatter in the data increases between 50 and 110 mbsf as a result of fracturing of sediment and opening of fractures at the tips of the AVS vanes during some measurements. For this reason, actual sediment strength is probably best reflected by the highest measured values.

F21. Undrained peak shear strength, p. 43.

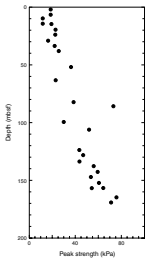

Thermal Conductivity and Projected Temperatures

Thermal conductivity was measured using a needle probe that was inserted into the unsplit core for a full-space conductivity measurement. In Units I and II, thermal conductivities generally range between 1.0 and 1.1 W/(m·°C) (Fig. F22A). The few thermal conductivity values obtained below this depth are significantly higher than those above

F22. Thermal conductivity and temperature trends, p. 44.

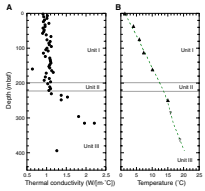

~220 mbsf. A conductive heat flow of 56 mW/m² was defined by shipboard thermal conductivity and downhole temperature measurements to 248 mbsf (see "In Situ Temperature and Pressure Measurements," p. 20) (Fig. F22B).

Acoustic Velocity

In APC cores, *P*-wave velocities were measured using the *P*-wave sensors 1 and 2 (PWS1 and PWS2) insertion probe system along the core axis (z-axis) and across the core axis (y-axis), respectively. The PWS3 contact probe system was used to measure *P*-wave velocities across the core liner (x-axis) (Fig. F23A). In XCB cores, sample cubes were cut and measurements were performed in all three directions using the PWS3 contact probe system. Acoustic impedance was computed as the product of bulk density and velocity along the z-axis. Bulk densities were obtained from moisture and density samples, and values were used only when acquired within 20 cm of the *P*-wave velocity measurements. When cubes were cut, moisture and density samples were generally taken adjacent to *P*-wave velocity samples.

Few velocity measurements could be obtained along the axis of APC cores because of gas expansion cracks, but measurements along the x- or y-axes of APC cores could be obtained in almost all cores (Fig. F23A). An increase in velocity from 1520 to 1620 m/s is observed between 57 and 65 mbsf. This increase correlates with an increase in bulk density and may correspond to a laterally continuous reflector on the seismic section. Velocities acquired between this level and ~180 mbsf display some scatter and do not readily correlate with specific seismic reflectors. The transition from Unit II to Unit III is marked by a strong gradient in velocity, with an increase from 1630 to 1830 m/s over a 20-m interval. This transition is also well marked on the impedance plot and thus may correspond to a seismic reflector (Fig. F23B). In Unit III, recovery was poor and measurements were infrequent. Unlike Site 1175, there is no velocity increase in the lower part of the hole and velocities at 400 mbsf are comparatively low, between 1700 and 1800 m/s.

F23. *P*-wave velocity and impedance, p. 45.

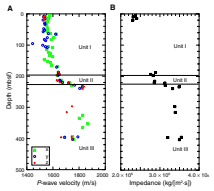

Electrical Conductivity

Measurements were made on APC cores with a four-needle 30-kHz electrode array. On XCB cores, conductivity was measured on the same sample cubes used for *P*-wave measurements with a two-electrode 30-kHz system. Electrical conductivity and formation factor (see "Physical Properties," p. 19, in the "Explanatory Notes" chapter) measured on the sample cubes are given in Table T18. For needle-probe measurements, only the apparent formation factor is given. The formation factor displays the same sharp boundaries as porosity and *P*-wave velocity at ~60 and 200–220 mbsf. The formation factor ranges from 2.3 to 3 between 0 and 60 mbsf and from 3 to 4.5 between 60 and 220 mbsf and increases to ~5.5 at 220 mbsf (Fig. F24). The formation factor in Unit III could only be measured at the very top of the unit and near the bottom of Hole 1176A in the few layers that were recovered. These samples are poorly sorted sand/silt/clay mixtures and have anisotropic properties with a bedding-parallel formation factor of ~5 and a bedding-transverse formation factor of ~6 (Table T17).

F24. Formation factor, p. 46.

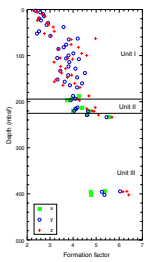

Magnetic Susceptibility

Volumetric magnetic susceptibilities were measured in all recovered cores from Site 1176 (Fig. F25). Uncorrected values of magnetic susceptibility from the Janus database were used. Magnetic susceptibility values show no obvious downhole trend and generally fall between 10 × 10^{-5} and 40 × 10^{-5} SI with little scatter. Several magnetic susceptibility peaks have values as high as 300 × 10^{-5} SI. Between 220 and 250 mbsf, magnetic susceptibility values increase slightly from 10 × 10^{-5}–30 × 10^{-5} to 50 × 10^{-5}–120 × 10^{-5} SI.

Natural Gamma Ray

NGR results are presented in counts per second (cps) (Fig. F26). The background scatter, produced by Compton scattering, photoelectric absorption, and pair production, was measured at the beginning (6.39 cps) and subtracted from the measured gamma-ray values. In general, NGR counts are low and are consequently likely to be affected by the short counting interval and by porosity variations. Overall, NGR data show considerable scatter between 15 and 30 cps. A slight decrease of NGR values is observed at 60 and 180 mbsf.

Summary and Discussion

Porosities decrease gradually with depth in the upper slope–basin facies (mudline to ~200 mbsf). Between the mudline and 50 mbsf, a slight decrease in bulk density is observed. Within this interval, zones of increasing and decreasing bulk density are observed. This observation may be related to slump structures. No clear changes in bulk density or porosity occur at the boundary between the upper and middle slope–basin facies (Unit I/II boundary). In the middle slope–basin facies (Unit II), there are no obvious porosity changes. Changes in moisture and density correlate with the boundary between the middle slope–basin and accretionary prism facies (Unit II/III boundary). Porosity decreases from 56% to 48%–54% at 225 mbsf. Velocity and formation factor increase at the top of Unit III. Between 225 and 300 mbsf, porosity decreases rapidly with depth, reaching ~40%–47%. Porosity does not change significantly between 300 mbsf and the last measurement at 405 mbsf.

IN SITU TEMPERATURE AND PRESSURE MEASUREMENTS

Five reliable determinations of downhole temperatures were made at Site 1176 using the Adara APC tool and the Davis-Villinger temperature probe (DVTP). Table T19 summarizes the deployments, and the temperature data are shown in Figures F27 and F28. In situ temperatures were estimated by extrapolation of the station data to correct for the frictional heating on penetration assuming a thermal conductivity of 1.0 W/(m·°C).

Two additional measurements were attempted with the DVTP, and one additional measurement was taken with the water-sampling temperature probe (WSTP) during a water sampling run. At these three stations, temperatures were anomalous, despite reasonable decay curves

F25. Magnetic susceptibility, p. 47.

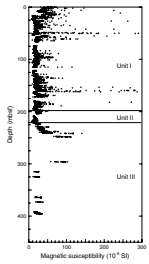

F26. Natural gamma ray, p. 48.

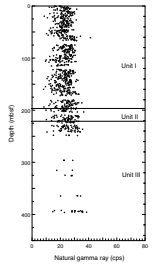

T19. Summary of downhole temperature measurements, p. 80.

F27. Temperatures measured during the deployment of the APC temperature tool, p. 49.

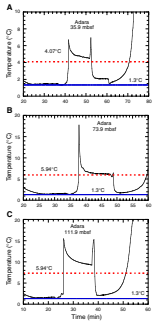

F28. Temperatures measured in Hole 1176A during the DVTP stations, p. 50.

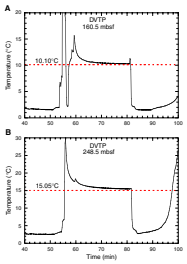

(Fig. F29). Infiltration of seawater from the bottom of the borehole into permeable or cracked formation provides the most plausible explanation for these data.

The mudline temperature and the five upper measurements define a linear gradient of 0.056°C/m in the upper 248.5 m (Fig. F30). For thermal conductivities of 1.0 W/(m·°C), vertical conductive heat flow at Hole 1176A would be 56 mW/m². Pressures were also recorded during the DVTP-P deployments at 248.5, 295.7, and 383.5 mbsf. The pressure record from the successful run, which was at 248.5 mbsf, is shown in Figure F31. As noted in **"In Situ Temperature and Pressure Measurements,"** p. 26, in the "Explanatory Notes" chapter, postcruise modeling and processing is required to estimate in situ pressures.

SEISMIC STRATIGRAPHY

Lithostratigraphic boundaries at Site 1176 can be correlated with reflections on 3-D seismic line 277 (Fig. F32). Specific correlations should be considered preliminary at this time because the velocity structure at this site is not well known. Any inaccuracies in velocity will produce errors in depth conversion. Additional velocity work will be carried out postcruise to improve depth conversions and stratigraphic correlations.

Lithostratigraphic Unit I is recognized on the seismic line as a sequence bounded at the top by the seafloor and at the bottom by a strong reflector that dips northwest, intersecting Site 1176 at ~180 mbsf (Fig. F32). Reflections within the upper 800 m of the sequence are generally continuous and dip slightly to the southeast (seaward), but the lower reflections are somewhat discontinuous and dip northwest (landward). The unit thickens to the northwest and exhibits an overall wedge shape.

Seismic Unit II is correlated with lithostratigraphic Unit II and is bounded by a sharp reflection at its top and onlaps the underlying sequence at its base. Internal reflections are strong and continuous northwest of Site 1176 but are discontinuous and lower amplitude southeast of Site 1176.

The lowest identified seismic stratigraphic unit correlates with lithostratigraphic Unit III. It is defined by an angular unconformity at its top. Internal reflections exhibit high amplitudes, are laterally continuous, and dip steeply to the northwest (landward).

The major out-of-sequence thrust that was a significant target for this site is interpreted to lie ~10–20 m below the base of Hole 1176A.

F29. Temperature measurements suspected to be lowered by infiltration of seawater, p. 51.

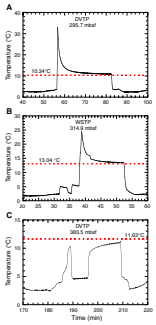

F30. Temperatures vs. depth, p. 52.

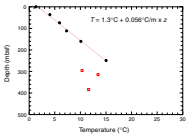

F31. Pressure record from the DVTP-P run at 248.5 mbsf, p. 53.

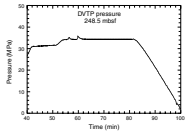

F32. Three-dimensional seismic reflection line, p. 54.

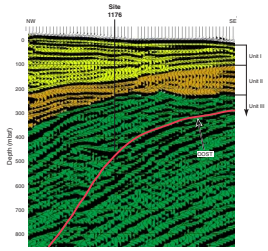

REFERENCES

Cande, S.C., and Kent, D.V., 1995. Revised calibration of the geomagnetic polarity timescale for the Late Cretaceous and Cenozoic. *J. Geophys. Res.,* 100:6093–6095.

Champion, D.E., Lanphere, M.A., and Kuntz, M.A., 1988. Evidence for a new geomagnetic reversal from lava flows in Idaho: discussion of short polarity reversals in the Brunhes and Late Matuyama polarity chrons. *J. Geophys. Res.,* 93:11667–11681.

Gartner, S., 1977. Calcareous nannofossil biostratigraphy and revised zonation of the Pleistocene. *Mar. Micropaleontol.,* 2:1–25.

Martini, E., 1971. Standard Tertiary and Quaternary calcareous nannoplankton zonation. *In* Farinacci, A. (Ed.), *Proc. 2nd Int. Conf. Planktonic Microfossils Roma:* Rome (Ed. Tecnosci.), 2:739–785.

Parkes, R.J., Cragg, B.A., Bale, S.J., Getliff, J.M., Goodman, K., Rochelle, P.A., Fry, J.C., Weightman, A.J., and Harvey, S.M., 1994. A deep bacterial biosphere in Pacific Ocean sediments. *Nature,* 371:410–413.

Young, J.R., 1998. Neogene. *In* Bown, P.R. (Ed.), *Calcareous Nannofossil Biostratigraphy* (Vol. 8): Dordrecht (Kluwer Academic), 225–265.

Figure F1. Stratigraphic column for Site 1176, showing lithostratigraphic units, ages, and characteristic lithologies.

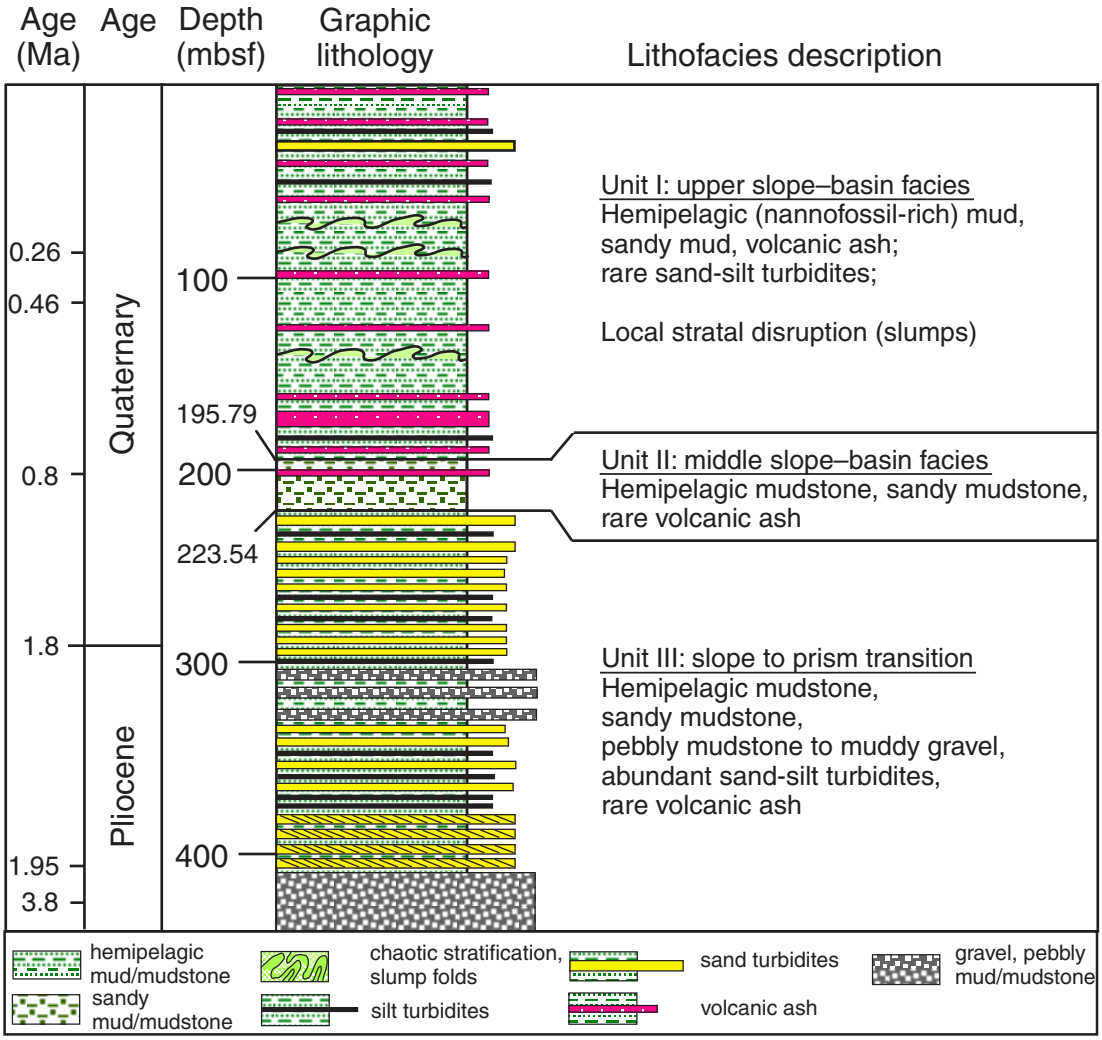

Figure F2. Chaotic and inclined interbeds, probably due to slump folding; lithologies consist of brown volcanic ash and silty clay in Unit I (interval 190-1176A-7H-3, 0–50 cm).

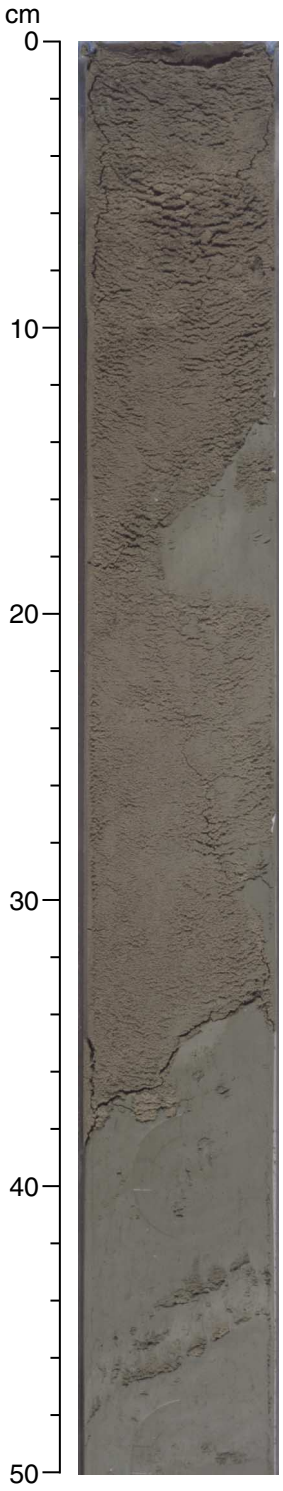

Figure F3. Distribution and thickness of volcanic ash layers at Site 1176.

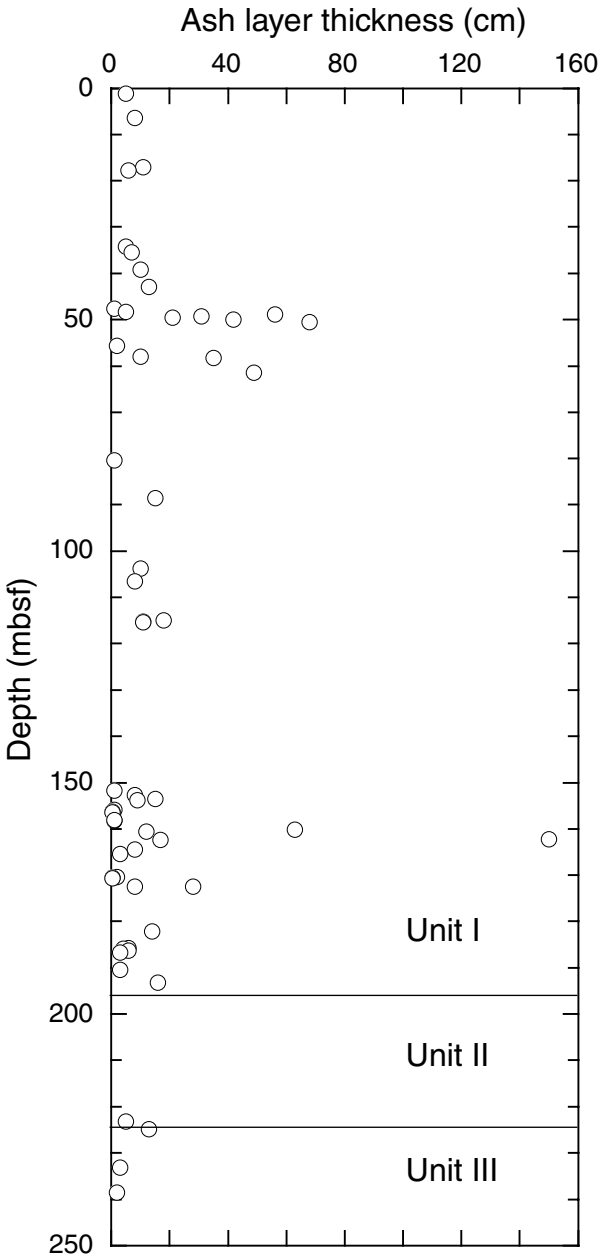

Figure F4. Dark gray to light-colored volcanic ash from Unit I with a sharp base and diffuse top (interval 190-1176A-21X-2, 35–55 cm). The base of the ash contains pyroxene crystals.

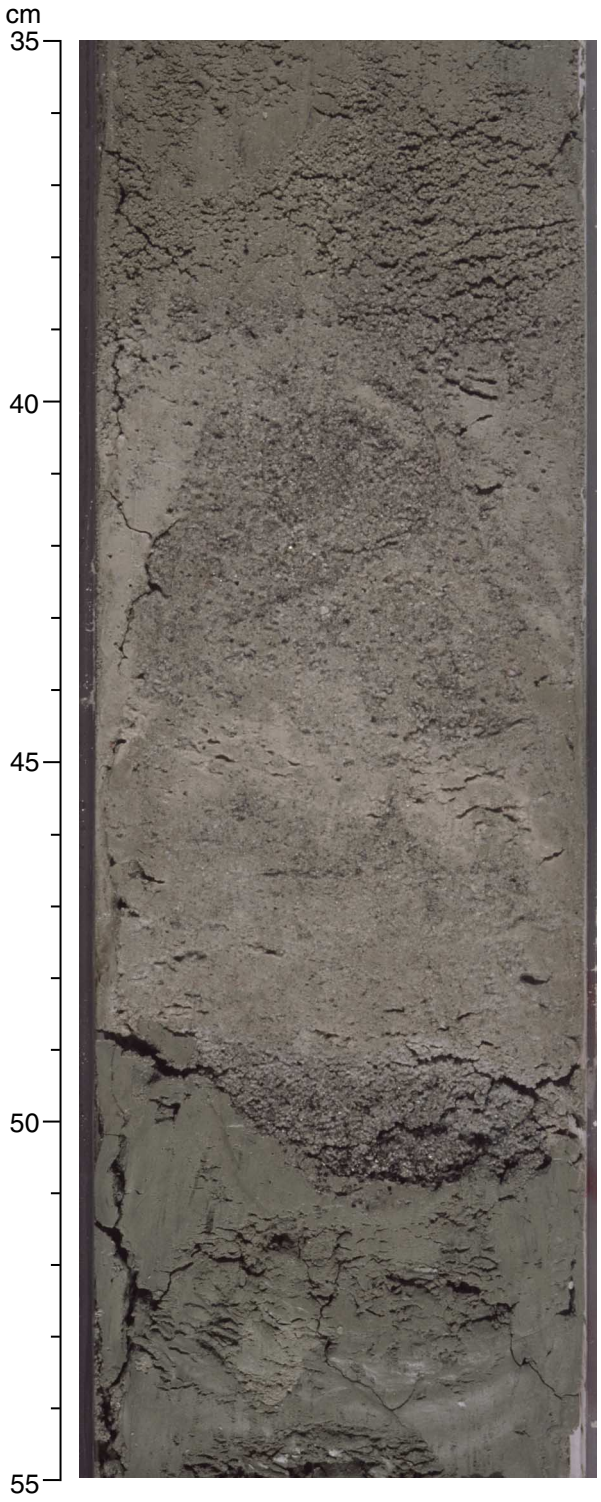

Figure F5. Thickening-upward cycle of silty sand turbidites and gray-green silty clay from Unit I (interval 190-1176A-5H-3, 35–70 cm).

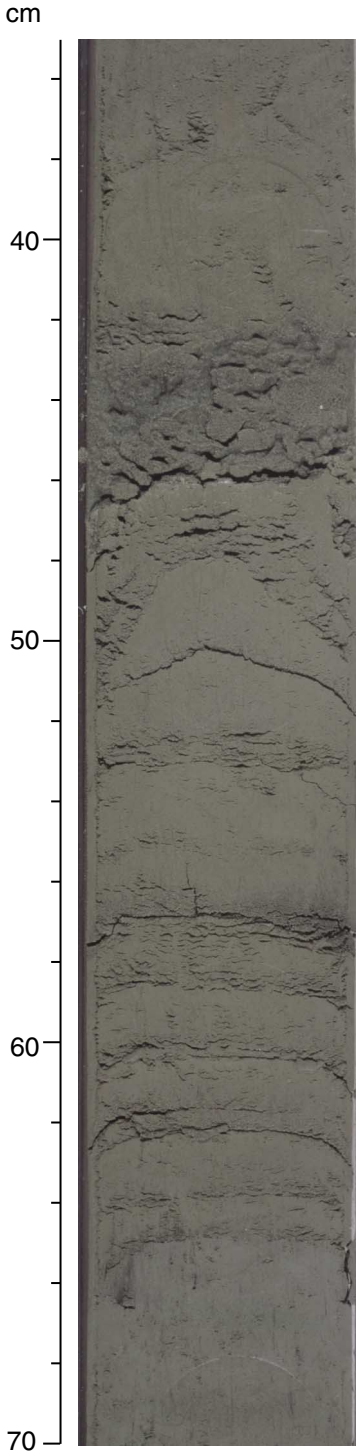

Figure F6. Cross-laminae in silty sand from Unit III (interval 190-1176A-40X-CC, 10–25 cm).

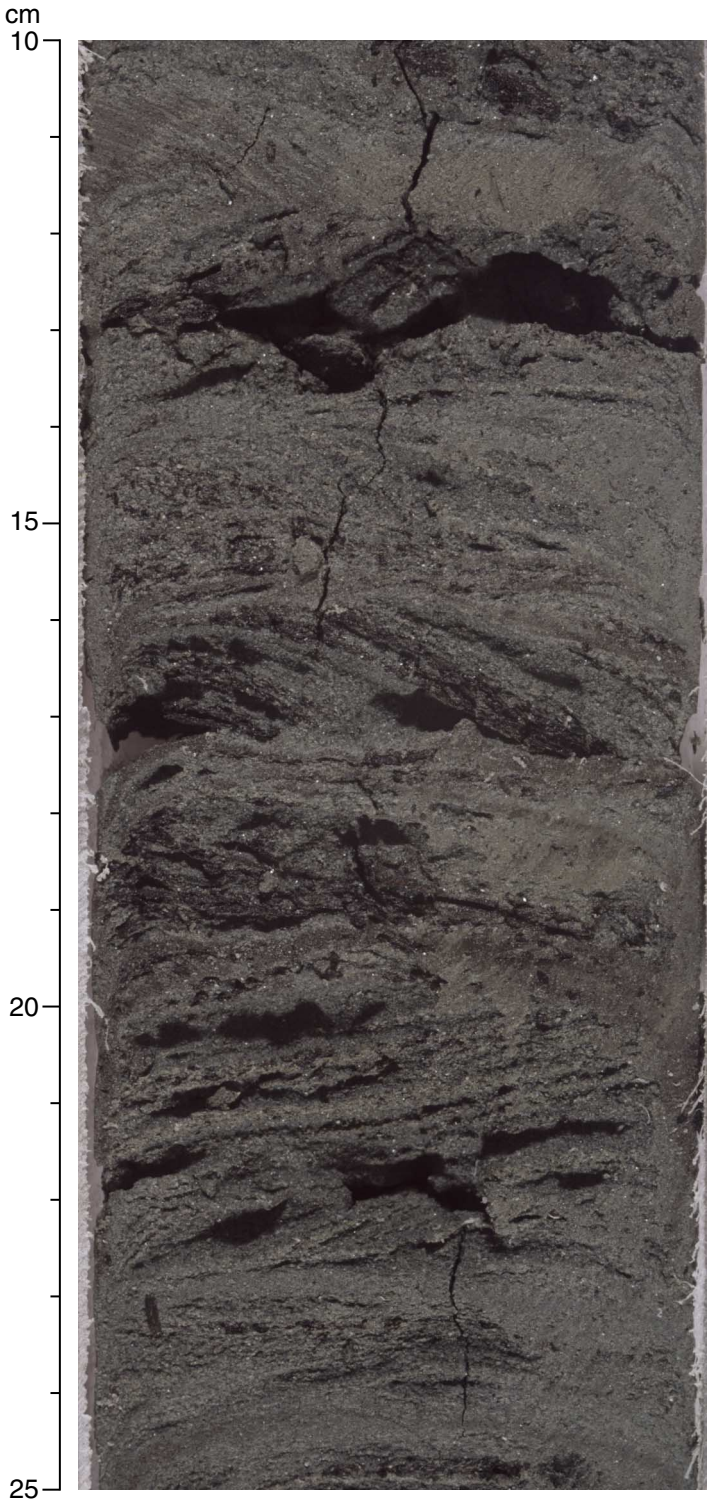

Figure F7. Pebbles and gravel of quartz and lithic clasts in muddy matrix from Unit III (interval 190-1176A-47X-CC, 0–28 cm).

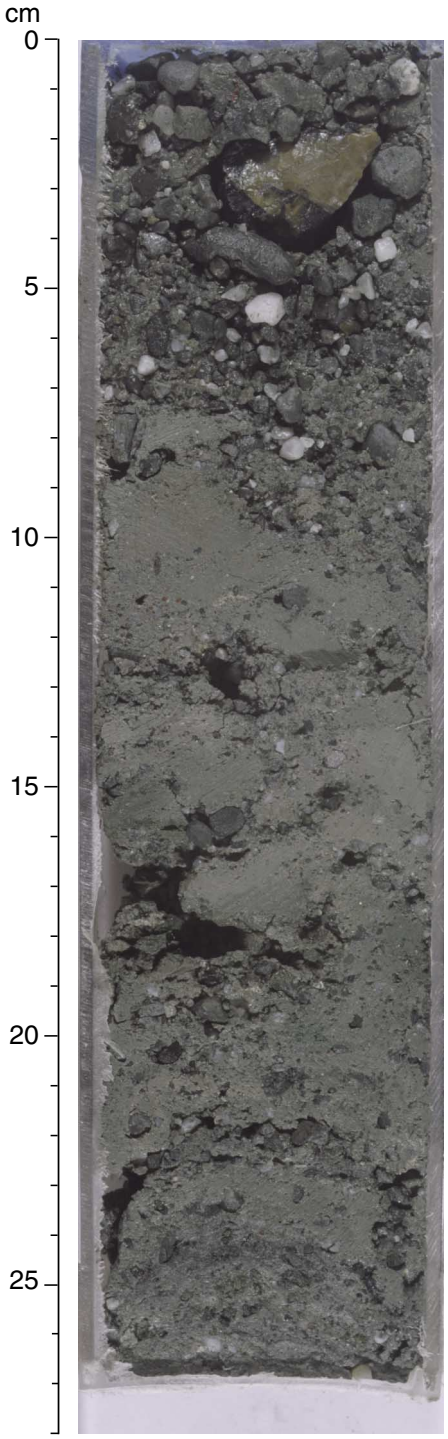

Figure F8. Relative abundance of total clay minerals, quartz, plagioclase, and calcite at Site 1176 based on X-ray diffraction analyses of randomly oriented bulk-sediment powders.

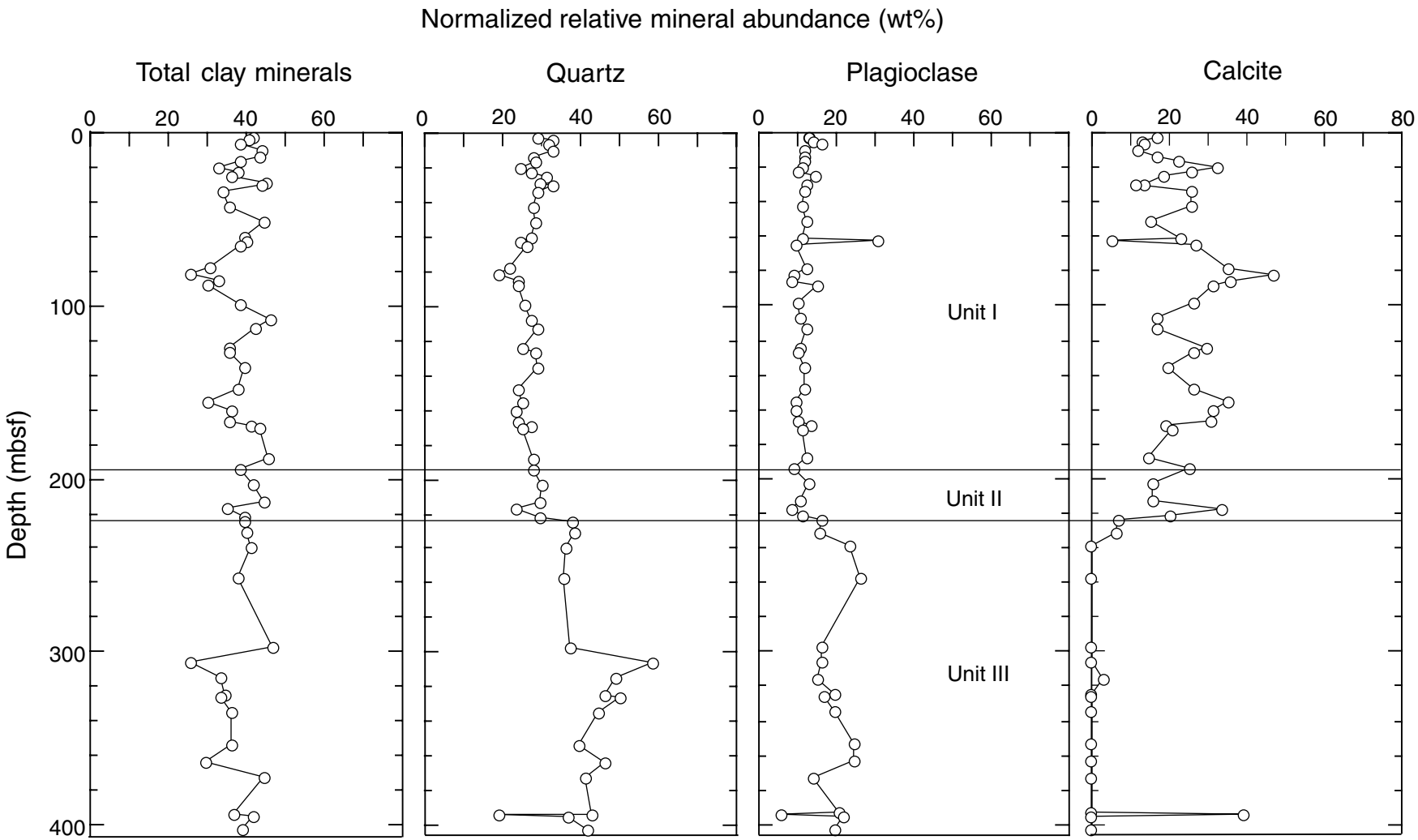

Figure F9. Bedding dips relative to the core liner plotted against depth in comparison with lithostratigraphic divisions. Distribution of structures is shown to the right along with observed fault displacements (in millimeters).

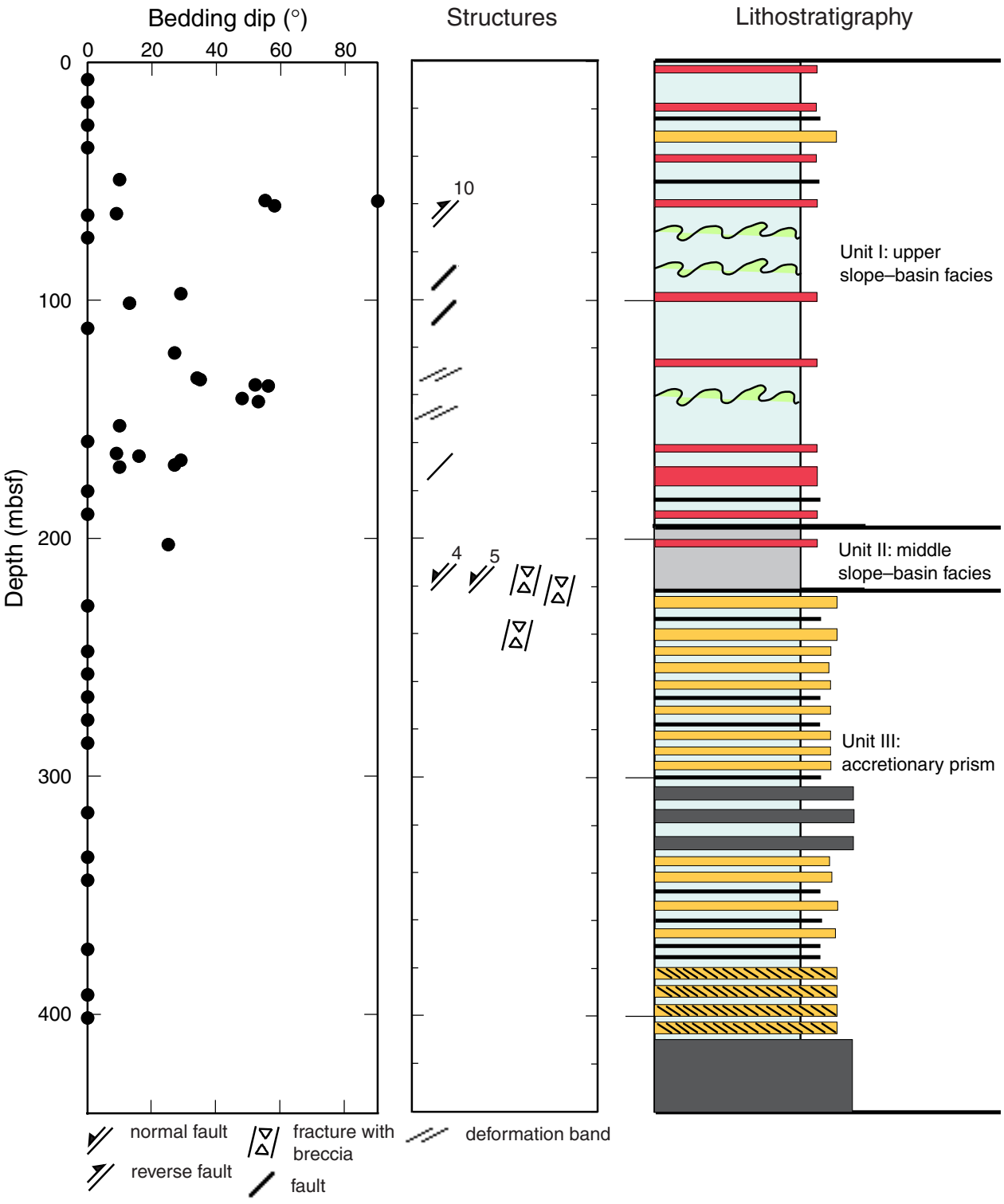

Figure F10. Equal-area lower-hemisphere stereographic projections of bedding in Units I and II after paleomagnetic reorientation. **A.** Poles to bedding planes. Note that the many horizontal bedding planes overlap as one point at the center of the plot. **B.** Contoured poles to bedding planes. Number of points = 27, contour interval = 2.0%/1% area.

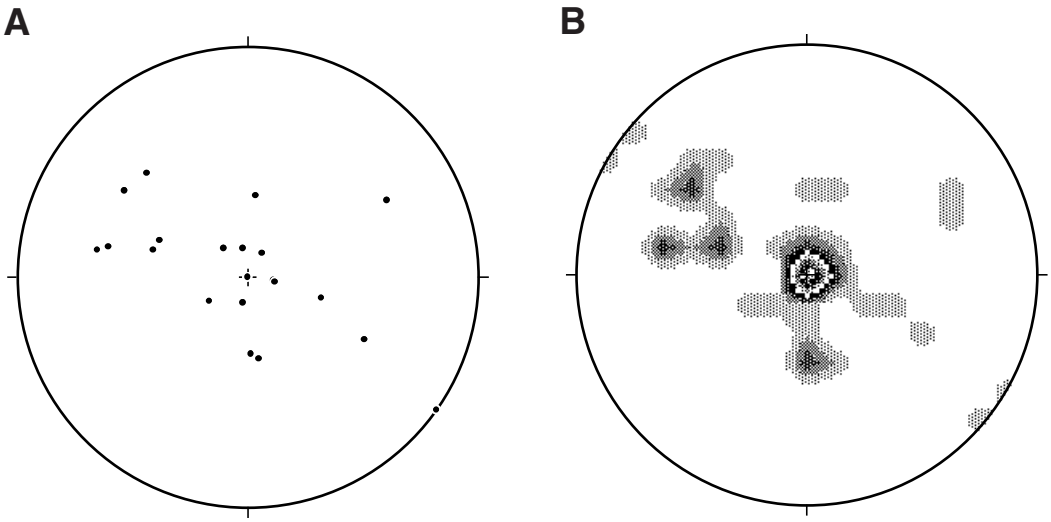

Figure F11. Examples of small faults in (**A**) Section 190-1176A-7H-6 (63 mbsf) and (**B**) Section 190-1176A-12H-4 (107 mbsf). Note both fault sets are found in very soft, unconsolidated sediments.

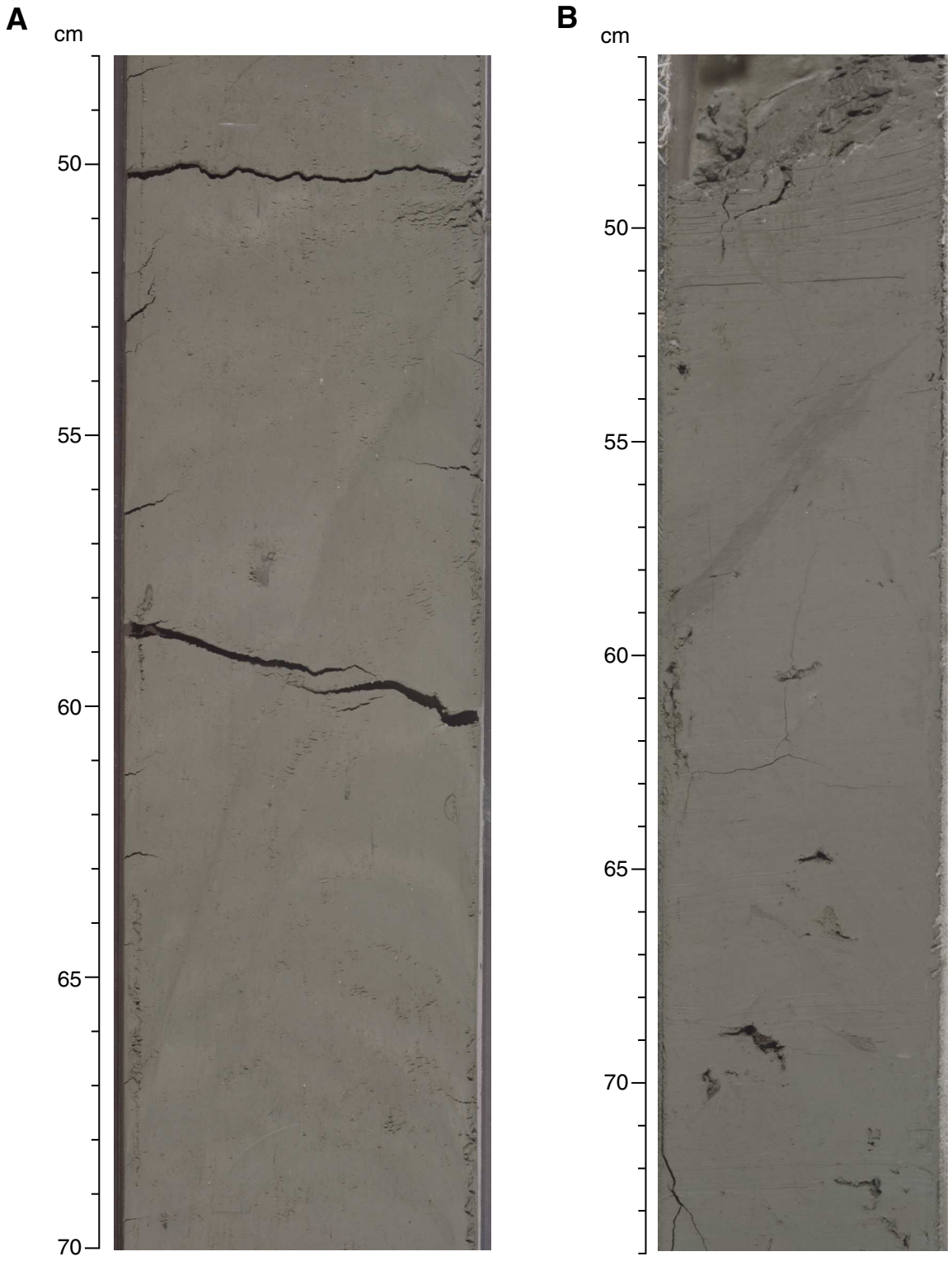

Figure F12. Uncalibrated gas-permeability results from Site 1176.

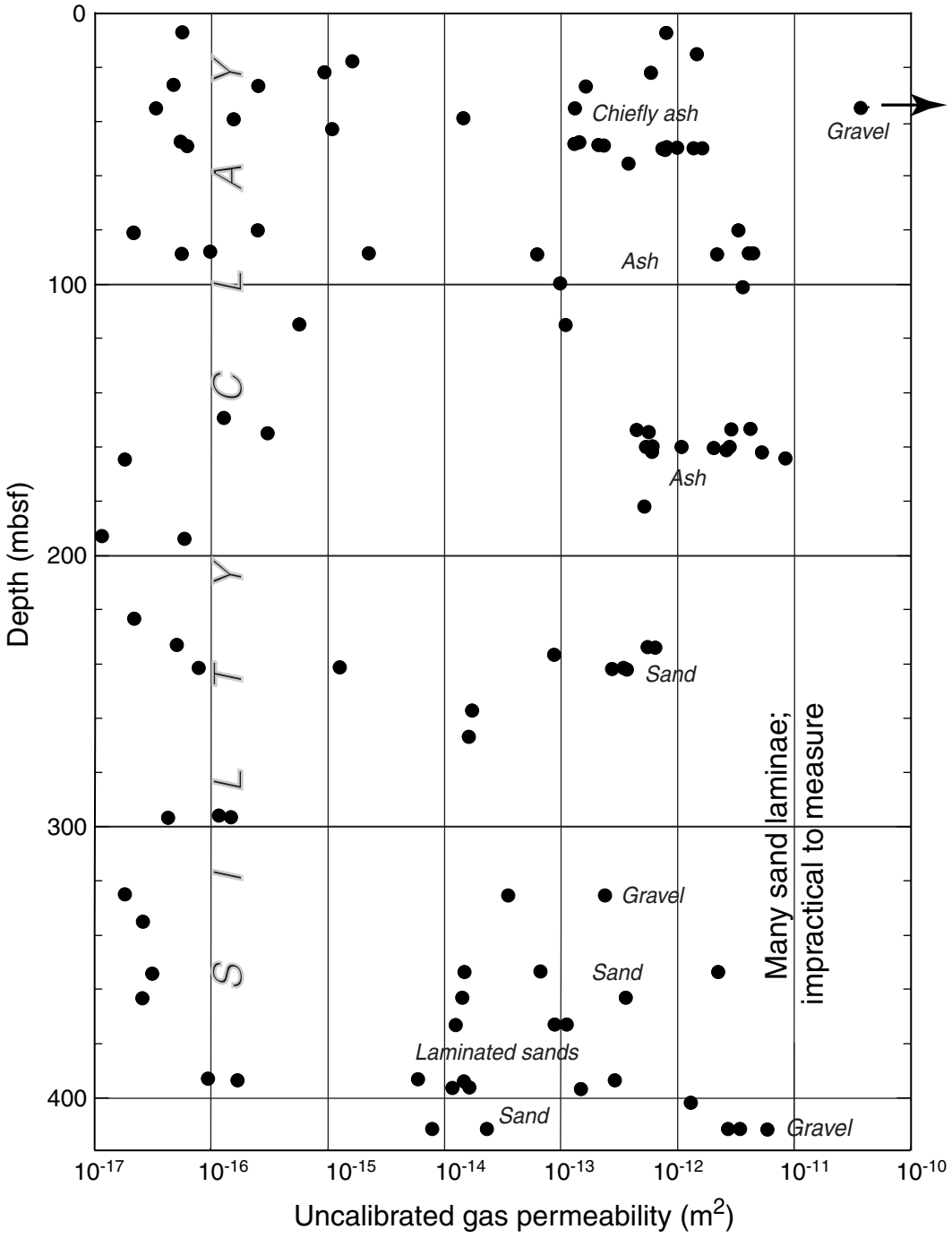

Figure F13. Paleomagnetic declination, inclination, and intensity after AF demagnetization at 30 mT at Hole 1176A. Note that declinations from 16.05 to 204.54 mbsf were corrected using Tensor tool orientation data.

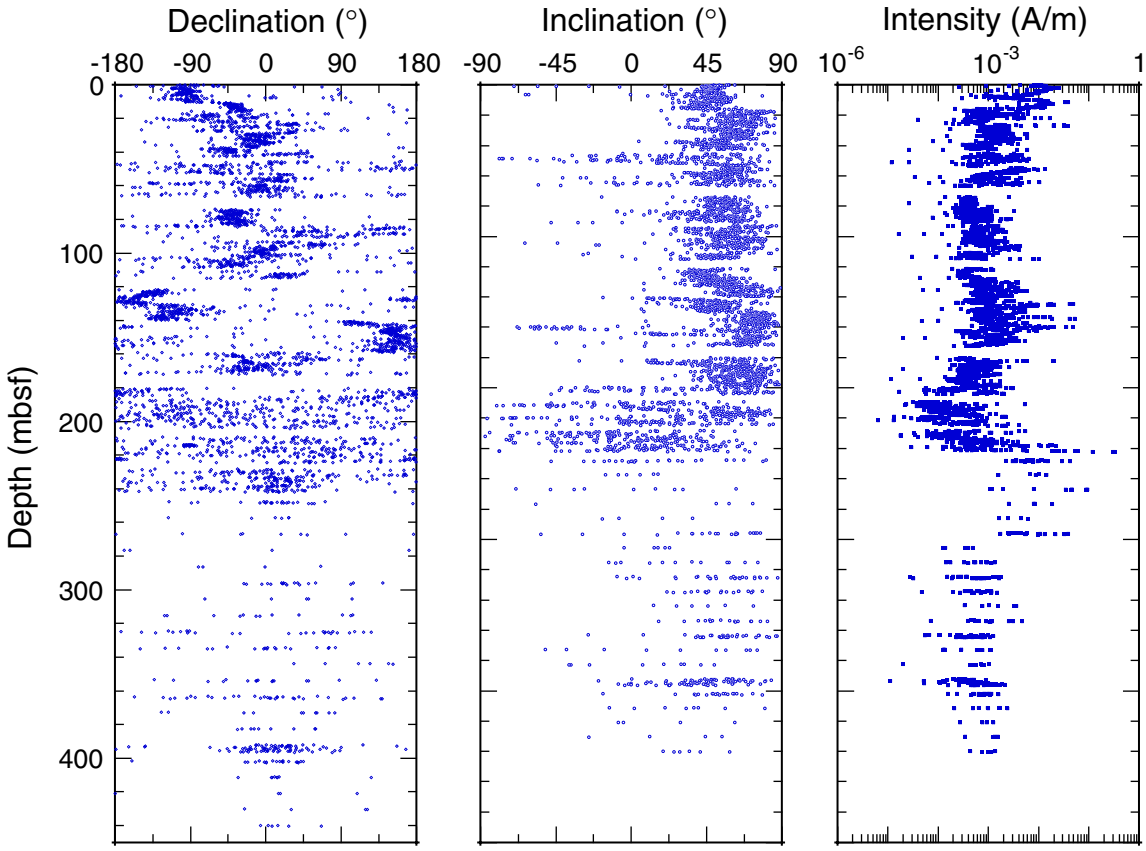

Figure F14. Site 1176 magnetostratigraphy. Black = normal polarity, white = reversed polarity, gray = unknown polarity, ? = questionable correlation.

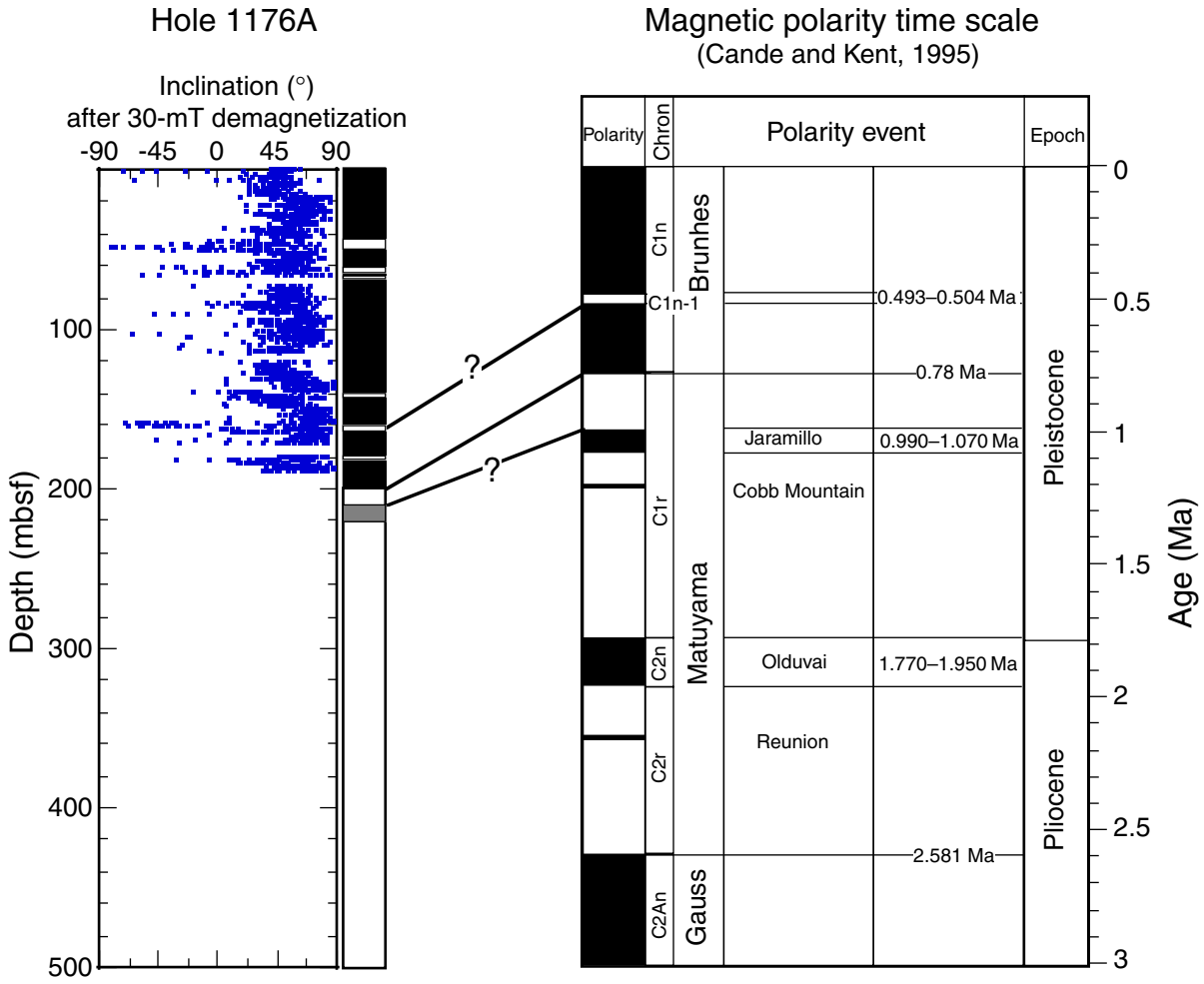

Figure F15. Site 1176 age-depth plot obtained from magnetostratigraphy and biostratigraphy. Black = normal polarity, white = reversed polarity, gray = unknown polarity, J = Jaramillo.

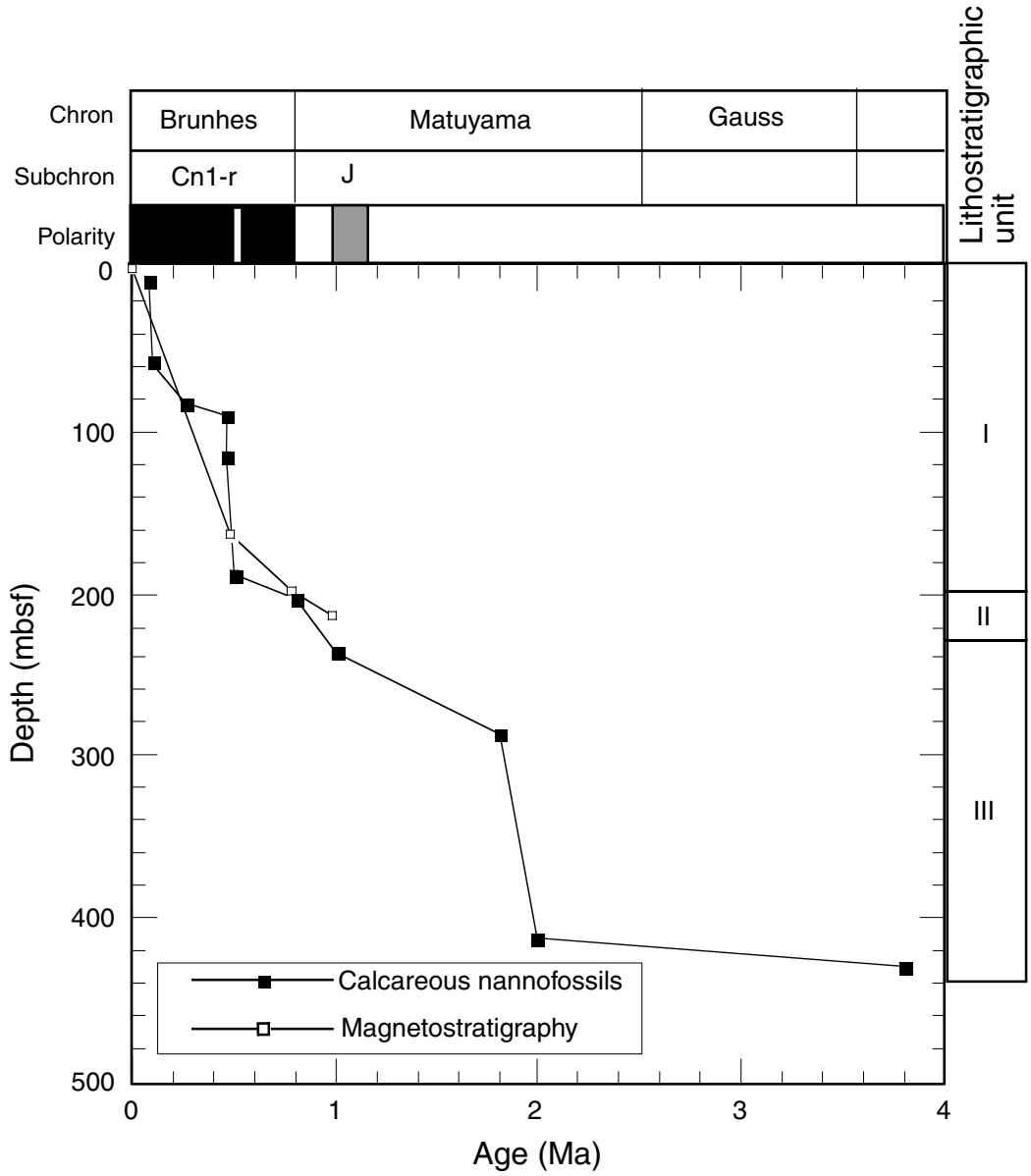

Figure F16. Pore fluid compositions as a function of depth, Hole 1176A. Solid horizontal lines = lithostratigraphic boundaries.

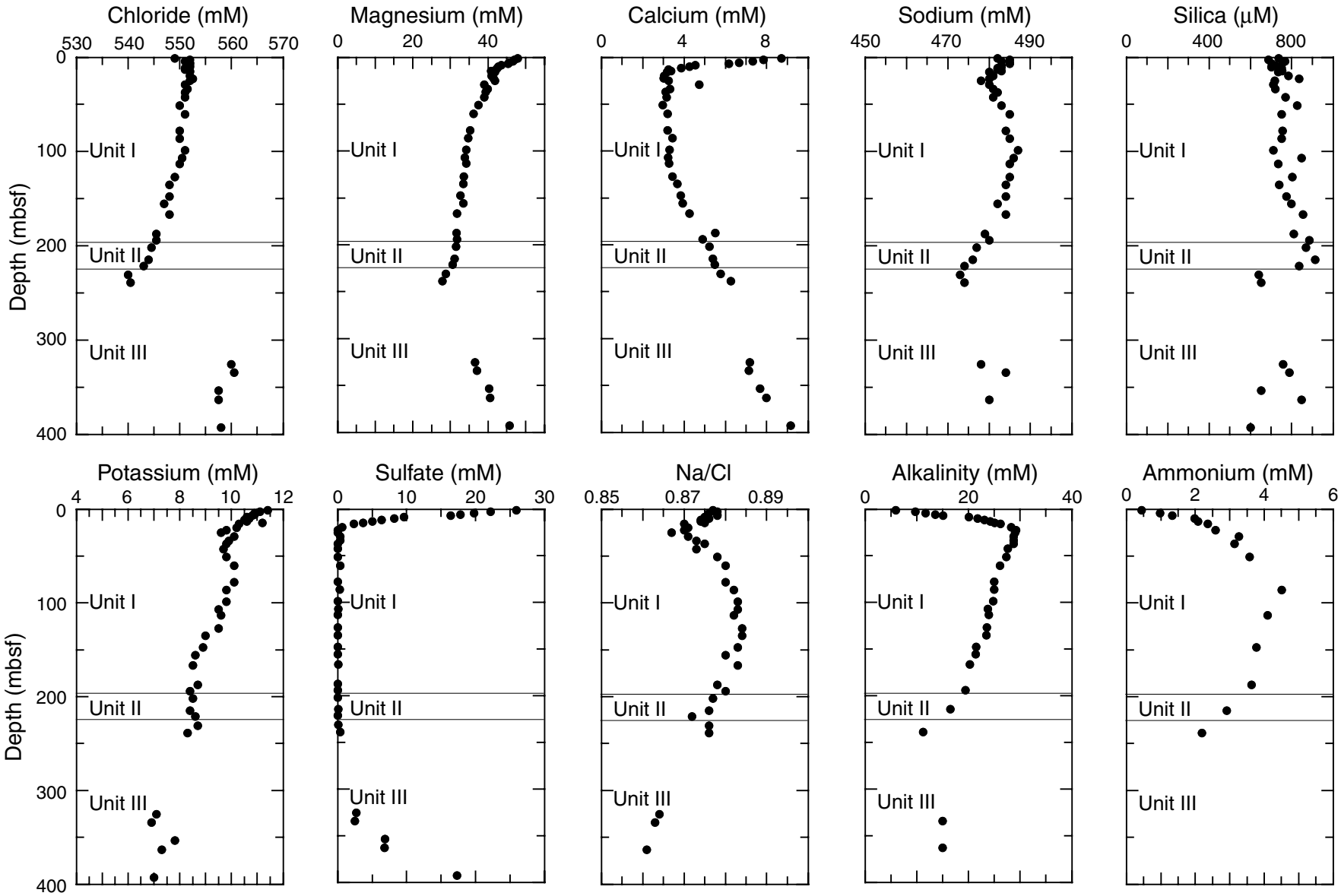

Figure F17. The compositions, concentrations, and distributions of headspace gases measured in sediments. **A.** Hole 1175A. **B.** Site 1176. Note the striking similarity between values measured at the two sites.

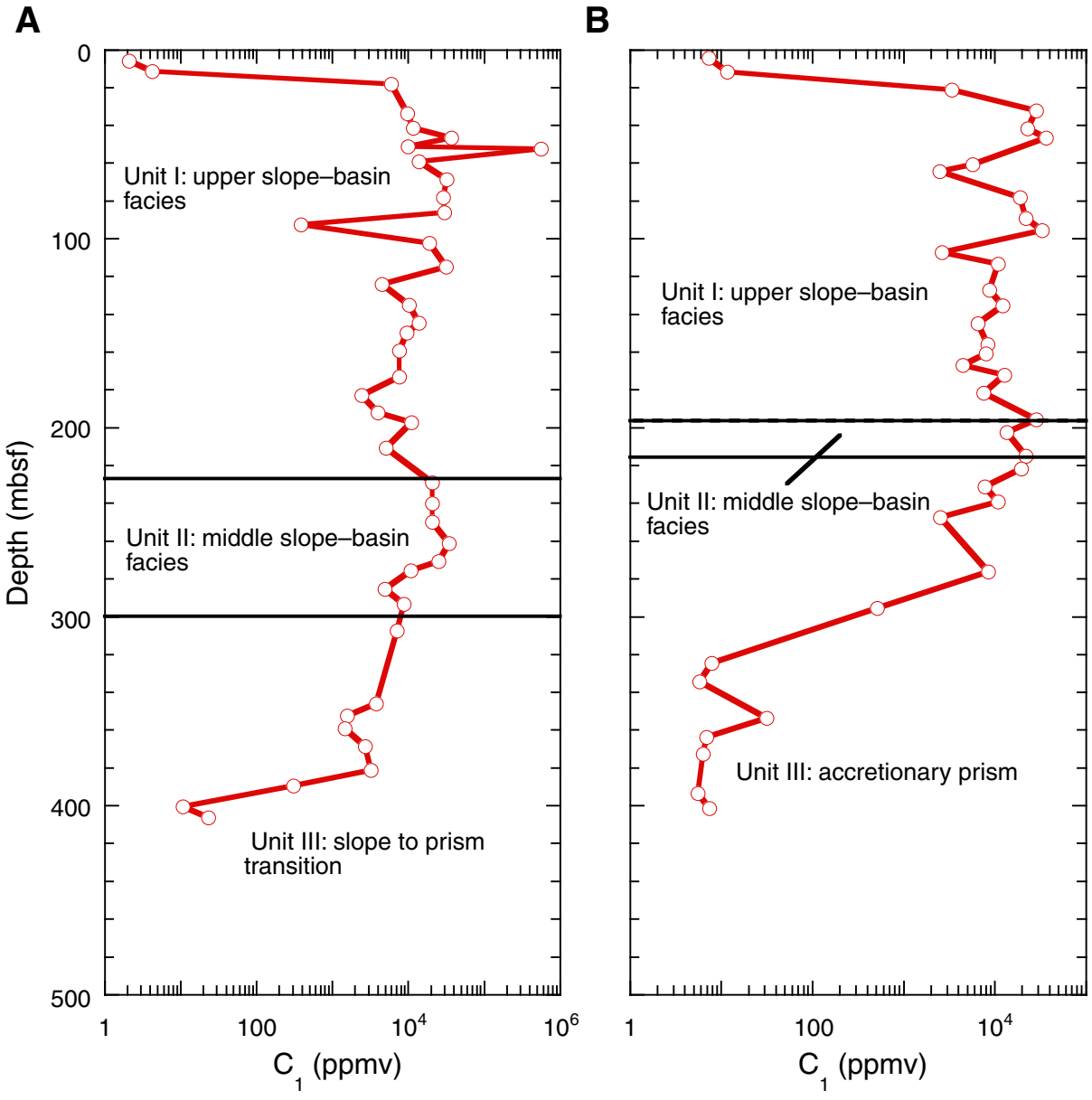

Figure F18. TOC, sulfur, and methane in sediment samples from Hole 1176A. The TOC and sulfur concentrations display a similar trend and track one another throughout the lower 200 m of Hole 1176A.

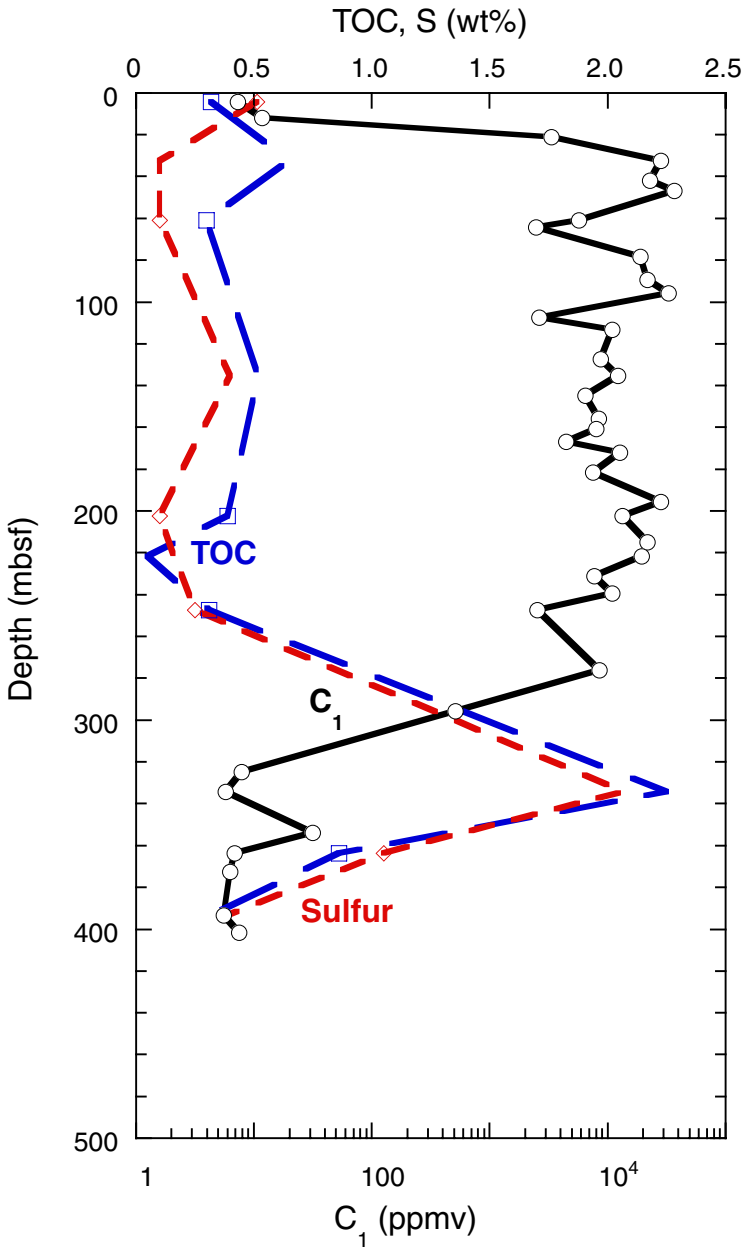

Figure F19. Depth distribution of total bacterial populations in sediment samples from Hole 1176A. The curved dashed line represents a general regression line of bacterial numbers vs. depth in deep-sea sediments (Parkes et al., 1994), with 95% upper and lower prediction limits shown by the curved lines of longer dashes. The shaded area to the left of the figure indicates levels where bacterial populations are too low to be detected with the acridine orange direct count technique; the detection limit was 6×10^4 cells/cm^3.

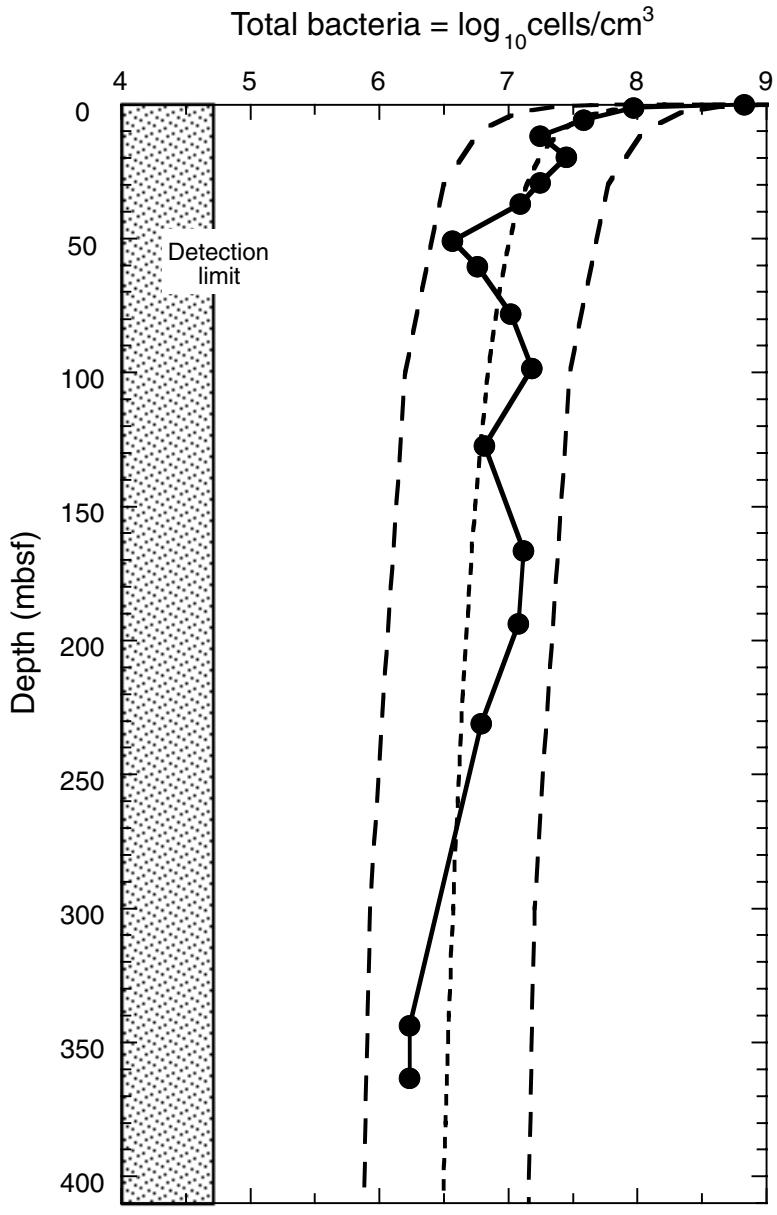

Figure F20. A. Site 1176 bulk-density measurements. Lithostratigraphic Units I (upper slope–basin facies), II (middle slope–basin facies), and III (accretionary prism facies) are indicated. **B.** MST GRA density data and mass/volume bulk density. **C.** Grain density. **D.** Porosity.

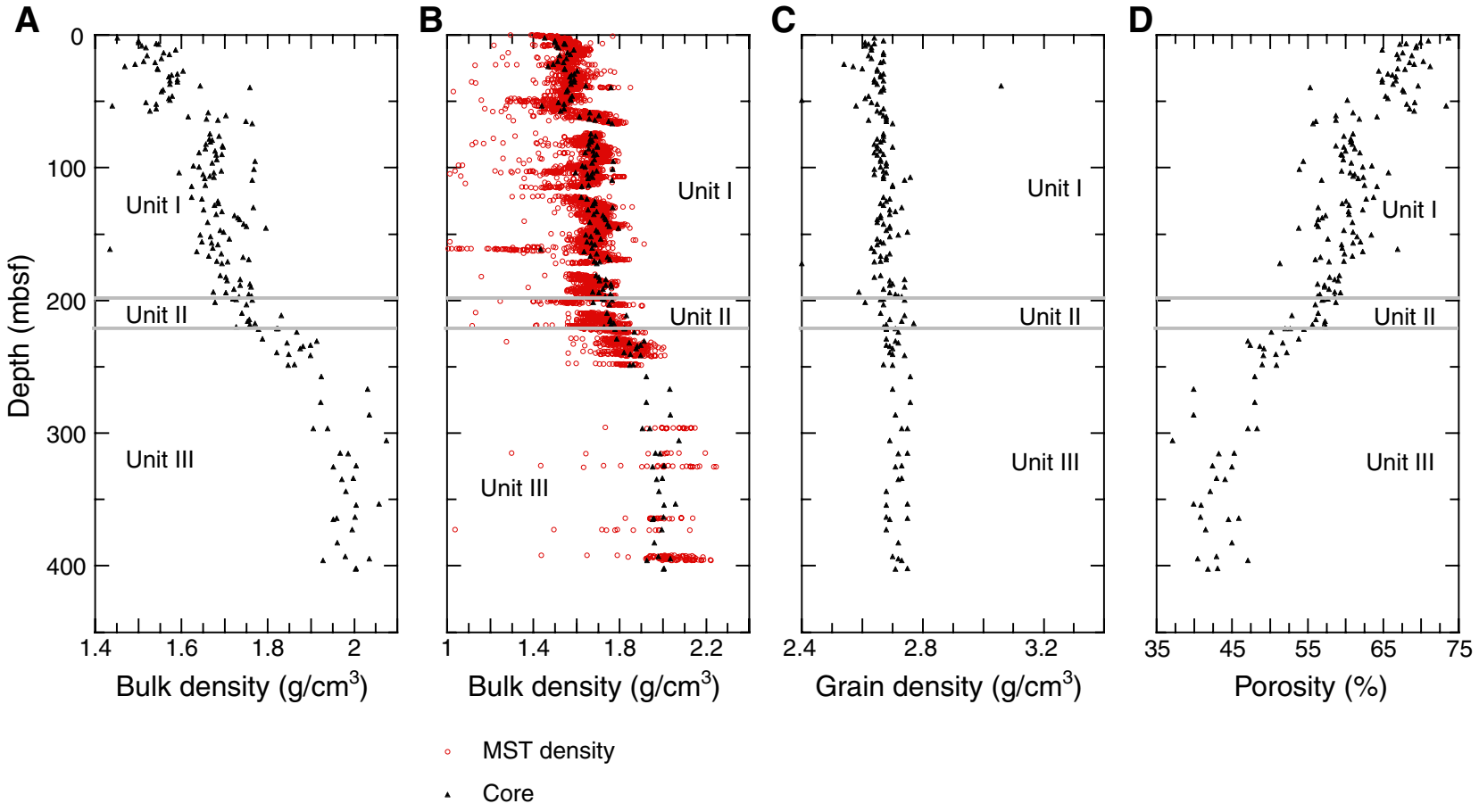

Figure F21. Site 1176 undrained peak shear strength.

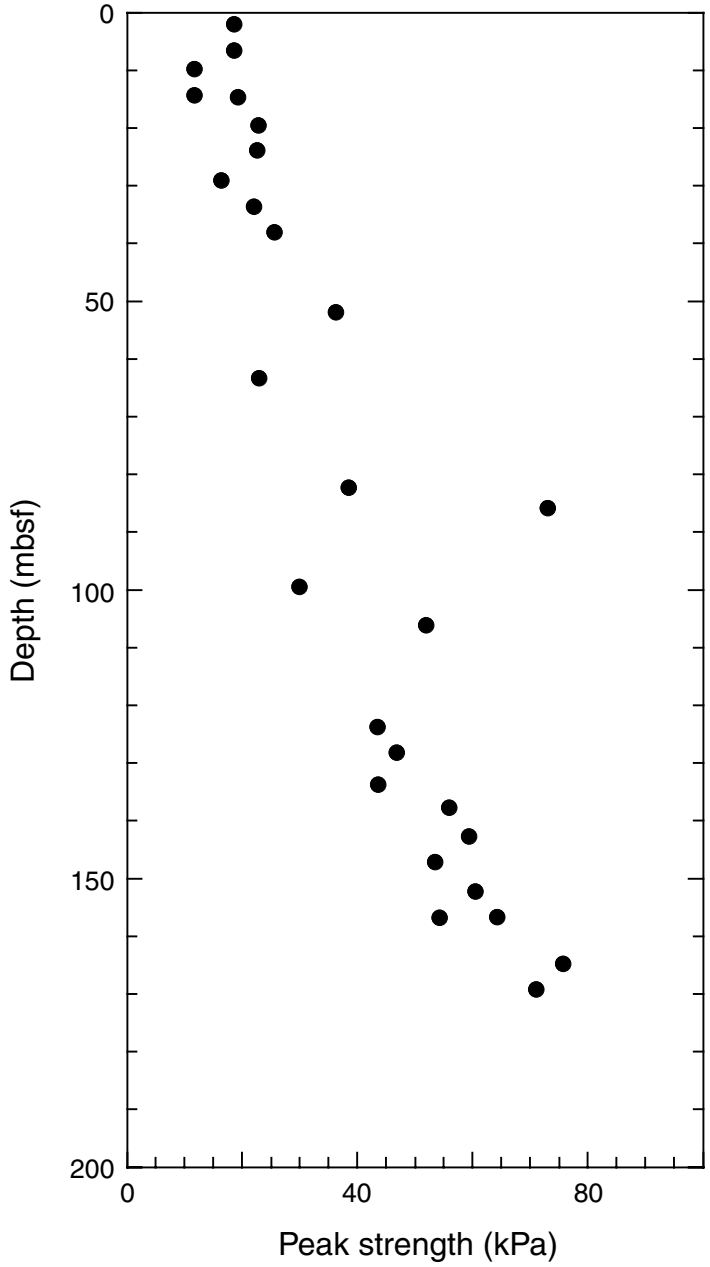

Figure F22. A. Site 1176 thermal conductivity. **B.** Observed (triangles) and projected (dashed line) temperatures.

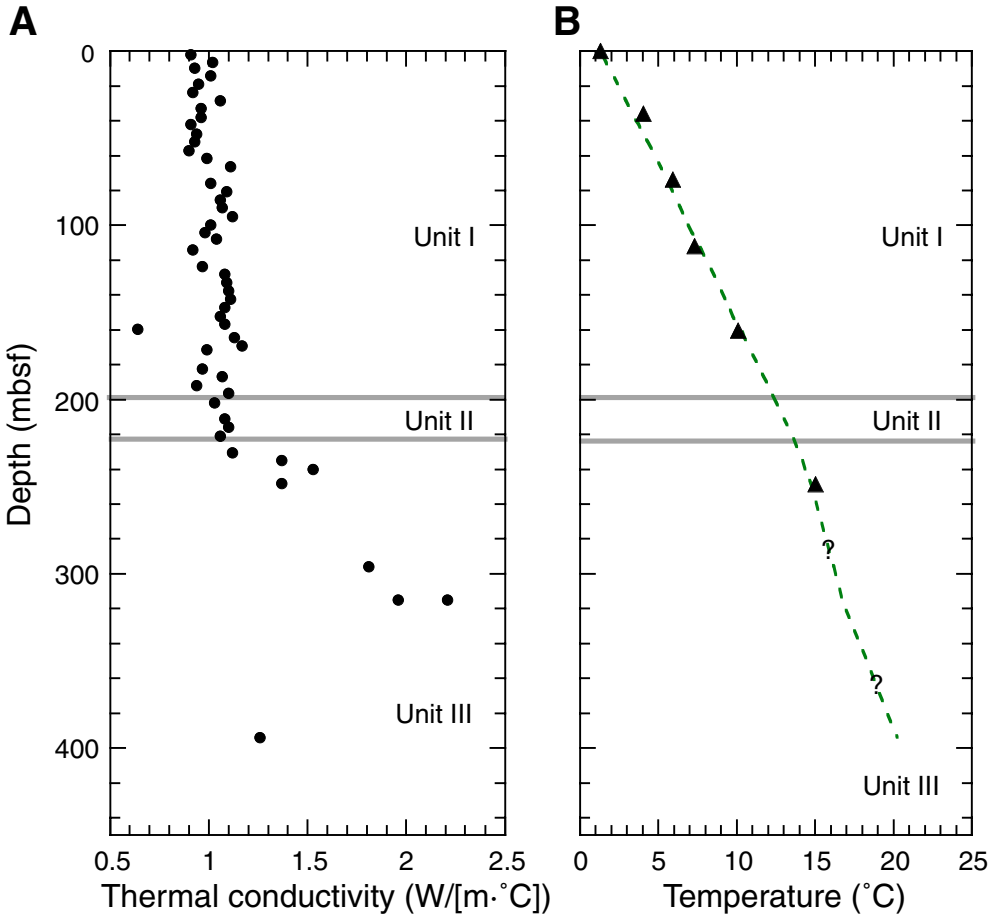

Figure F23. A. Site 1176 *P*-wave velocity. **B.** Impedance computed from velocity and bulk-density data.

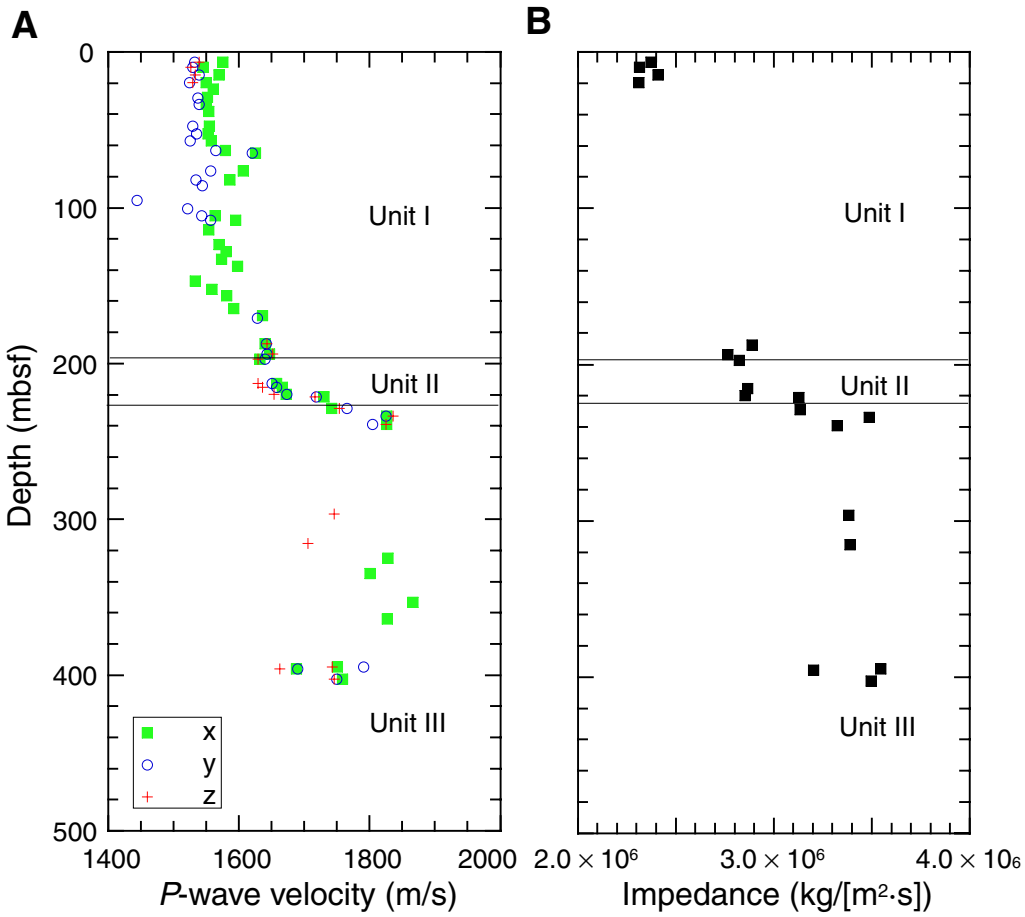

Figure F24. Site 1176 formation factor. Needle-probe measurements on APC cores were performed in the y- (across core) and z- (along core) directions. Measurements on cut samples were performed in the x- and y- (orthogonal to core) and z- (parallel to core) directions.

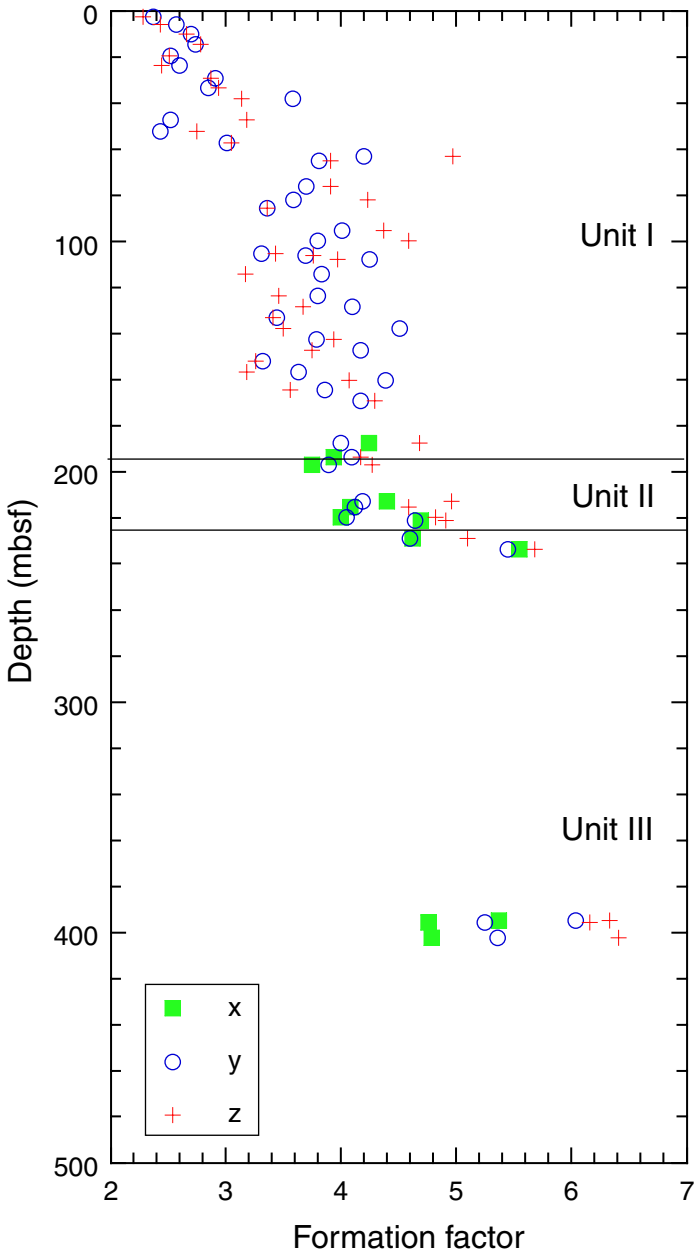

Figure F25. Site 1176 magnetic susceptibility.

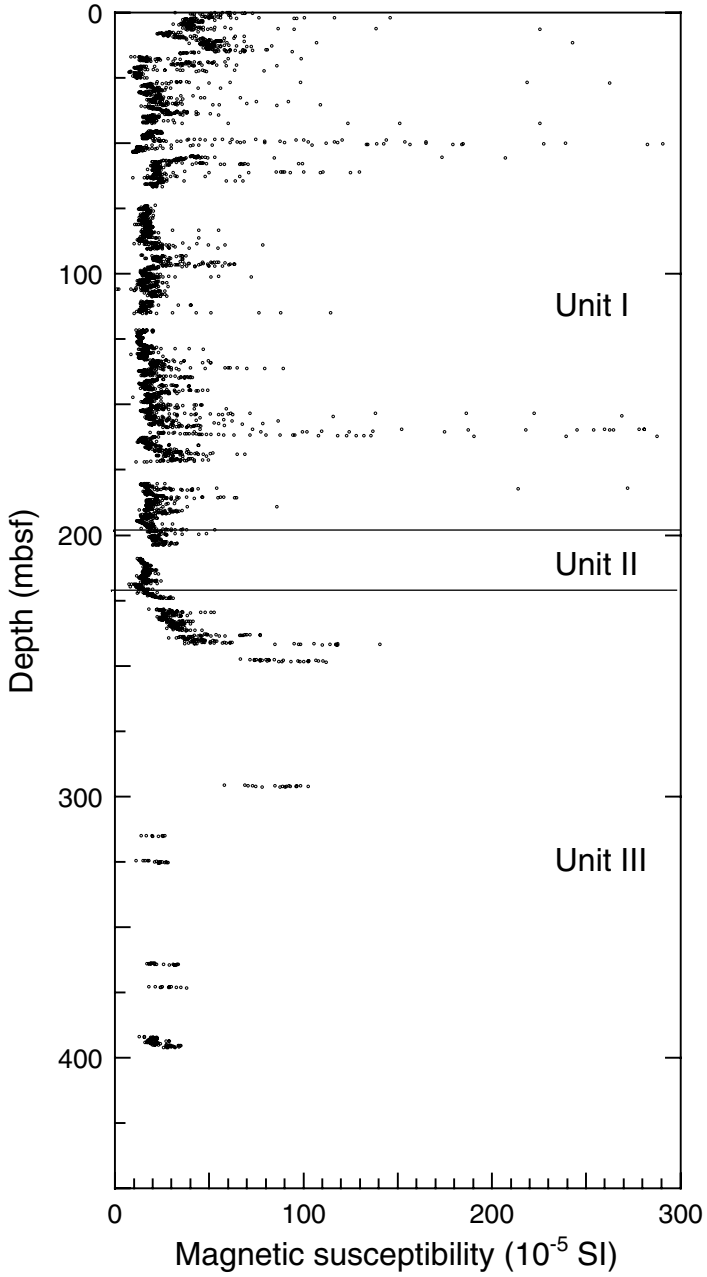

Figure F26. Site 1176 natural gamma ray.

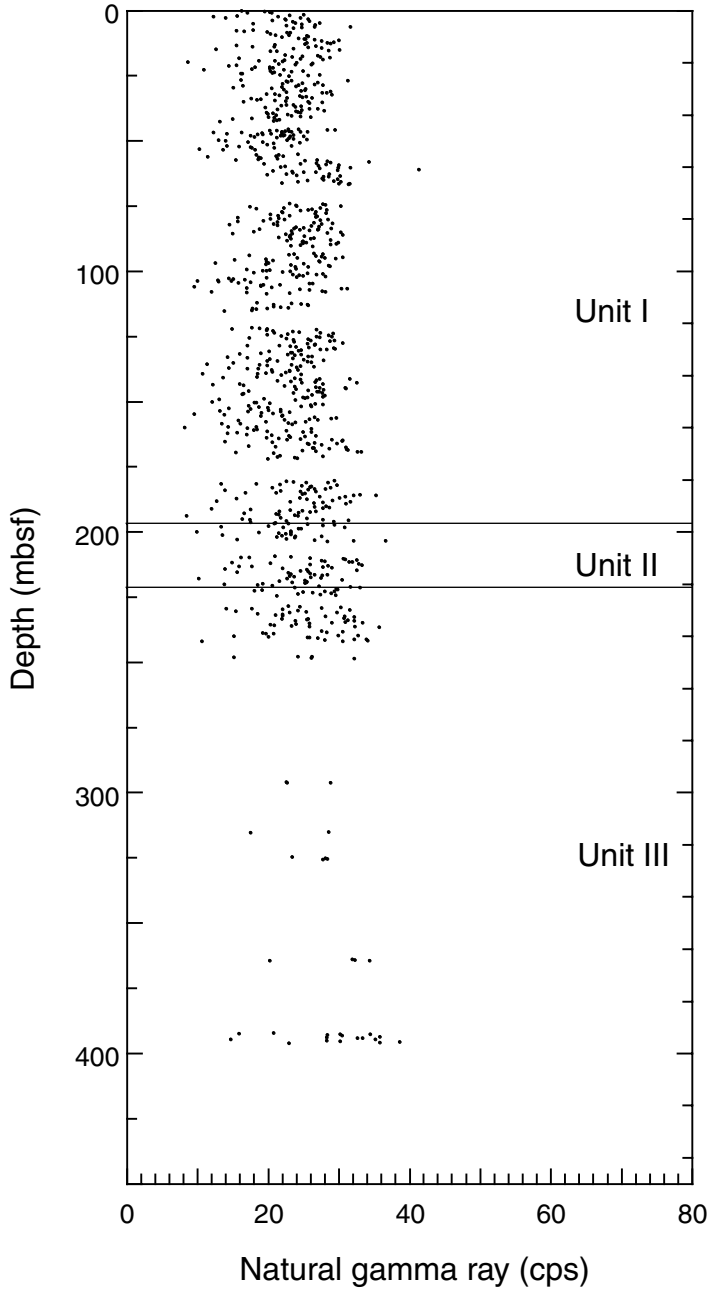

Figure F27. Temperatures measured during the deployment of the APC temperature tool in Hole 1176A (**A**) at the bottom of Core 190-1176A-4H and (**B**) at the bottom of Core 8H, and (**C**) at the bottom of Core 14H. Dashed lines = extrapolated temperatures, solid line = mudline temperature.

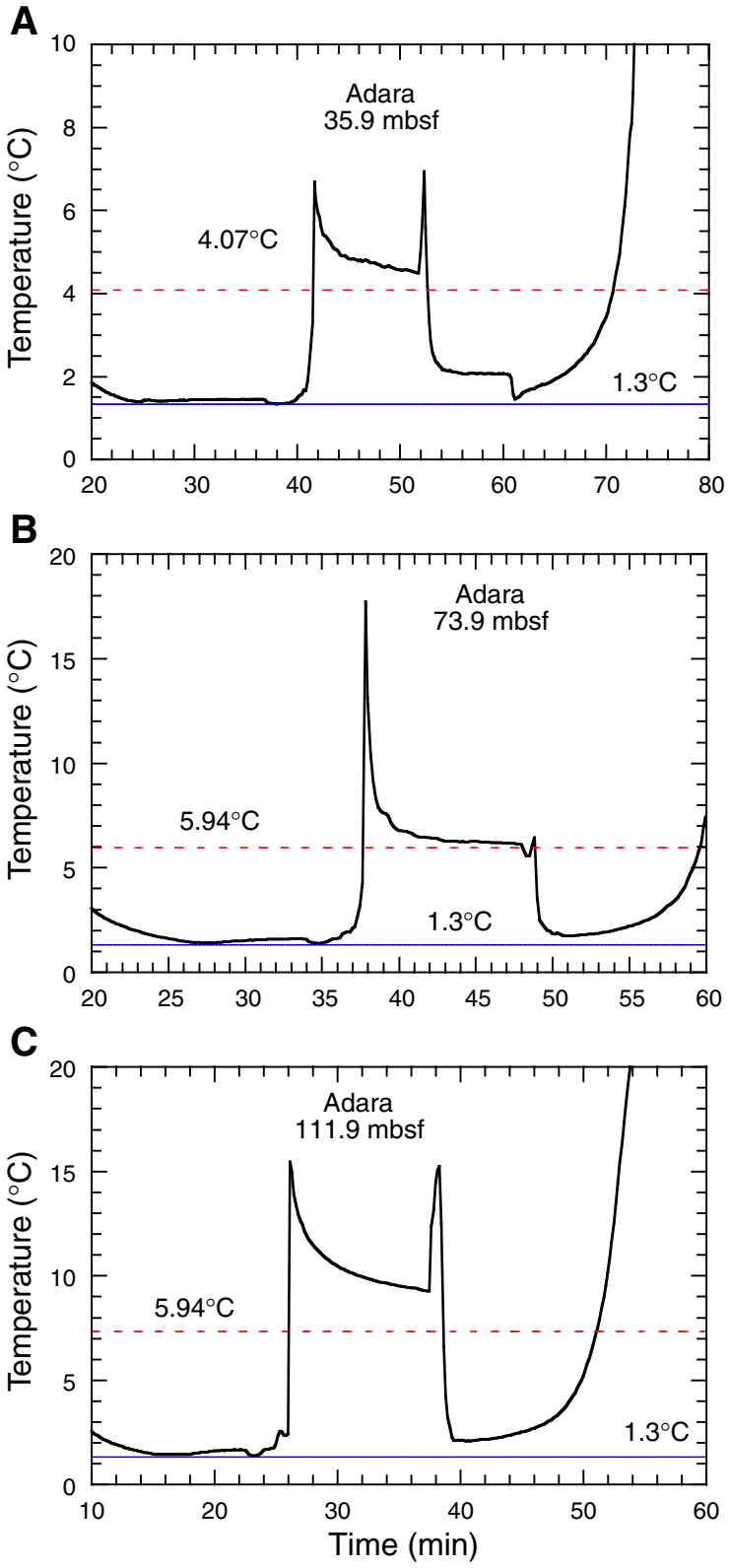

Figure F28. Temperatures measured in Hole 1176A during the DVTP stations (**A**) after Core 190-1176A-18H and (**B**) after Core 28X. Dashed lines = extrapolated in situ temperatures.

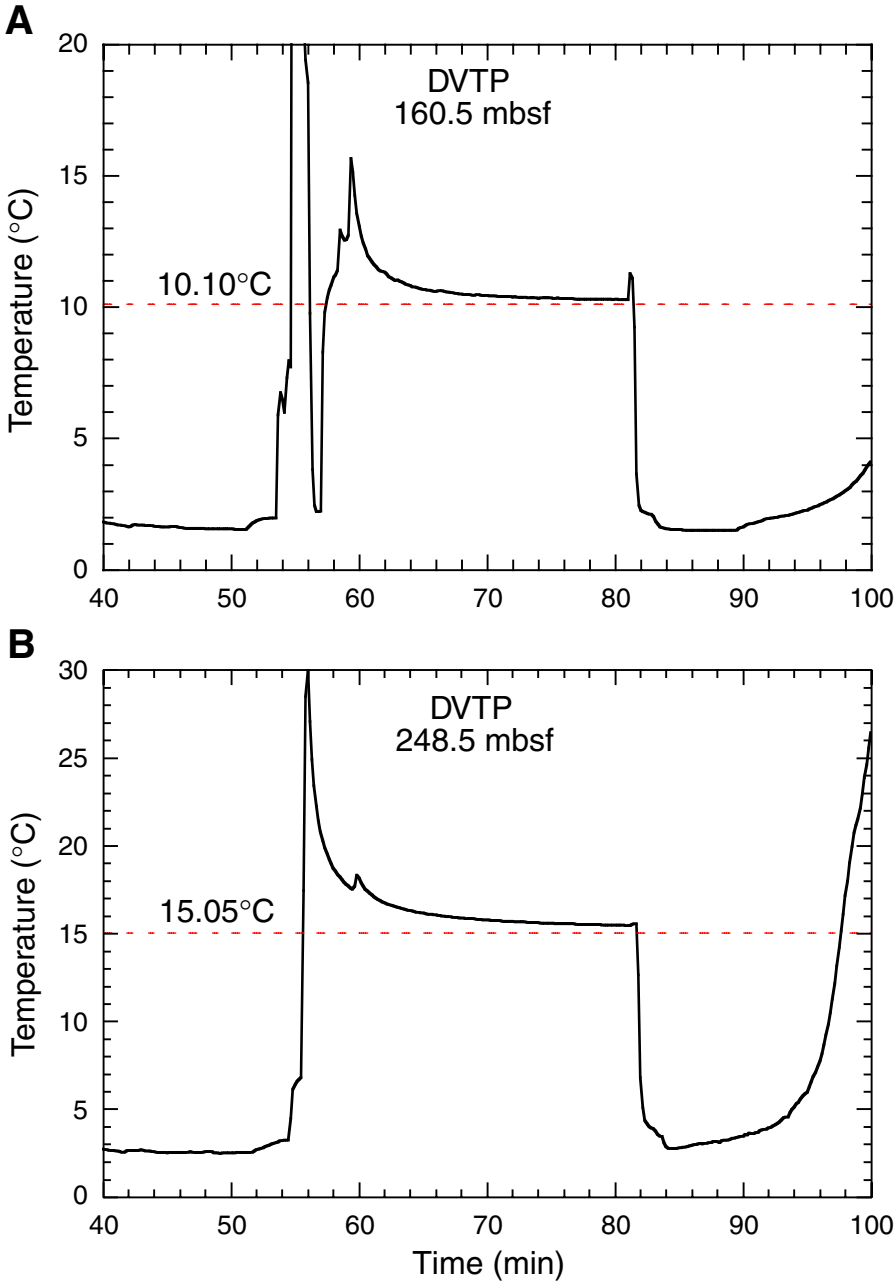

Figure F29. Hole 1176A temperature measurements suspected to be lowered by infiltration of seawater. **A.** DVTP after Core 190-1176A-34X. **B.** WSTP after Core 190-1176A-36A. **C.** DVTP after Core 190-1176A-42X.

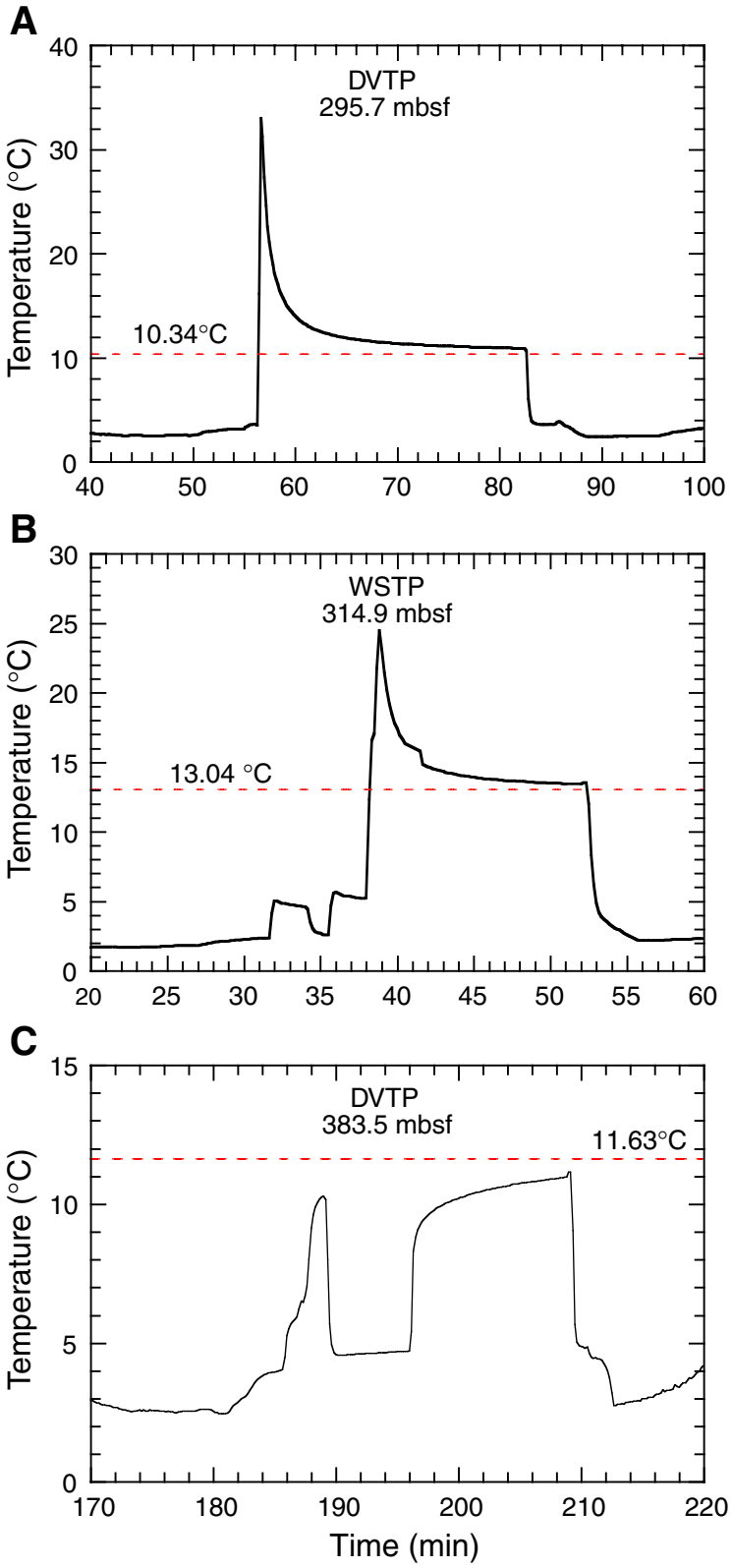

Figure F30. Hole 1176A temperatures vs. depth. Anomalous data are shown by squares. Equation shows the linear best fit for the five reliable measurements. *T* = temperature; *z* = depth (mbsf).

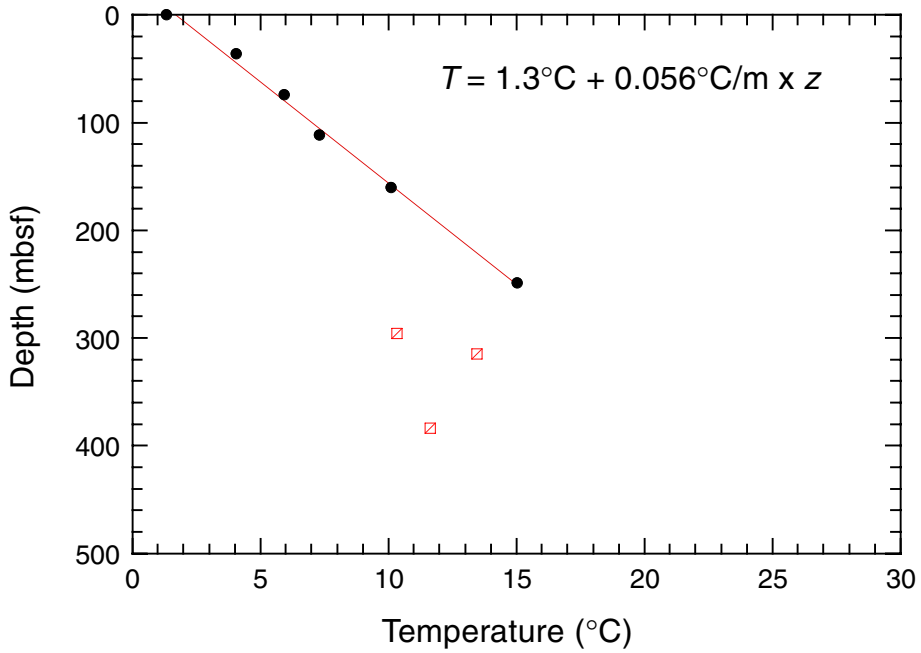

Figure F31. Pressure record from the DVTP run at 248.5 mbsf. Data were corrected for observed zero shift of 4.5 MPa. The DVTP also collected pressures during stations at 295.7 and 383.5 mbsf, but these runs were suspected of being affected by infiltration of bottom water.

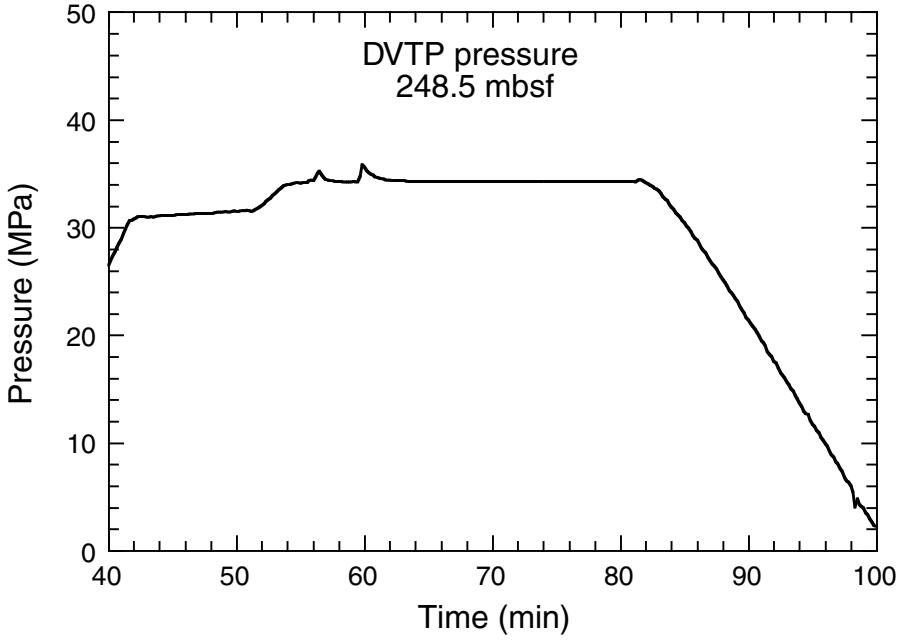

Figure F32. Three-dimensional seismic reflection line 277 across Site 1176. This line has been 3-D stacked and migrated. OOST = out-of-sequence thrust.

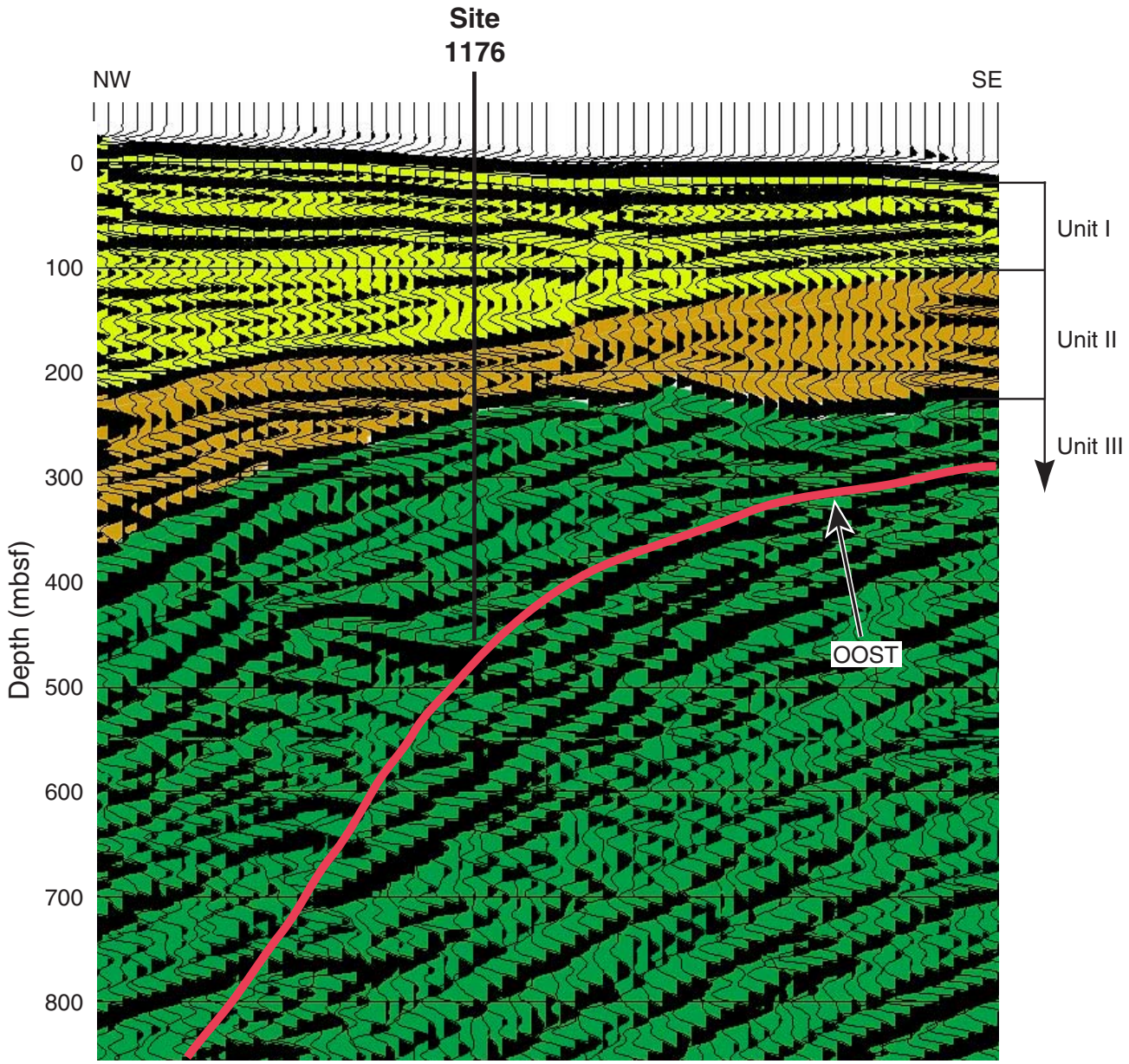

Table T1. Coring summary, Site 1176.

Core	Date (June 2000)	Time (local)	Depth (mbsf) Top	Depth (mbsf) Bottom	Length (m) Cored	Length (m) Recovered	Recovery (%)	Comments
190-1176A-								
1H	26	1330	0.0	7.4	7.4	7.41	100.1	
2H	26	1440	7.4	16.9	9.5	9.09	95.7	
3H	26	1525	16.9	26.4	9.5	9.17	96.5	Start tensor at 14:30
4H	26	1645	26.4	35.9	9.5	9.46	99.6	
5H	26	1725	35.9	45.4	9.5	7.12	74.9	
6H	26	1815	45.4	54.9	9.5	8.39	88.3	
7H	26	1900	54.9	64.4	9.5	9.52	100.2	
8H	26	2000	64.4	73.9	9.5	2.51	26.4	
9H	26	2100	73.9	83.4	9.5	10.11	106.4	
10H	26	2155	83.4	92.9	9.5	7.54	79.4	Start tensor at 21:50
11H	26	2255	92.9	102.4	9.5	9.72	102.3	
12H	26	2345	102.4	111.9	9.5	9.08	95.6	Disturbed
13H	27	0105	111.9	115.3	3.4	3.43	100.9	
140	27	0145	115.3	121.4	0.0	0.00	NA	Drilled without coring
14H	27	0215	121.4	130.9	9.5	9.88	104.0	
15H	27	0310	130.9	140.4	9.5	9.02	94.9	
16H	27	0405	140.4	149.9	9.5	9.42	99.2	
17H	27	0455	149.9	159.4	9.5	9.32	98.1	DVTP at 3191.5 m, camera out at 04:55
18H	27	0735	159.4	162.4	3.0	3.04	101.3	Camera in at 06:30
19H	27	0850	162.4	170.6	8.2	8.20	100.0	Camera out at 08:50
20X	27	1030	170.6	180.2	9.6	1.86	19.4	
21X	27	1125	180.2	189.9	9.7	9.33	96.2	
22X	27	1230	189.9	199.5	9.6	9.86	102.7	
23X	27	1345	199.5	209.1	9.6	4.77	49.7	
24X	27	1500	209.1	218.7	9.6	9.83	102.4	DVTP at 218.7 mbsf
25X	27	1735	218.7	228.3	9.6	6.13	63.9	
26X	27	1850	228.3	237.9	9.6	8.75	91.1	
27X	27	2000	237.9	247.5	9.6	4.58	47.7	DVTP at 3279.6 m
28X	27	2240	247.5	257.1	9.6	1.43	14.9	
29X	27	2345	257.1	266.7	9.6	0.35	3.6	
30X	28	0035	266.7	276.4	9.7	0.51	5.3	
31X	28	0130	276.4	286.1	9.7	0.29	3.0	
32X	28	0245	286.1	295.7	9.6	0.28	2.9	
33X	28	0340	295.7	305.3	9.6	1.21	12.6	DVTP at 3337.4 m
34X	28	0635	305.3	314.9	9.6	0.30	3.1	
35X	28	0735	314.9	324.5	9.6	0.77	8.0	WSTP at 3356.6 m
36X	28	1025	324.5	334.1	9.6	1.61	16.8	
37X	28	1120	334.1	343.7	9.6	1.21	12.6	
38X	28	1220	343.7	353.4	9.7	0.38	3.9	
39X	28	1330	353.4	363.0	9.6	1.12	11.7	
40X	28	1510	363.0	372.7	9.7	2.02	20.8	
41X	28	1645	372.7	382.4	9.7	0.58	6.0	DVTP at 382.4 mbsf
42X	28	1910	382.4	392.0	9.6	0.50	5.2	
43X	28	2030	392.0	401.6	9.6	4.61	48.0	
44X	28	2200	401.6	411.2	9.6	1.17	12.2	
45X	28	2340	411.2	420.8	9.6	0.45	4.7	
46X	29	0105	420.8	430.3	9.5	0.29	3.1	
47X	29	0250	430.3	440.0	9.7	0.27	2.8	
48X	29	0435	440.0	449.6	9.6	0.36	3.8	
				Totals:	443.5	226.25	51.0	

Notes: DVTP = Davis-Villinger temperature probe, WSTP = water-sampling temperature probe. NA = not applicable.

Table T2. Coring summary by section, Site 1176. (**See table notes.** Continued on next four pages.)

Core	Date (June 2000)	Time (local)	Core depth (mbsf) Top	Core depth (mbsf) Bottom	Length (m) Cored	Length (m) Recovered	Recovery (%)	Section	Length (m) Liner	Length (m) Curated	Section depth (mbsf) Top	Section depth (mbsf) Bottom	Catwalk samples
190-1176A-													
1H	26	1330	0.0	7.4	7.4	7.41	100.1						
								1	1.5	1.5	0.0	1.5	IW, WRY, WRY, WRS
								2	1.5	1.5	1.5	3.0	IW
								3	1.5	1.5	3.0	4.5	IW, BGAS
								4	1.5	1.5	4.5	6.0	IW, HS, BGAS, BACT
								5	0.95	0.95	6.0	6.95	IW
								6	0.25	0.25	6.95	7.2	
								CC(w/6)	0.21	0.21	7.2	7.41	PAL
								Totals:	7.41	7.41			
2H	26	1440	7.4	16.9	9.5	9.09	95.7						
								1	1.5	1.5	7.4	8.9	IW
								2	1.5	1.5	8.9	10.4	IW, BGAS
								3	1.5	1.5	10.4	11.9	BACT, IW
								4	1.5	1.5	11.9	13.4	IW, HS, BGAS
								5	1.5	1.5	13.4	14.9	IW
								6	1.0	1.0	14.9	15.9	IW
								7	0.41	0.41	15.9	16.31	
								CC(w/7)	0.18	0.18	16.31	16.49	PAL
								Totals:	9.09	9.09			
3H	26	1525	16.9	26.4	9.5	9.17	96.5						
								1	1.5	1.5	16.9	18.4	
								2	1.5	1.5	18.4	19.9	BACT, IW
								3	1.5	1.5	19.9	21.4	BGAS
								4	1.5	1.5	21.4	22.9	HS, BGAS, IW
								5	1.5	1.5	22.9	24.4	
								6	1.01	1.01	24.4	25.41	IW
								7	0.43	0.43	25.41	25.84	
								CC(w/7)	0.23	0.23	25.84	26.07	PAL
								Totals:	9.17	9.17			
4H	26	1645	26.4	35.9	9.5	9.46	99.6						
								1	1.5	1.5	26.4	27.9	
								2	1.5	1.5	27.9	29.4	BACT, IW, BGAS
								3	1.5	1.5	29.4	30.9	
								4	1.5	1.5	30.9	32.4	
								5	1.5	1.5	32.4	33.9	HS, BGAS, IW
								6	1.0	1.0	33.9	34.9	
								7	0.72	0.72	34.9	35.62	
								CC(w/7)	0.24	0.24	35.62	35.86	PAL
								Totals:	9.46	9.46			
5H	26	1725	35.9	45.4	9.5	7.12	74.9						
								1	1.5	1.5	35.9	37.4	BACT, IW
								2	1.5	1.5	37.4	38.9	
								3	1.5	1.5	38.9	40.4	
								4	1.5	1.5	40.4	41.9	
								5	0.89	0.89	41.9	42.79	HS, IW
								CC(w/5)	0.23	0.23	42.79	43.02	PAL
								Totals:	7.12	7.12			
6H	26	1815	45.4	54.9	9.5	8.39	88.3						
								1	1.5	1.5	45.4	46.9	
								2	1.5	1.5	46.9	48.4	HS
								3	1.5	1.5	48.4	49.9	
								4	1.5	1.5	49.9	51.4	WRY, WRS, BACT, BG
								5	1.5	1.5	51.4	52.9	
								6	0.71	0.71	52.9	53.61	
								CC(w/6)	0.18	0.18	53.61	53.79	PAL
								Totals:	8.39	8.39			
7H	26	1900	54.9	64.4	9.5	9.52	100.2						
								1	1.5	1.5	54.9	56.4	
								2	1.5	1.5	56.4	57.9	
								3	1.5	1.5	57.9	59.4	
								4	1.5	1.5	59.4	60.9	BACT, IW
								5	1.5	1.5	60.9	62.4	HS
								6	1.5	1.5	62.4	63.9	
								7	0.35	0.35	63.9	64.25	
								CC(w/7)	0.17	0.17	64.25	64.42	PAL
								Totals:	9.52	9.52			
8H	26	2000	64.4	73.9	9.5	2.51	26.4						

Table T2 (continued).

Core	Date (June 2000)	Time (local)	Core depth (mbsf) Top	Core depth (mbsf) Bottom	Length (m) Cored	Length (m) Recovered	Recovery (%)	Section	Length (m) Liner	Length (m) Curated	Section depth (mbsf) Top	Section depth (mbsf) Bottom	Catwalk samples
								1	1.5	1.5	64.4	65.9	HS
								2	0.91	0.91	65.9	66.81	
								CC(w/2)	0.1	0.1	66.81	66.91	BGAS, PAL
								Totals:	2.51	2.51			
9H	26	2100	73.9	83.4	9.5	10.11	106.4						
								1	1.5	1.5	73.9	75.4	
								2	1.5	1.5	75.4	76.9	
								3	1.5	1.5	76.9	78.4	BACT, IW
								4	1.5	1.5	78.4	79.9	HS
								5	1.5	1.5	79.9	81.4	
								6	1.5	1.5	81.4	82.9	
								7	0.82	0.82	82.9	83.72	
								CC(w/7)	0.29	0.29	83.72	84.01	PAL
								Totals:	10.11	10.11			
10H	26	2155	83.4	92.9	9.5	7.54	79.4						
								1	1.5	1.5	83.4	84.9	
								2	1.5	1.5	84.9	86.4	IW
								3	1.5	1.5	86.4	87.9	
								4	1.5	1.5	87.9	89.4	
								5	0.68	0.68	89.4	90.08	HS
								6	0.57	0.57	90.08	90.65	
								CC(w/6)	0.29	0.29	90.65	90.94	PAL, BGAS
								Totals:	7.54	7.54			
11H	26	2255	92.9	102.4	9.5	9.72	102.3						
								1	1.5	1.5	92.9	94.4	
								2	1.5	1.5	94.4	95.9	
								3	1.5	1.5	95.9	97.4	HS
								4	1.5	1.5	97.4	98.9	BGAS, IW, WRY, WRS
								5	1.5	1.5	98.9	100.4	
								6	1.5	1.5	100.4	101.9	
								7	0.51	0.51	101.9	102.41	
								CC(w/7)	0.21	0.21	102.41	102.62	PAL
								Totals:	9.72	9.72			
12H	26	2345	102.4	111.9	9.5	9.08	95.6						
								1	1.4	1.4	102.4	103.8	
								2	0.67	0.67	103.8	104.47	Disturbed
								3	1.5	1.5	104.47	105.97	
								4	1.45	1.45	105.97	107.42	IW
								5	1.32	1.32	107.42	108.74	HS, BGAS
								6	1.5	1.5	108.74	110.24	
								7	0.32	0.32	110.24	110.56	
								CC(w/CC)	0.92	0.92	110.56	111.48	PAL
								Totals:	9.08	9.08			
13H	27	0105	111.9	115.3	3.4	3.43	100.9						
								1	1.5	1.5	111.9	113.4	IW
								2	1.38	1.38	113.4	114.78	HS
								3	0.44	0.44	114.78	115.22	
								CC(w/3)	0.11	0.11	115.22	115.33	PAL
								Totals:	3.43	3.43			
NA	27	0145	115.3	121.4	NA	NA		**** Drilled without coring ****					
14H	27	0215	121.4	130.9	9.5	9.88	104						
								1	1.5	1.5	121.4	122.9	
								2	1.5	1.5	122.9	124.4	
								3	1.5	1.5	124.4	125.9	
								4	1.5	1.5	125.9	127.4	BACT, IW
								5	1.5	1.5	127.4	128.9	HS, BGAS
								6	1.5	1.5	128.9	130.4	
								7	0.57	0.57	130.4	130.97	
								CC(w/7)	0.31	0.31	130.97	131.28	PAL
								Totals:	9.88	9.88			
15H	27	0310	130.9	140.4	9.5	9.02	94.9						
								1	1.5	1.5	130.9	132.4	
								2	1.5	1.5	132.4	133.9	
								3	1.5	1.5	133.9	135.4	IW
								4	1.5	1.5	135.4	136.9	HS
								5	1.5	1.5	136.9	138.4	
								6	1.5	1.5	138.4	139.9	

Table T2 (continued).

Core	Date (June 2000)	Time (local)	Core depth (mbsf) Top	Core depth (mbsf) Bottom	Length (m) Cored	Length (m) Recovered	Recovery (%)	Section	Length (m) Liner	Length (m) Curated	Section depth (mbsf) Top	Section depth (mbsf) Bottom	Catwalk samples
								CC(NS)	0.02	0.02	139.9	139.92	All to PAL
								Totals:	9.02	9.02			
16H	27	0405	140.4	149.9	9.5	9.42	99.2						
								1	1.5	1.5	140.4	141.9	
								2	1.5	1.5	141.9	143.4	
								3	1.5	1.5	143.4	144.9	
								4	1.5	1.5	144.9	146.4	HS, BGAS
								5	1.5	1.5	146.4	147.9	IW
								6	1.5	1.5	147.9	149.4	
								CC(w/CC)	0.42	0.42	149.4	149.82	PAL
								Totals:	9.42	9.42			
17H	27	0455	149.9	159.4	9.5	9.32	98.1						
								1	1.5	1.5	149.9	151.4	
								2	1.5	1.5	151.4	152.9	
								3	1.5	1.5	152.9	154.4	
								4	1.5	1.5	154.4	155.9	IW
								5	1.5	1.5	155.9	157.4	HS
								6	1.5	1.5	157.4	158.9	
								CC(w/CC)	0.32	0.32	158.9	159.22	PAL
								Totals:	9.32	9.32			
18H	27	0735	159.4	162.4	3.0	3.04	101.3						
								1	1.37	1.37	159.4	160.77	
								2	1.5	1.5	160.77	162.27	HS, BGAS
								CC(w/CC)	0.17	0.17	162.27	162.44	PAL
								Totals:	3.04	3.04			
19H	27	0850	162.4	170.6	8.2	8.20	100						
								1	1.5	1.5	162.4	163.9	
								2	1.5	1.5	163.9	165.4	
								3	1.5	1.5	165.4	166.9	IW
								4	1.5	1.5	166.9	168.4	HS, BGAS
								5	1.5	1.5	168.4	169.9	
								6	0.5	0.5	169.9	170.4	
								CC(w/CC)	0.2	0.2	170.4	170.6	PAL
								Totals:	8.2	8.2			
20X	27	1030	170.6	180.2	9.6	1.86	19.4						
								1	1.5	1.5	170.6	172.1	
								2	0.28	0.28	172.1	172.38	HS
								CC(w/2)	0.08	0.08	172.38	172.46	PAL
								Totals:	1.86	1.86			
21X	27	1125	180.2	189.9	9.7	9.33	96.2						
								1	1.5	1.5	180.2	181.7	
								2	1.5	1.5	181.7	183.2	HS, BGAS
								3	1.5	1.5	183.2	184.7	
								4	1.5	1.5	184.7	186.2	
								5	1.5	1.5	186.2	187.7	IW
								6	1.5	1.5	187.7	189.2	
								CC(w/CC)	0.33	0.33	189.2	189.53	PAL
								Totals:	9.33	9.33			
22X	27	1230	189.9	199.5	9.6	9.86	102.7						
								1	1.5	1.5	189.9	191.4	
								2	1.5	1.5	191.4	192.9	
								3	1.5	1.5	192.9	194.4	WRY, WRY, WRY, WRS
								4	1.5	1.5	194.4	195.9	
								5	1.5	1.5	195.9	197.4	HS
								6	1.5	1.5	197.4	198.9	
								7	0.48	0.48	198.9	199.38	
								CC(w/7)	0.38	0.38	199.38	199.76	BACT, PAL
								Totals:	9.86	9.86			
23X	27	1345	199.5	209.1	9.6	4.77	49.7						
								1	1.5	1.5	199.5	201.0	
								2	1.5	1.5	201.0	202.5	IW
								3	1.39	1.39	202.5	203.89	HS, BGAS
								CC(w/CC)	0.38	0.38	203.89	204.27	PAL
								Totals:	4.77	4.77			
24X	27	1500	209.1	218.7	9.6	9.83	102.4						
								1	1.5	1.5	209.1	210.6	
								2	1.5	1.5	210.6	212.1	
								3	1.5	1.5	212.1	213.6	

Table T2 (continued).

Core	Date (June 2000)	Time (local)	Core depth (mbsf) Top	Core depth (mbsf) Bottom	Length (m) Cored	Length (m) Recovered	Recovery (%)	Section	Length (m) Liner	Length (m) Curated	Section depth (mbsf) Top	Section depth (mbsf) Bottom	Catwalk samples
								4	1.5	1.5	213.6	215.1	IW
								5	1.5	1.5	215.1	216.6	HS, BGAS
								6	1.5	1.5	216.6	218.1	
								7	0.44	0.44	218.1	218.54	
								CC(w/7)	0.39	0.39	218.54	218.93	PAL
								Totals:	9.83	9.83			
25X	27	1735	218.7	228.3	9.6	6.13	63.9						
								1	1.5	1.5	218.7	220.2	
								2	1.5	1.5	220.2	221.7	IW
								3	1.5	1.5	221.7	223.2	HS
								4	1.22	1.22	223.2	224.42	
								CC(w/CC)	0.41	0.41	224.42	224.83	PAL
								Totals:	6.13	6.13			
26X	27	1850	228.3	237.9	9.6	8.75	91.1						
								1	1.5	1.5	228.3	229.8	
								2	1.5	1.5	229.8	231.3	BACT, BGAS, IW
								3	1.5	1.5	231.3	232.8	HS
								4	1.5	1.5	232.8	234.3	
								5	1.5	1.5	234.3	235.8	
								6	0.88	0.88	235.8	236.68	
								CC(w/6)	0.37	0.37	236.68	237.05	PAL
								Totals:	8.75	8.75			
27X	27	2000	237.9	247.5	9.6	4.58	47.7						
								1	1.5	1.5	237.9	239.4	IW
								2	1.5	1.5	239.4	240.9	HS
								3	1.2	1.2	240.9	242.1	
								CC(w/CC)	0.38	0.38	242.1	242.48	PAL
								Totals:	4.58	4.58			
28X	27	2240	247.5	257.1	9.6	1.43	14.9						
								1	1.2	1.2	247.5	248.7	HS
								CC(w/1)	0.23	0.23	248.7	248.93	PAL
								Totals:	1.43	1.43			
29X	27	2345	257.1	266.7	9.6	0.35	3.6						
								CC(w/CC)	0.35	0.35	257.1	257.45	PAL
								Totals:	0.35	0.35			
30X	28	0035	266.7	276.4	9.7	0.51	5.3						
								CC(w/CC)	0.51	0.51	266.7	267.21	PAL
								Totals:	0.51	0.51			
31X	28	0130	276.4	286.1	9.7	0.29	3						
								CC(w/CC)	0.29	0.29	276.4	276.69	PAL, HS
								Totals:	0.29	0.29			
32X	28	0245	286.1	295.7	9.6	0.28	2.9						
								CC(w/CC)	0.28	0.28	286.1	286.38	PAL
								Totals:	0.28	0.28			
33X	28	0340	295.7	305.3	9.6	1.21	12.6						
								1	0.79	0.79	295.7	296.49	HS
								CC(w/1)	0.42	0.42	296.49	296.91	PAL
								Totals:	1.21	1.21			
34X	28	0635	305.3	314.9	9.6	0.30	3.1						
								CC(w/CC)	0.3	0.3	305.3	305.6	PAL
								Totals:	0.3	0.3			
35X	28	0735	314.9	324.5	9.6	0.77	8						
								1	0.43	0.43	314.9	315.33	
								CC(w/1)	0.34	0.34	315.33	315.67	PAL
								Totals:	0.77	0.77			
36X	28	1025	324.5	334.1	9.6	1.61	16.8						
								1	0.43	0.43	324.5	324.93	HS, BGAS, IW
								2	0.84	0.84	324.93	325.77	IW
								CC(w/2)	0.34	0.34	325.77	326.11	PAL
								Totals:	1.61	1.61			
37X	28	1120	334.1	343.7	9.6	1.21	12.6						
								1	0.61	0.61	334.1	334.71	HS, BGAS, IW
								2	0.29	0.29	334.71	335.0	
								CC(w/2)	0.31	0.31	335.0	335.31	PAL
								Totals:	1.21	1.21			
38X	28	1220	343.7	353.4	9.7	0.38	3.9						
								CC(w/CC)	0.38	0.38	343.7	344.08	PAL, BACT
								Totals:	0.38	0.38			

Table T2 (continued).

Core	Date (June 2000)	Time (local)	Core depth (mbsf) Top	Core depth (mbsf) Bottom	Length (m) Cored	Length (m) Recovered	Recovery (%)	Section	Length (m) Liner	Length (m) Curated	Section depth (mbsf) Top	Section depth (mbsf) Bottom	Catwalk samples
39X	28	1330	353.4	363.0	9.6	1.12	11.7						
								1	0.45	0.45	353.4	353.85	IW
								2	0.23	0.23	353.85	354.08	HS, BGAS
								CC(w/2)	0.44	0.44	354.08	354.52	PAL
								Totals:	1.12	1.12			
40X	28	1510	363.0	372.7	9.7	2.02	20.8						
								1	0.75	0.75	363.0	363.75	IW, BACT
								2	0.91	0.91	363.75	364.66	HS
								CC(w/2)	0.36	0.36	364.66	365.02	PAL
								Totals:	2.02	2.02			
41X	28	1645	372.7	382.4	9.7	0.58	6						
								CC(w/CC)	0.58	0.58	372.7	373.28	PAL, HS
								Totals:	0.58	0.58			
42X	28	1910	382.4	392.0	9.6	0.50	5.2						
								CC(w/CC)	0.5	0.5	382.4	382.9	PAL
								Totals:	0.5	0.5			
43X	28	2030	392.0	401.6	9.6	4.61	48						
								1	1.5	1.5	392.0	393.5	IW, IW
								2	1.5	1.5	393.5	395.0	HS, BGAS, IW, IW
								3	1.12	1.12	395.0	396.12	
								CC(w/CC)	0.49	0.49	396.12	396.61	PAL
								Totals:	4.61	4.61			
44X	28	2200	401.6	411.2	9.6	1.17	12.2						
								1	0.79	0.79	401.6	402.39	BACT, HS
								CC(w/1)	0.38	0.38	402.39	402.77	PAL
								Totals:	1.17	1.17			
45X	28	2340	411.2	420.8	9.6	0.45	4.7						
								CC(w/CC)	0.45	0.45	411.2	411.65	PAL
								Totals:	0.45	0.45			
46X	29	0105	420.8	430.3	9.5	0.29	3.1						
								CC(w/CC)	0.29	0.29	420.8	421.09	PAL
								Totals:	0.29	0.29			
47X	29	0250	430.3	440.0	9.7	0.27	2.8						
								CC(w/CC)	0.27	0.27	430.3	430.57	PAL
								Totals:	0.27	0.27			
48X	29	0435	440.0	449.6	9.6	0.36	3.8						
								CC(w/CC)	0.36	0.36	440.0	440.36	PAL, IW
								Totals:	0.36	0.36			
			Totals:		443.5	226.25	51.0						

Notes: Catwalk samples: IW = interstitial water, HS = headspace, PAL = paleontology, VAC = vacutainer. All other abbreviations are sample codes for postcruise research (see the "**Sample Codes**" database query). NA = not applicable. CC = core catcher (number in parenthesis indicated which section the core catcher is stored with). This table is also available in **ASCII** format.

Table T3. Summary of stratigraphic relations at Site 1176 and correlation with Site 1175.

Unit	Facies name	Interval (cm) Top	Interval (cm) Bottom	Depth (mbsf)	Thickness (m)	Stratigraphic age	Lithologic description	Processes of formation	Correlation with Site 1175
I	Upper slope basin	1176A-1H-1, 0	1176A-22X-4, 139	000.00-195.79	195.79	Quaternary	Hemipelagic (nannofossil-rich) mud, volcanic ash, sand-to-silt turbidites, local soft-sediment folding and chaotic disruption	Hemipelagic settling, volcanic ash falls, turbidity currents, rare submarine slumps	Unit I
II	Middle slope basin	1176A-22X-4, 139	1176A-25X-4, 34	195.79-223.54	27.75	Quaternary	Hemipelagic mud, sandy mudstone, rare volcanic ash	Hemipelagic settling, muddy debris flows, volcanic ash falls	Unit II
III	Slope to prism transition	1176A-25X-4, 34	1176A-48X-CC, 36	223.54-440.36	216.82	Quaternary to Pliocene	Hemipelagic mudstone, pebbly mudstone, gravel, abundant sand-to-silt turbidites, rare volcanic ash	Debris flows, frequent turbidity currents, hemipelagic settling, volcanic ash falls	Unit III

Table T4. Peak intensities and peak areas from X-ray diffraction analysis of bulk-powder sediment samples, Hole 1176A. (Continued on next page.)

Core, section, interval (cm)	Depth (mbsf)	X-ray diffraction peak intensity (cps)								X-ray diffraction peak area (total counts)							
		Smectite + chlorite	Illite	Chlorite + kaolinite	(101) Quartz	Plagioclase	Calcite	(100) Quartz	(101) Cristobalite	Smectite + chlorite	Illite	Chlorite + kaolinite	(101) Quartz	Plagioclase	Calcite	(100) Quartz	(101) Cristobalite
190-1176A-																	
1H-2, 135-136	2.85	58	183	142	1,970	352	638	330	126	2,246	2,791	2,377	25,968	10,107	8,537	4,249	1,453
1H-3, 137-138	4.37	51	103	126	1,855	346	436	314	102	1,636	2,309	2,031	24,919	9,120	5,672	4,049	1,318
1H-4, 137-138	5.87	53	100	122	1,877	601	474	282	91	1,847	2,160	2,169	24,830	11,155	6,147	3,878	1,086
2H-2, 136-137	10.26	58	125	137	2,186	398	451	339	99	2,291	2,775	2,425	28,339	9,201	6,236	4,441	1,314
2H-4, 137-138	13.27	53	112	124	1,586	302	536	297	85	2,214	2,447	2,073	21,229	8,236	7,419	3,991	1,014
2H-6, 87-88	15.77	46	87	96	1,540	309	693	258	87	2,156	1,852	1,608	20,188	7,786	9,160	3,386	1,188
3H-2, 137-138	19.77	43	81	93	1,484	299	1,028	258	85	1,746	1,833	1,876	19,290	7,935	13,871	3,252	1,287
3H-4, 138-139	22.78	46	85	89	1,596	297	845	337	77	2,222	2,027	1,755	20,766	7,172	11,197	4,261	1,054
3H-6, 89-90	25.29	49	90	98	1,672	291	509	247	82	1,566	1,800	1,826	21,846	8,771	7,214	3,384	1,166
4H-2, 140-141	29.30	60	102	113	1,868	326	439	308	91	1,745	2,840	2,070	23,910	8,499	6,246	3,798	1,121
4H-3, 66-67	30.06	56	101	126	1,963	316	385	338	96	2,150	2,532	2,359	25,899	8,586	5,459	4,521	1,282
4H-5, 138-139	33.78	43	98	102	1,720	284	797	270	90	1,487	1,911	1,900	22,678	7,854	10,599	3,460	1,189
5H-5, 71-72	42.61	39	82	88	1,672	274	811	237	114	1,798	1,950	1,815	21,182	7,593	10,840	3,178	1,571
6H-4, 107-108	50.97	45	122	123	1,687	372	491	296	91	2,157	2,706	2,469	22,950	8,598	7,059	3,637	1,222
7H-4, 128-129	60.68	59	115	112	1,792	321	847	285	69	2,161	2,446	2,065	22,962	8,621	10,686	3,702	932
7H-6, 9-10	62.49	34	32	36	465	564	93	175	64	1,495	690	637	6,297	9,424	1,436	2,017	1,280
8H-1, 68-69	65.08	53	104	104	1,731	270	985	262	84	2,186	2,364	2,155	22,230	7,200	12,476	3,167	1,033
9H-3, 130-131	78.20	33	76	73	1,353	556	1,268	222	70	1,815	1,779	1,359	17,694	9,360	16,118	2,943	979
9H-6, 69-70	82.09	36	66	65	1,066	217	1,451	184	63	1,269	1,266	1,201	13,729	5,548	18,714	2,347	808
10H-2, 79-80	85.69	43	85	87	1,578	245	1,294	266	73	1,990	1,953	1,656	20,196	6,509	16,895	3,262	1,030
10H-3, 131-132	87.71	46	82	82	1,434	566	1,064	257	107	1,746	1,619	1,584	18,706	10,668	13,674	3,438	1,377
11H-4, 105-106	98.45	51	94	100	1,488	286	852	287	106	2,015	2,161	1,704	19,774	7,099	11,264	3,615	1,198
12H-4, 129-130	107.26	48	144	141	1,748	314	602	294	89	2,242	3,069	2,449	23,457	8,018	8,179	4,069	1,175
13H-1, 126-127	113.16	56	111	109	1,818	395	588	278	113	2,071	2,613	1,890	23,880	8,841	7,792	3,636	1,543
14H-2, 80-81	123.70	46	98	97	1,716	355	1,103	269	80	1,875	2,378	1,704	22,577	8,240	14,226	3,748	1,082
14H-4, 131-132	127.21	53	99	106	1,764	299	929	335	75	2,028	2,076	2,052	23,461	7,560	12,089	4,235	916
15H-3, 129-130	135.19	54	111	113	1,660	346	652	296	90	2,292	2,175	2,256	22,557	8,660	8,917	3,902	1,192
16H-5, 129-130	147.69	57	103	116	1,546	389	950	270	64	2,051	2,428	2,080	20,644	8,946	12,299	3,544	853
17H-4, 132-133	155.72	33	69	69	1,367	235	1,120	216	87	1,809	1,416	1,454	18,410	6,506	14,597	3,056	1,425
18H-1, 135-136	160.75	32	49	42	755	138	658	132	53	1,687	1,052	1,057	10,202	4,498	8,720	1,924	1,000
19H-3, 128-129	166.68	42	94	90	1,368	247	967	230	71	1,586	2,038	1,534	18,041	6,778	12,509	3,098	915
19H-5, 76-77	169.16	52	115	115	1,694	350	647	267	76	2,085	2,511	2,168	22,253	9,608	8,688	3,429	1,073
20X-1, 42-43	171.02	56	115	111	1,547	296	719	265	78	2,517	2,593	2,223	20,178	8,425	9,709	3,379	1,015
21X-5, 121-122	187.41	64	148	140	2,008	347	561	308	88	2,202	3,399	2,871	26,618	9,877	7,762	4,136	1,081
22X-3, 104-105	193.94	54	93	95	1,531	251	854	277	82	2,811	1,941	1,843	21,288	7,128	11,956	3,742	1,087
23X-3, 58-59	203.08	64	121	120	2,173	324	622	264	83	2,627	2,698	2,116	27,010	10,528	8,428	3,313	1,232
24X-3, 88-89	212.98	66	123	122	1,771	308	584	319	85	2,902	2,559	2,417	23,521	8,374	7,952	4,325	1,285
24X-6, 60-61	217.20	51	63	70	1,308	281	1,287	239	71	3,029	1,656	1,275	16,883	7,022	16,257	3,335	856
25X-2, 121-122	221.41	56	95	109	1,673	297	695	309	101	2,638	2,004	1,866	22,169	8,312	9,260	4,052	1,233
25X-4, 70-71	223.90	51	122	94	2,532	568	349	622	82	2,384	2,383	2,065	33,540	13,112	4,244	7,576	1,193
26X-2, 119-120	230.99	71	123	120	2,635	467	322	426	103	3,001	2,254	2,265	34,448	13,377	4,273	5,600	1,316
27X-1, 119-120	239.09	81	180	185	3,007	1,144	96	624	97	3,033	3,247	3,520	40,346	22,962	1,200	7,771	1,435
29X-CC, 26-27	257.36	66	119	149	2,595	1,169	125	404	112	2,873	2,378	2,747	33,753	22,747	1,679	5,341	1,478
33X-CC, 17-18	296.66	85	161	169	3,024	558	0	413	108	3,024	3,470	3,045	38,036	14,796	0	5,513	1,460
34X-CC, 22-23	305.52	39	54	79	5,170	669	0	781	87	1,660	1,251	1,906	60,625	14,750	0	9,227	1,056
35X-1, 29-30	315.19	53	88	78	3,485	440	90	603	87	2,442	1,530	1,610	42,914	12,282	2,556	7,624	1,028

Table T4 (continued). .

Core, section, interval (cm)	Depth (mbsf)	X-ray diffraction peak intensity (cps)								X-ray diffraction peak area (total counts)							
		Smectite + chlorite	Illite	Chlorite + kaolinite	(101) Quartz	Plagioclase	Calcite	(100) Quartz	(101) Cristobalite	Smectite + chlorite	Illite	Chlorite + kaolinite	(101) Quartz	Plagioclase	Calcite	(100) Quartz	(101) Cristobalite
36X-1, 29-30	324.79	65	138	130	4,165	965	50	574	109	2,389	2,467	2,244	50,914	19,178	692	7,095	1,222
36X-2, 69-70	325.62	68	122	137	4,161	600	77	660	106	2,496	2,054	2,498	52,960	15,959	764	8,297	1,155
37X-1, 39-40	334.49	67	113	100	3,682	646	61	560	98	2,407	2,389	2,004	45,288	17,872	1,246	6,446	1,089
39X-1-23, 24	353.63	78	170	174	3,337	1,157	39	614	142	2,287	2,790	2,830	43,296	23,191	662	7,257	1,578
40X-1-50, 51	363.50	54	113	129	4,210	1,249	56	813	106	2,119	2,058	2,082	52,783	24,777	887	10,087	1,107
41X-CC, 12-13	372.82	67	116	120	2,514	341	93	360	105	2,787	2,246	2,335	31,959	10,608	1,433	4,746	1,343
43X-1, 120-121	393.20	52	90	86	2,570	513	21	389	59	1,764	1,745	1,545	31,198	13,533	168	4,722	733
43X-2, 129-130	394.79	79	136	171	2,700	740	0	587	175	3,419	2,636	3,120	35,757	19,734	0	7,542	2,597
43X-2, 58-59	394.08	47	65	79	1,041	165	816	175	55	2,515	2,060	1,651	13,674	4,333	17,977	2,551	725
44X-CC, 2-3	402.41	64	127	123	3,182	788	19	491	83	2,883	2,470	2,161	40,816	17,861	208	6,373	989

Table T5. Normalized relative mineral abundances based on X-ray diffraction analysis of random bulk-sediment powders, Hole 1176A.

Unit	Core, section, interval (cm)	Depth (mbsf)	Normalized relative mineral abundance (wt%)				Peak area ratio: (101) Cristobalite/ (100) Quartz
			Total clay minerals	Quartz	Plagioclase	Calcite	
	190-1176A-						
	1H-3, 137-138	4.37	41	33	14	13	0.33
	1H-4, 137-138	5.87	39	32	16	13	0.28
	2H-2, 136-137	10.26	44	33	12	12	0.30
	2H-4, 137-138	13.27	44	28	12	17	0.25
	2H-6, 87-88	15.77	38	29	11	22	0.35
	3H-2, 137-138	19.77	33	24	11	32	0.40
	3H-4, 138-139	22.78	38	27	10	25	0.25
	3H-6, 89-90	25.29	36	31	14	18	0.34
	4H-2, 140-141	29.30	45	29	12	14	0.30
	4H-3, 66-67	30.06	44	33	12	11	0.28
	4H-5, 138-139	33.78	34	29	12	26	0.34
	5H-5, 71-72	42.61	36	28	11	26	0.49
	6H-4, 107-108	50.97	45	28	12	15	0.34
	7H-4, 128-129	60.68	39	27	11	23	0.25
	7H-6, 9-10	62.49	40	24	31	5	0.63
	8H-1, 68-69	65.08	38	26	9	26	0.33
I	9H-3, 130-131	78.20	31	22	12	35	0.33
	9H-6, 69-70	82.09	25	19	9	47	0.34
	10H-2, 79-80	85.69	33	24	8	35	0.32
	10H-3, 131-132	87.71	30	24	15	31	0.40
	11H-4, 105-106	98.45	38	26	10	26	0.33
	12H-4, 129-130	107.26	46	27	10	17	0.29
	13H-1, 126-127	113.16	42	29	12	17	0.42
	14H-2, 80-81	123.70	35	25	10	29	0.29
	14H-4, 131-132	127.21	36	28	10	26	0.22
	15H-3, 129-130	135.19	40	29	12	20	0.31
	16H-5, 129-130	147.69	38	24	12	26	0.24
	17H-4, 132-133	155.72	30	25	10	35	0.47
	18H-1, 135-136	160.75	36	23	10	31	0.52
	19H-3, 128-129	166.68	36	24	10	31	0.30
	19H-5, 76-77	169.16	41	27	13	19	0.31
	20X-1, 42-43	171.02	43	25	11	21	0.30
	21X-5, 121-122	187.41	46	28	12	14	0.26
	22X-3, 104-105	193.94	38	28	9	25	0.29
	Mean Unit I:		38	27	12	23	0.34
	23X-3, 58-59	203.08	42	30	13	16	0.37
	24X-3, 88-89	212.98	44	29	11	16	0.30
II	24X-6, 60-61	217.20	35	23	8	33	0.26
	25X-2, 121-122	221.41	40	29	11	20	0.30
	Mean Unit II:		40	28	11	21	0.31
	25X-4, 70-71	223.90	39	38	16	7	0.16
	26X-2, 119-120	230.99	40	38	15	6	0.24
	27X-1, 119-120	239.09	41	36	23	0	0.18
	29X-CC, 26-27	257.36	38	36	26	0	0.28
	33X-CC, 17-18	296.66	47	37	16	0	0.26
	34X-CC, 22-23	305.52	25	59	16	0	0.11
	35X-1, 29-30	315.19	33	49	15	3	0.13
	36X-1, 29-30	324.79	35	46	19	0	0.17
III	36X-2, 69-70	325.62	33	50	17	0	0.14
	37X-1, 39-40	334.49	36	44	19	0	0.17
	39X-1, 23-24	353.63	36	39	25	0	0.22
	40X-1, 50-51	363.50	29	46	25	0	0.11
	41X-CC, 12-13	372.82	44	41	14	0	0.28
	43X-1, 120-121	393.20	36	43	21	0	0.16
	43X-2, 129-130	394.79	42	37	22	0	0.34
	43X-2, 58-59	394.08	37	19	6	39	0.28
	44X-CC, 2-3	402.41	39	42	20	0	0.16
	Mean Unit III:		37	41	18	3	0.20

Table T6. Results of X-ray diffraction analysis of bulk-powder volcanic ash samples, Hole 1176A.

Core, section, interval (cm)	Depth (mbsf)	X-ray diffraction peak intensity (cps)												X-ray diffraction peak area (total counts)											
		Smectite	Illite	Chlorite	Clinoptilolite	Hornblende	Cristobalite	Quartz	Plagioclase	Calcite	Pyroxene	Halite	Pyrite	Smectite	Illite	Chlorite	Clinoptilolite	Hornblende	Cristobalite	Quartz	Plagioclase	Calcite	Pyroxene	Halite	Pyrite
190-1176A-																									
13H-3, 12-13	114.91	22	0	0	0	0	72	148	94	55	53	154	0	1,450	0	0	0	0	1,300	1,852	2,700	857	761	2,259	0
17H-3, 52-53	153.43	0	33	14	0	33	0	392	1,403	65	133	112	0	0	736	251	0	286	0	5,059	23,803	926	2,391	2,330	0
18H-2, 68-69	161.46	19	284	0	0	0	31	159	54	32	0	461	0	1,172	2,283	0	0	0	358	2,079	971	426	0	5,845	0
25X-CC, 31-32	224.74	0	41	23	0	0	27	336	57	26	0	94	0	0	639	254	0	0	617	4,477	1,470	593	0	1,509	0

Table T7. Structural data, Hole 1176A. (See table note. Continued on next page.)

Core, section, interval (cm)	Depth (mbsf)	Cr az. (°)	Cr dip (°)	Pm az.	Pm plunge	Identifier	Notes
190-1176A-							
1H-4, 117-123	5.67	209	44			Bed	
2H	7.4	0	0			Bed	
3H	16.9	0	0	228.76	0	Bed	
4H	26.4	0	0	49.79	0	Bed	
5H	35.9	0	0	247.26	0	Bed	
6H-3, 86-87	49.26	0	10	80.82	10	Bed	
7H-3, 32-37	58.22	0	55	35.22	55	Bed	Slump layer?
7H-3, 41-48	58.31	180	90	215.22	90	Bed	Slump layer?
7H-4, 95-99	60.35	116	58	151.22	58	Bed	Slump layer?
7H-6, 130-134	63.7	244	9	279.22	9	Bed	
7H-6, 52-60	62.92	349	74	24.22	74	Fault	Possibly reverse, 1-cm displacement
8H	64.4	0	0	295.88	0	Bed	
9H	73.9	0	0	290.01	0	Bed	
10H-6, 6-23	90.14	338	69	321.71	69	Bed	
11H-3, 134-138	97.24	13	29	95.98	29	Bed	
11H-6, 76-77	101.16	328	13	50.98	13	Bed	
12H-4, 52-61	106.49	315	61	98.38	61	Bed	
12H-4, 60-71	106.57	180	55	323.38	55	Bed	
12H-4, 60-71	106.57	180	60	323.38	60	Bed	
13H	111.9	0	0	52.63	0	Bed	
14H-6, 66-82	129.56	195	67	328.14	67	Fault or deformation band	
14H-1, 81-84	122.21	135	27	268.14	27	Bed	
14H-6, 141-151	130.31	180	66	313.14	66	Fault	
15H-2, 34-37	132.74	22	34	23.05	34	Bed	
15H-2, 97-101	133.37	15	35	16.05	35	Bed	
15H-4, 16-25	135.56	11	52	12.05	52	Bed	
15H-4, 61-70	136.01	9	56	10.05	56	Bed	
16H-1, 87-90	141.27	32	48	207.84	48	Bed	
16H-2, 73-75	142.63	230	53	45.84	53	Bed	
16H-4, 130-145	146.2	15	69	190.84	69	Fault or deformation band	
16H-6, 85-106	148.75	21	73	196.84	73	Fault or deformation band	
17H-2, 124-125	152.64	180	10	121.01	10	Bed	
18H	159.4	0	0	138.93	0	Bed	
19H-2, 48-49	164.38	302	9	186.14	9	Bed	
19H-3, 5-6	165.45	83	16	327.14	16	Bed	
19H-4, 35-38	167.25	18	29	262.14	29	Bed	
19H-5, 53-62	168.93	345	57	229.14	57	Bed	
19H-5, 97-100	169.37	312	27	196.14	27	Bed	
19H-6, 26-27	170.16	307	10	191.14	10	Bed	
20X	170.6					No structures	
21X	180.2	0	0			Bed	
22X	189.9	0	0			Bed	
23X-3, 9-10	202.59	55	25			Bed	
24X-5, 15-19	215.25	39	73			Normal fault	4-mm displacement
24X-6, 96-100	217.56	45	57			Normal fault	5-mm displacement
24X-6, 112-144	217.72					Breccia zone	
24X-6, 140-143	218	344	50			Fault	
25X-2, 24-29	220.44	328	86	134	86	Fault	
25X-2, 101-126	221.21					Breccia zone	
26X	228.3	0	0			Bed	
27X-2, 40-67	239.8					Breccia zone	
27X-2, 50-59	239.9	5	59	45	59	Fracture	
27X-2, 74-81	240.14	309	61	309	61	Fracture	
28X-1,CC	247.5	0	0			Bed	Evidence of horizontal bedding
29X-CC	257.1	0	0			Bed	Evidence of horizontal bedding
30X-CC	266.7	0	0			Bed	Evidence of horizontal bedding
31X-CC	276.4	0	0			Bed	Evidence of horizontal bedding
32X-CC	286.1	0	0			Bed	Evidence of horizontal bedding
33X-1, 55-72	296.25					Fracture	Few fractures probably of natural origin
33X-CC	296.49					Bed	Inclined beds?
34X-1							Highly disturbed
35X-1	314.9						Highly disturbed
35X-CC, 30-31	315.63	166	21			Fracture	Possible fault
35X-CC	315.33	0	0			Bed	Evidence of horizontal bedding
36X-1	324.5						Rubble

Table T7 (continued).

Core, section, interval (cm)	Depth (mbsf)	Cr az. (°)	Cr dip (°)	Pm az.	Pm plunge	Identifier	Notes
36X-2	324.93						Sands and gravels, no clear bedding
36X-CC	325.77						
37X-1.2.CC	334.1	0	0			Bed	Evidence of horizontal bedding
38X-CC	343.7	0	0			Bed	Evidence of horizontal bedding
39X	353.4						
39X	353.4					Fracture	Some fractured material
40X-1	363						Rubble
40X-2, 33-37	364.08	14	67	129	67	Fracture	Slightly developed slickensides
40X-2, 33-37	364.08	171	53	286	53	Fracture	Conjugate set preceding fracture
40X-2, 44-51	364.19	0	68	354	68	Fracture	Slightly developed slickensides
40X-2, 56-61	364.31	195	76	245	76	Fracture	Slightly developed slickensides
40X-2, 56-61	364.31	335	53	25	53	Fracture	Slightly developed slickensides
40X-2, 74-79	364.49	0	43	328	43	Fracture	Four parallel fractures
40X-2, 74-76	364.49	88	79	56	79	Fracture	Slightly developed slickensides
41X-CC, 14-55	372.84	0	0			Bed	Horizontal
42X		0	0			Bed	Very poor recovery
43X-1, 2, 3	392	0	0			Bed	Very poor recovery
43X-2, 15-20	393.65					Fracture	
44X	401.6	0	0			Bed	Very poor recovery
45X		0	0			Bed	Very poor recovery
46X		0	0			Bed	Very poor recovery
47X							Pebbly mudstone without sign of bedding
48X							Pebbly mudstone without sign of bedding

Note: Cr az. = azimuth of plane in core reference frame, Cr dip = dip of plane in core reference frame, Pm az. = azimuth of plane in paleomagnetic reference frame, Pm plunge = plunge of plane in paleomagnetic reference frame.

Table T8. Nannofossil events recognized, Site 1176.

Nannofossil zones	Datum events	Age (Ma)	Depth (mbsf)	Average sedimentation rate* (m/m.y.)
NN21b	FAD *Emiliania huxleyi* acme	0.085	11.94	170.5
	LAD *Helicosphaera inversa*	0.14	59.10	
NN21a	FAD *Emiliania huxleyi*	0.26	85.64	
NN20	LAD *Pseudoemiliania lacunosa*	0.46	89.11	
	LAD *Pseudoemiliania lacunosa*	0.46	109.10	
	LAD *Reticulofenestra asanoi*	0.8	200.64	
	FAD *Reticulofenestra asanoi*	1.06	238.59	
	FAD *Gephyrocapsa oceanica*	1.8	291.63	
NN19	LAD *Discoaster brouweri*	1.95	407.20	
NN16	LAD *Reticulofenestra pseudoumbilicus* (>7 µm)	3.8	425.82	

Notes: FAD = first appearance datum, LAD = last appearance datum. * = uncorrected for compaction.

Table T9. Interval and depth constraints of calcareous nannofossil events, Hole 1176A.

Event		Interval (cm)		Depth (mbsf)	
		Top	Bottom	Top	Bottom
		190-1176A-	190-1176A-		
B	*Emiliania huxleyi* acme	1H-CC	2H-CC	7.40	16.48
T	*Helicosphaera inversa*	6H-CC	8H-3, 89-90	53.78	64.41
B	*Emiliania huxleyi*	9H-CC	10H-CC	84.00	87.29
T	*Pseudoemiliania lacunosa*	10H-3, 89-90	10H-CC	87.29	90.93
T	*Pseudoemiliania lacunosa*	12H-4, 75-76	12H-CC	106.72	111.47
T	*Reticulofenestra asanoi*	22X-CC	23X-2, 53-54	199.75	201.53
B	*Reticulofenestra asanoi*	26X-CC	27X-2, 75-76	237.04	240.15
B	*Gephyrocapsa oceanica*	32X-CC	33X-CC	286.37	296.90
T	*Discoaster brouweri*	44X-CC	45X-CC	402.76	411.64
T	*Reticulofenestra pseudoumbilicus* (>7 µm)	46X-CC	47X-CC	421.08	430.56

Note: B = bottom occurrence, T = top occurrence.

Table T10. Calcareous nannofossil range chart, Site 1176. (See table notes. Continued on next page.)

Epoch	Zone	Core, section, interval (cm)	Depth (mbsf)	Preservation	Abundance	*Calcidiscus tropicus*	*Calcidiscus leptoporus*	*Calcidiscus macintyrei*	*Ceratolithus cristatus*	*Ceratolithus cristatus* var. *telesmus*	*Coccolithus pelagicus*	*Coccolithus pelagicus* (with bar)	*Cyclolithus annulus*	*Discoaster asymmetricus*	*Discoaster brouweri*	*Discoaster kugleri*	*Discoaster pentaradiatus*	*Discoaster* spp.	*Discoaster surculus*	*Discoaster triradiatus*	*Emiliania huxleyi*	*Florisphaera profunda*	*Gephyrocapsa muellerae*	*Gephyrocapsa oceanica*	*Gephyrocapsa* spp. (<2 µm)	*Helicosphaera carteri*	*Helicosphaera carteri* var. *walichii*	*Helicosphaera inversa*	*Helicosphaera sellii*	*Holodiscolithus macroporus*	*Oolithotus fragilis*	*Pontosphaera discopora*	*Pontosphaera japonica*	*Pontosphaera multipora*	*Pseudoemiliania lacunosa*	*Pseudoemiliania ovata*	*Reticulofenestra asanoi*	*Reticulofenestra haqii*	*Reticulofenestra minuta*	*Reticulofenestra minutula*	*Reticulofenestra pseudoumbilicus* (>7 µm)	*Reticulofenestra pseudoumbilicus* (5–7 µm)	*Reticulofenestra* spp.	*Rhabdosphaera clavigera*	*Rhabdosphaera clavigera* var. *stylifera*	*Scapholithus fossilis*	*Scyphosphaera* spp.	*Sphenolithus* spp.	*Syracosphaera pulchra*	*Syracosphaera* spp.	*Umbellosphaera tenuis*	*Umbilicosphaera hulburtiana*	*Umbilicosphaera rotula*	*Umbilicosphaera sibogae* var. *foliosa*	*Umbilicosphaera sibogae* var. *sibogae*
		190-1176A-																																																					
Pleistocene	NN21b	1H-CC		G	C		C					F									D	A	C	A	C	F	F									F				F				F	R				F	C	C			F	C
	NN21a	2H-CC		G	C		C		F			F									A	A	C	A	A	F									F								C	F		F					F	F		F	F
		3H-CC		G	C		F		R												C	A	C	C	D	F	R						F																F	F	F	F		F	F
		4H-CC		G	C		C				R	R	F					R			C	A	C	A	A	F	R			F						R									R				R	R	F			F	F
		5H-CC		M	C		C														C	A	C	C	D																		R						R	F				F	F
		6H-CC		G	C		C						F								C	A	A	C	A	R	R														R									F	R			F	F
		7H-CC		M	C		F		R		R										F	A	A	C	A	R	R	R						R	F								R											F	F
		8H-CC		G	F		F														F	C	A	C	D										F								F						C		F				
		9H-CC		G	C		C														F	A	A	A	A	F	R	R							F								F							R				F	F
	NN20	10H-3, 89-90	87.29	G	C		F		R		R	R										C	A	A	A	F							R	R										F					F	F				F	F
	NN19	10H-CC		G	C		F															A	D	C	A			R							F	C																			F
	NN20	11H-4, 78-79	98.18	G	C		F		R	R	R											A	D	C	A	R		R					R																						F
		11H-CC		G	C		F			R												A	A	C	A	R		R																					F		F				F
		12H-4, 75-76	106.72	G	C		F		R		F											A	A	A	D	R	R	F						R																					F
	NN19	12H-CC		G	C		R															C	D	A	A										F						F								R	F				R	R
		13H-CC		G	C		C															A	D	C	A			F																						F					F
		14H-CC		G	C																	C	D	C	A										F																				
		15H-CC		G	C																	C	D	C	A	F																												R	R
		16H-CC		G	C		F															C	D	C	A	F									C															F					F
		17H-CC		G	C		F															A	D	C	C										F	F					F										F				F
		18H-CC		M	F		C						F									C	D	C	A	F									F	C												F	F						F
		19H-CC		M	F		F															A	A	A	A	F										F							F								F			F	F
		20X-CC		G	F		C															A	C	C	D	F									F	C							F								F				
		21X-CC		G	C		C															A	A	A	A	F									C	C							F	F		F	F							F	F
		22X-CC		G	C		C											F				C	A	A	D	F		R							C	C									F	F		F	F	F				C	
		23X-2, 53-54	201.53	G	C		F				F	F										A	A	C	D	F									F	C	F												F						
		23X-CC		G	C		C				F											A	A	C	D	F	F							F	F	C	R																		
		24X-CC		G	C		C															A	C		D	R	R						F		C	C	C														R			F	F
		25X-CC		G	F		C				R	R	F									A	A	A	A	R	R		R			R			F	C	R				R		F											F	
		26X-CC		P	R																	C	A	A	A										C	C	F		C	C										C			F		
		27X-2, 75-76	240.15	P	F		R															A	C	F	D										C	F													R		R				
		27X-CC		P	R		C															A	C	F	A				R						C	C				A															
		28X-CC		P	R																		A	A	A															A															
		29X-CC		P	R		C					C						C				C			D										C	C	C			A								C							
		30X-CC		P	R						C											D	A												A					C															
		31X-CC		M	F		C	R														C	C	C	D	F			C						C	C				A	R								F						C

Table T10 (continued).

Epoch	Zone	Core, section, interval (cm)	Depth (mbsf)	Preservation	Abundance	*Calcidiscus tropicus*	*Calcidiscus leptoporus*	*Calcidiscus macintyrei*	*Ceratolithus cristatus*	*Ceratolithus cristatus* var. *telesmus*	*Coccolithus pelagicus*	*Coccolithus pelagicus* (with bar)	*Cyclolithus annulus*	*Discoaster asymmetricus*	*Discoaster brouweri*	*Discoaster kugleri*	*Discoaster pentaradiatus*	*Discoaster* spp.	*Discoaster surculus*	*Discoaster triradiatus*	*Emiliania huxleyi*	*Florisphaera profunda*	*Gephyrocapsa muellerae*	*Gephyrocapsa oceanica*	*Gephyrocapsa* spp. (<2 µm)	*Helicosphaera carteri*	*Helicosphaera carteri* var. *walichii*	*Helicosphaera inversa*	*Helicosphaera sellii*	*Holodiscolithus macroporus*	*Oolithotus fragilis*	*Pontosphaera discopora*	*Pontosphaera japonica*	*Pontosphaera multipora*	*Pseudoemiliania lacunosa*	*Pseudoemiliania ovata*	*Reticulofenestra asanoi*	*Reticulofenestra haqii*	*Reticulofenestra minuta*	*Reticulofenestra minutula*	*Reticulofenestra pseudoumbilicus* (>7 µm)	*Reticulofenestra pseudoumbilicus* (5–7 µm)	*Reticulofenestra* spp.	*Rhabdosphaera clavigera*	*Rhabdosphaera clavigera* var. *stylifera*	*Scapholithus fossilis*	*Scyphosphaera* spp.	*Sphenolithus* spp.	*Syracosphaera pulchra*	*Syracosphaera* spp.	*Umbellosphaera tenuis*	*Umbilicosphaera hulburtiana*	*Umbilicosphaera rotula*	*Umbilicosphaera sibogae* var. *foliosa*	*Umbilicosphaera sibogae* var. *sibogae*
Pleistocene		32X-CC		P	R																		A	C	D																								
		33X-CC		P	R		C														A	C	C		C										C													
		34X-CC		P	R																D	F	C												A	C												
		35X-CC		P	R		C														D	C		C	C										C	C		C	C									
		36X-CC		P	R	F	C	C													A			A						F				C	F			C										
		37X-CC		P	R			C													A			A	C									C				A										
	NN19	38X-CC		P	R			C			R										A	C		A	R			F		F		R	C	C			A										
		39X-CC		P	R																A			F										A	C			A										
		40X-CC		M	F		C	F			F		F								A	A		A		F								C	C			C										
		41X-CC		P	R																A			A										A				A										
Pliocene		42X-CC		P	R			R			F										A	C		D				R						C	C			A										
		43X-CC		P	R		C	C			F										A	C		A										C	C		A	A										
		44X-CC		P	T			A																										A														
		45X-CC		M	F							C			A						A	C		A									C				A	C										
	NN18-17	46X-CC		P	F	R	C	F			C	R			R	R			F	F			C		A	C										A	A	C										
		47X-CC		P	R									F			A							D												C	A	F										
	NN16?	48X-CC		M	F	C	C	C						F		F	C			F	D	C										C		C		F	C										

Notes: Abundance: D = dominant, A = abundant, C = common, F = few, R = rare. Preservation: P = poor, M = moderate, G = good. See **"Biostratigraphy,"** p. 9, in the "Explanatory Notes" chapter. This table is also available in **ASCII** format.

Table T11. Depths and ages of magnetic chrons and subchrons identified, Site 1176.

Depth (mbsf)					Age
Top	Bottom	Polarity	Chron	Subchron	(Ma)
0.00	199.55	N	Brunhes		0
46.70	50.65	R			
61.20	61.35	R			
64.50	66.35	R			
140.50	141.70	R			
159.45	161.47	R			
163.95	164.80	R			
181.75	182.15	R			
199.55	—	R	Matuyama		0.78
214.80	219.35	N		Jaramillo?	0.99

Notes: N = normal, R = reversed. — = not recovered.

Table T12. Pore fluid composition, Hole 1176A.

Hole, core, section, interval (cm)	Depth (mbsf)	pH (ISE)	Alk (T) (mM)	Sal (R)	Cl (T) (mM)	SO_4 (I) (mM)	Na (CB) (mM)	Mg (I) (mM)	Ca (I) (mM)	K (I) (mM)	H_4SiO_4 (S) (µM)	NH_4 (S) (mM)
190-1176A-												
1H-1, 140-150	1.40	7.67	6.0	34.0	549.0	25.9	482	47.9	8.72	11.4	737	0.45
1H-2, 140-150	2.90	7.63	9.7	34.0	552.0	22.2	485	47.0	7.84	11.1	687	
1H-3, 140-150	4.40	7.76	11.7	34.0	551.0	19.8	483	46.6	7.34	10.9	767	0.98
1H-4, 140-150	5.90	8.06	13.6	34.0	552.0	17.8	485	45.6	6.66	10.9	757	
1H-5, 85-95	6.85	8.07	15.1	34.0	552.0	16.4	485	45.3	6.18	10.8	705	1.33
2H-1, 140-150	8.80	7.75	20.1	33.0	552.0	9.6	483	43.6	4.55	10.6	722	
2H-2, 140-150	10.30	8.01	21.8	33.5	552.0	8.2	483	42.8	4.28	10.7	703	1.98
2H-3, 140-150	11.80	8.10	23.1	33.5	551.0	6.4	482	42.5	3.86	10.5	752	
2H-4, 140-150	13.30	7.80	24.2	33.0	551.0	5.0	482	42.1	3.26	10.6	744	2.08
2H-5, 140-150	14.80	8.06	25.1	33.0	552.0	3.7	483	40.8	3.37	11.2	754	
2H-6, 90-100	15.80	7.80	26.2	33.0	552.0	2.4	480	41.8	3.19	10.3	735	2.36
3H-2, 140-150	19.80	7.89	28.3	33.0	552.0	0.7	481	41.0	3.05	10.2	785	
3H-4, 140-150	22.80	8.07	29.2	33.0	552.5	0.0	480	41.4	3.03	9.8	837	2.59
3H-6, 91-101	25.31	8.14	29.0	33.0	552.0	0.0	478	41.8	3.26	9.6	718	
4H-2, 140-150	29.30	8.12	28.7	33.0	551.0	0.4	480	39.0	4.73	10.1	711	3.27
4H-5, 140-150	33.80	8.15	28.7	33.0	551.5	0.4	481	39.9	3.32	9.9	722	
5H-1, 135-150	37.25	7.80	28.8	33.0	551.0	0.0	482	39.4	3.11	9.8		3.14
5H-5, 74-89	42.64	7.82	27.6	33.0	551.0	0.0	481	39.0	3.17	9.7	770	
6H-4, 135-150	51.25	7.82	27.3	32.5	550.0	0.0	483	37.4	2.98	9.8	826	3.58
7H-4, 130-150	60.70	7.84	26.1	32.5	551.0	0.4	485	36.1	3.20	10.1	752	
9H-3, 135-150	78.25	7.88	25.0	32.5	550.0	0.0	484	35.2	3.20	10.1	757	
10H-2, 135-150	86.25	7.82	25.0	32.5	550.0	0.3	485	34.7	3.45	9.8	752	4.51
11H-4, 130-150	98.70	7.86	24.8	32.5	551.0	0.0	487	34.2	3.31	9.8	711	
12H-4, 130-145	107.27	7.85	23.8	32.5	550.5	0.1	486	33.9	3.24	9.5	847	
13H-1, 130-150	113.20	7.86	23.9	32.5	550.0	0.0	485	34.3	3.29	9.6	735	4.10
14H-4, 135-150	127.25	7.83	23.6	32.5	549.0	0.0	485	33.6	3.45	9.5	804	
15H-3, 135-150	135.25	7.62	23.5	32.5	548.0	0.0	484	33.4	3.69	9.0	741	
16H-5, 135-150	147.75	7.87	21.5	32.5	548.0	0.0	484	32.6	3.85	8.9	774	3.77
17H-4, 135-150	155.75	7.87	21.4	32.0	547.0	0.0	482	33.4	3.93	8.6	798	
19H-3, 130-150	166.70	7.64	20.3	32.0	548.0	0.1	484	31.8	4.26	8.5	856	
21X-5, 130-150	187.50			32.0	545.5	0.0	479	31.6	5.51	8.7	811	3.64
22X-3, 130-150	194.20	7.57	19.4	32.0	545.5	0.0	480	31.8	4.91	8.4	886	
23X-2, 125-150	202.25			32.0	544.5	0.0	477	31.5	5.24	8.5	869	
24X-4, 125-150	214.85	7.52	16.5	32.0	544.0	0.1	476	31.1	5.39	8.4	914	2.91
25X-2, 125-150	221.45			32.0	543.0	0.0	474	30.6	5.48	8.6	837	
26X-2, 125-150	231.05			31.5	540.0	0.1	473	28.8	5.77	8.7	642	
27X-1, 125-150	239.15	7.84	11.2	31.5	540.5	0.4	474	27.9	6.27	8.3	653	2.19
36X-2, 69-84	325.62			32.5	560.0	2.7	484	36.6	7.20	7.1		
37X-1, 41-61	334.51		15.0	32.0	560.5	2.5	484	37.0	7.14	6.9		
39X-1, 25-45	353.65			33.5	557.5	6.9		40.3	7.68	7.8		
40X-1, 50-75	363.50		15.0	33.0	557.5	6.8	480	40.6	8.00	7.3		
43X-1, 130-150	393.00			34.5	558.0	17.3		45.7	9.17	7.0		
48X-CC, 0-5	440.00			35.5								

Note: ISE = ion selective electrode, Alk = alkalinity, T = titration, Sal = salinity, R = refractometry, I = ion, CB = charge balance, S = spectrophotometry.

Table T13. Headspace gas analysis, Hole 1176A.

Core, section, interval (cm)	Depth (mbsf)	Sample method	C_1/C_2	C_1 (ppm)	C_2 (ppm)	C_2= (ppm)	C_3 (ppm)	C_3= (ppm)
190-1176A-								
1H-4, 0-5	4.50	HS		7	0.0	0.0	0.0	0.0
2H-4, 0-5	11.90	HS		12	0.0	0.0	0.0	0.0
3H-4, 0-5	21.40	HS		3,378	0.0	0.0	0.0	0.0
4H-5, 0-5	32.40	HS		28,570	0.0	0.0	0.0	0.0
5H-5, 0-5	41.90	HS		23,060	0.0	0.0	0.0	0.0
6H-2, 0-5	46.90	HS		36,920	0.0	0.0	0.0	0.0
7H-5, 0-5	60.90	HS		5,728	0.0	0.0	0.0	0.0
8H-1, 0-5	64.40	HS		2,500	0.0	0.0	0.0	0.0
9H-4, 0-5	78.40	HS		19,069	0.0	0.0	0.0	0.0
10H-5, 0-5	89.40	HS		21,823	0.0	0.0	0.0	0.0
11H-3, 0-5	95.90	HS	82,532	33,013	0.4	0.0	0.0	0.0
12H-5, 0-5	107.42	HS		2,640	0.0	0.0	0.0	0.0
13H-2, 0-5	113.40	HS		10,935	0.0	0.0	0.0	0.0
14H-5, 0-5	127.40	HS		8,766	0.0	0.0	0.0	0.0
15H-4, 0-5	135.40	HS		12,312	0.0	0.0	0.0	0.0
16H-4, 0-5	144.90	HS		6,497	0.0	0.0	0.0	0.0
17H-5, 0-5	155.90	HS		8,455	0.0	0.0	0.0	0.0
18H-2, 0-5	160.77	HS		8,031	0.0	0.0	0.0	0.0
19H-4, 0-5	166.90	HS		4,483	0.0	0.0	0.0	0.0
20X-2, 0-5	172.10	HS		12,820	0.0	0.0	0.0	0.0
21X-2, 0-5	181.70	HS	25,402	7,621	0.3	0.0	0.0	0.0
22X-5, 0-5	195.90	HS	31,692	28,523	0.9	0.0	0.0	0.0
23X-3, 0-5	202.50	HS	27,054	13,527	0.5	0.0	0.0	0.0
24X-5, 0-5	215.10	HS	19,890	21,880	1.1	0.3	0.0	0.0
25X-3, 0-5	221.70	HS	13,009	19,514	1.5	0.4	0.0	0.0
26X-3, 0-5	231.30	HS	7,772	7,772	1.0	0.3	0.0	0.0
27X-2, 0-5	239.40	HS	8,460	10,998	1.3	0.0	0.0	0.0
28X-1, 0-5	247.50	HS		2,549	0.0	0.0	0.0	0.0
31X-CC, 0-5	276.40	HS	10,650	8,520	0.8	0.0	0.0	0.0
33X-1, 0-5	295.70	HS		517	0.0	0.0	0.0	0.0
36X-1, 28-43	324.78	HS		8	0.0	0.0	0.0	0.0
37X-1, 41-61	334.51	HS	19	6	0.3	0.0	0.0	0.0
39X-2, 0-5	353.85	HS	32	32	1.0	0.0	0.0	0.0
40X-2, 0-5	363.75	HS	10	7	0.7	0.3	0.5	0.0
41X-CC, 0-5	372.70	HS		6	0.0	0.0	0.0	0.0
43X-2, 0-5	393.50	HS		6	0.0	0.0	0.0	0.0
44X-1, 0-5	401.60	HS		8	0.0	0.0	0.0	0.0

Note: HS = headspace.

Table T14. Carbon, nitrogen, sulfur, and hydrogen analyses, Hole 1176A.

Core, section, interval (cm)	Depth (mbsf)	Inorganic C (wt%)	$CaCO_3$ (wt%)	TOC (wt%)	Organic C (wt%)	N (wt%)	S (wt%)	H (mg HC/g of sediment)
190-1176A-								
1H-2, 135-136	2.85	1.17	9.78	NA	NA	NA	NA	NA
1H-3, 137-138	4.37	1.08	9.03	NA	NA	NA	NA	NA
1H-4, 137-138	5.87	1.01	8.42	1.40	0.32	0.16	0.51	0.67
2H-2, 136-137	10.26	1.04	8.66	NA	NA	NA	NA	NA
2H-4, 137-138	13.27	1.18	9.85	NA	NA	NA	NA	NA
2H-6, 87-88	15.77	1.43	11.96	NA	NA	NA	NA	NA
3H-2, 137-138	19.77	2.09	17.48	NA	NA	NA	NA	NA
3H-4, 138-139	22.78	1.40	11.68	NA	NA	NA	NA	NA
3H-6, 89-90	25.29	0.95	7.92	NA	NA	NA	NA	NA
4H-2, 141-142	29.31	0.96	8.06	NA	NA	NA	NA	NA
4H-3, 67-68	30.07	0.69	5.78	1.34	0.65	0.14	0.00	0.58
4H-5, 140-141	33.80	1.59	13.25	NA	NA	NA	NA	NA
5H-5, 70-71	42.60	1.61	13.42	NA	NA	NA	NA	NA
6H-4, 109-110	50.99	1.08	9.03	NA	NA	NA	NA	NA
7H-4, 129-130	60.69	1.75	14.65	NA	NA	NA	NA	NA
7H-6, 8-9	62.48	0.25	2.09	0.30	0.05	0.02	0.00	0.43
8H-1, 68-69	65.08	2.04	17.03	NA	NA	NA	NA	NA
9H-3, 131-132	78.21	2.29	19.14	NA	NA	NA	NA	NA
9H-6, 70-71	82.10	3.18	26.51	NA	NA	NA	NA	NA
10H-2, 77-78	85.67	2.62	21.89	NA	NA	NA	NA	NA
10H-3, 132-133	87.72	2.02	16.90	NA	NA	NA	NA	NA
11H-4, 106-107	98.46	1.88	15.72	NA	NA	NA	NA	NA
12H-4, 126-127	107.23	1.22	10.24	NA	NA	NA	NA	NA
13H-1, 127-128	113.17	1.27	10.64	NA	NA	NA	NA	NA
14H-2, 79-80	123.69	2.22	18.51	NA	NA	NA	NA	NA
14H-4, 130-131	127.20	1.89	15.80	NA	NA	NA	NA	NA
15H-3, 130-131	135.20	1.21	10.14	1.73	0.52	0.01	0.40	0.53
16H-5, 130-131	147.70	2.19	18.32	NA	NA	NA	NA	NA
17H-4, 132-133	155.72	2.12	17.66	NA	NA	NA	NA	NA
18H-1, 136-137	160.76	1.54	12.88	NA	NA	NA	NA	NA
18H-2, 69-70	161.46	0.11	0.96	NA	NA	NA	NA	NA
19H-3, 129-130	166.69	2.02	16.82	NA	NA	NA	NA	NA
19H-5, 77-78	169.17	1.41	11.78	NA	NA	NA	NA	NA
20X-1, 43-44	171.03	1.62	13.53	NA	NA	NA	NA	NA
21X-5, 120-121	187.40	1.44	12.07	NA	NA	NA	NA	NA
22X-3, 105-106	193.95	1.85	15.47	NA	NA	NA	NA	NA
23X-3, 60-61	203.10	0.86	7.17	1.26	0.39	0.12	0.16	0.48
24X-3, 88-89	212.98	1.34	11.18	NA	NA	NA	NA	NA
24X-6, 60-61	217.20	2.85	23.77	NA	NA	NA	NA	NA
25X-2, 122-123	221.42	1.23	10.28	NA	NA	NA	NA	NA
25X-4, 69-70	223.89	0.63	5.32	NA	NA	NA	NA	NA
25X-CC, 30-31	224.72	0.05	0.48	0.11	0.05	0.03	0.00	0.46
26X-2, 120-121	231.00	0.68	5.71	NA	NA	NA	NA	NA
27X-1, 120-121	239.10	0.26	2.23	NA	NA	NA	NA	NA
29X-CC, 27-28	257.37	0.19	1.61	0.50	0.31	0.03	0.25	0.34
33X-CC, 16-17	296.65	0.08	0.69	NA	NA	NA	NA	NA
34X-CC, 23-24	305.53	0.10	0.90	NA	NA	NA	NA	NA
36X-1, 28-29	324.78	0.10	0.89	NA	NA	NA	NA	NA
36X-2, 68-69	325.61	0.07	0.59	NA	NA	NA	NA	NA
37X-1, 40-41	334.50	0.12	1.04	2.38	2.25	0.03	2.07	0.51
39X-1, 24-25	353.64	0.06	0.51	NA	NA	NA	NA	NA
40X-1, 48-49	363.48	0.22	1.91	1.09	0.86	0.02	1.05	0.33
41X-CC, 12-13	372.82	0.41	3.48	NA	NA	NA	NA	NA
43X-1, 121-122	393.21	0.08	0.67	NA	NA	NA	NA	NA
43X-2, 57-58	394.07	4.41	36.78	NA	NA	NA	NA	NA
43X-2, 129-130	394.79	0.10	0.87	0.42	0.32	0.04	0.39	0.46
44X-CC, 1-2	402.40	0.34	2.90	NA	NA	NA	NA	NA

Notes: TOC = total organic carbon; HC = hydrocarbon. NA = not analyzed.

Table T15. Total bacterial populations in sediments, Site 1176.

Depth (mbsf)	Bacterial cells (cells/cm^3)
0.00	6.67×10^8
1.19	9.33×10^7
5.89	3.83×10^7
11.79	1.76×10^7
19.79	2.81×10^7
29.29	1.75×10^7
37.24	1.24×10^7
51.04	3.66×10^6
60.69	5.74×10^6
78.24	1.04×10^7
98.49	1.50×10^7
127.29	6.46×10^6
166.69	1.31×10^7
193.94	1.19×10^7
231.04	6.15×10^6
343.86	1.71×10^6
363.49	1.71×10^6

Table T16. Comparison of near-surface sediment bacterial populations at Site 1176 with data from nine other ODP sites with different overlying-water depths.

Location	ODP leg-site	Depth (mbsf)	Total bacteria (cells/cm^3)
Peru margin	112-681	150	1.05×10^9
Santa Barbara Basin	146-893	577	1.27×10^9
Japan Sea	128-798	900	7.82×10^8
Woodlark Basin	180-1115	1150	2.83×10^8
Cascadia margin	146-890	1326	6.95×10^8
Woodlark Basin	180-1109	2211	3.28×10^8
Juan de Fuca Ridge	139-857	2419	8.28×10^8
Cascadia margin	146-888	2516	5.32×10^8
Lau Basin	135-834	2703	6.12×10^8
Woodlark Basin	180-1108	3188	2.67×10^8
Amazon Fan	155-940	3195	5.62×10^8
Amazon Fan	155-934	3432	6.04×10^8
Eastern Equatorial Pacific	138-851	3760	2.08×10^8
Nankai Trough	190-1173	4791	7.23×10^7
	190-1174	4751	1.47×10^8
	190-1175	2998	6.97×10^7
	190-1176	3020	6.67×10^8

Table T17. Formation factor data from the needle-probe method, Hole 1176A.

Core, section, interval (cm)	Depth (mbsf)	Lithologic type	Formation factor	
			y	z
190-1176A-				
1H-2, 113	2.63	Clayey silt	2.37	2.28
1H-5, 5	6.05	Clayey silt	2.57	2.43
2H-2, 110	10.00	Clayey silt	2.70	2.66
2H-5, 106	14.46	Clayey silt	2.74	2.78
3H-2, 105	19.45	Clayey silt	2.52	2.51
3H-5, 90	23.80	Clayey silt	2.60	2.44
4H-2, 126	29.16	Clayey silt	2.91	2.87
4H-5, 105	33.45	Clayey silt	2.85	2.94
5H-2, 62	38.02	Clayey silt	3.58	3.14
6H-2, 55	47.45	Clayey silt	2.52	3.18
6H-5, 95	52.35	Clayey silt	2.43	2.75
7H-2, 80	57.20	Clayey silt	3.01	3.05
7H-6, 81	63.21	Clayey silt	4.20	4.97
8H-1, 65	65.05	Clayey silt	3.81	3.91
9H-2, 82	76.22	Clayey silt	3.70	3.91
9H-6, 67	82.07	Clayey silt	3.59	4.23
10H-2, 70	85.60	Clayey silt	3.36	3.36
11H-2, 85	95.25	Clayey silt	4.01	4.37
11H-5, 83	99.73	Clayey silt	3.80	4.59
12H-3, 80	105.27	Clayey silt	3.31	3.43
12H-5, 44	107.86	Clayey silt	4.25	3.97
12H-4, 24	106.21	Clayey silt	3.69	3.76
13H-2, 80	114.20	Clayey silt	3.83	3.17
14H-2, 71	123.61	Clayey silt	3.80	3.46
14H-5, 88	128.28	Clayey silt	4.10	3.67
15H-2, 90	133.30	Clayey silt	3.44	3.41
15H-5, 88	137.78	Clayey silt	4.51	3.50
16H-2, 84	142.74	Clayey silt	3.79	3.94
16H-5, 83	147.23	Clayey silt	4.17	3.75
17H-2, 70	152.10	Clayey silt	3.32	3.26
17H-5, 80	156.70	Clayey silt	3.63	3.18
18H-1, 94	160.34	Clayey silt	4.39	4.07
19H-2, 68	164.58	Clayey silt	3.86	3.56
19H-5, 88	169.28	Clayey silt	4.17	4.29

Note: x and y = probe axis.

Table T18. Electrical conductivities and formation factor data for cubes, Hole 1176A.

Core, section, interval (cm)	Depth (mbsf)	Conductivity (S/m)			Temp (°C)	Formation factor		
		x	y	z		x	y	z
190-1176A-								
21X-5, 135	187.55	1.25	1.32	1.13	25.0	4.24	4.00	4.68
22X-3, 74	193.64	1.35	1.30	1.27	25.1	3.94	4.09	4.17
22X-5, 125	197.15	1.41	1.36	1.24	24.8	3.75	3.89	4.27
24X-3, 86	212.96	1.21	1.27	1.07	25.3	4.40	4.19	4.96
24X-5, 35	215.45	1.31	1.30	1.16	25.3	4.08	4.12	4.59
25X-1, 107	219.77	1.32	1.31	1.10	24.9	4.00	4.05	4.82
25X-2, 97	221.17	1.13	1.14	1.08	24.9	4.69	4.64	4.91
26X-1, 70	229.00	1.15	1.16	1.04	25.2	4.62	4.60	5.10
26X-4, 99	233.79	0.96	0.98	0.94	25.2	5.55	5.45	5.68
43X-2, 127	394.77	1.00	0.89	0.85	25.6	5.37	6.04	6.33
43X-3, 83	395.83	1.13	1.02	0.87	25.7	4.76	5.25	6.16
44X-CC, 2	402.41	1.12	1.00	0.84	25.7	4.79	5.36	6.41

Note: x, y, and z = probe axis.

Table T19. Summary of downhole temperature measurements, Hole 1176A.

Depth (mbsf)	Tool	Measurement location	In situ temperature (°C)
0	Adara	Mudline	1.30
35.9	Adara	Bottom of Core 4H	4.07
73.9	Adara	Bottom of Core 8H	4.94
111.9	Adara	Bottom of Core 14H	7.31
160.5	DVTP	After Core 18H	10.10
248.5	DVTP	After Core 28X	15.05
295.7	DVTP	After Core 34X	10.34*
314.9	WSTP	After Core 36X	13.04*
383.5	DVTP	After Core 42X	11.63*

Notes: * = temperature suspected to be lowered by seawater infiltration. DVTP = Davis-Villinger temperature probe, WSTP = water-sampling temperature probe.